UNIVERSIDAD DE CHILE
FACULTAD DE CIENCIAS FÍSICAS Y MATEMÁTICAS
DEPARTAMENTO DE GEOLOGÍA

CONTROLS ON GE/SI RATIOS IN SILICEOUS SINTERS IN GEOTHERMAL FIELDS

TESIS PARA OPTAR AL GRADO DE MAGÍSTER EN
CIENCIAS MENCIÓN GEOLOGÍA

MEMORIA PARA OPTAR AL TÍTULO DE GEÓLOGA

VALERIA ANDREA BUSTAMANTE PÉREZ

PROFESORA GUÍA:
ALIDA PÉREZ FODICH

MIEMBROS DE LA COMISIÓN:
MARTIN REICH MORALES
CAROLINA MUÑOZ SAEZ

Este trabajo ha sido financiado por los proyectos FONDECYT 11200656 y U-Inicia UI- 006/20, el Centro de Excelencia en Geotermia de Los Andes (FONDAP-ACE210005), Corporación Nacional de Desarrollo Indígena, y por la Subdirección de Pueblos Indígenas de la Facultad de Ciencias Físicas y Matemáticas de la Universidad de Chile.

SANTIAGO DE CHILE
2024

RESUMEN DE LA TESIS PARA OPTAR AL GRADO DE MAGÍSTER EN CIENCIAS, MENCIÓN GEOLOGÍA Y MEMORIA PARA OPTAR AL TÍTULO DE GEÓLOGA

POR: VALERIA ANDREA BUSTAMANTE PÉREZ

FECHA: 2024

PROFESOR GUÍA: ALIDA PÉREZ FODICH

MECANISMOS DE CONTROL DE LAS RAZONES GE/SI EN SÍNTERES SILÍCEOS EN SISTEMAS GEOTERMALES

Los sínteres silíceos son depósitos formados cerca de la superficie, al precipitar un fluido hidrotermal rico en sílice. El campo geotermal El Tatio, ubicado a 4300 m.s.n.m. en Sudamérica, y contiene más de 200 manifestaciones termales. Las tasas de precipitación de sílice en El Tatio parecen estar controladas por las condiciones ambientales, que impulsan el enfriamiento rápido del agua, la alta evaporación y los microorganismos presentes. La dinámica de la precipitación puede influir en la incorporación de elementos traza como el Ge y el Al, que pueden sustituir a los átomos de Si en la estructura del ópalo. El objetivo de esta investigación es determinar la variación de la razón Ge/Si en fluidos y precipitados fósiles y modernos del campo geotermal El Tatio, además de comprender el efecto de las condiciones medioambientales en el fraccionamiento de la razón Ge/Si durante la precipitación de ópalo.

Se seleccionaron dos manifestaciones termales, Ckoitchi (chorro perpetuo) Vega Rinconada (géiser), para la obtención de muestras de fluidos hidrotermales y depósitos de sínteres activos, así como para el desarrollo de experimentos de precipitación y evaporación in-situ. Además, se consideró la toma de muestras de un sínter fósil para su posterior comparación, junto con muestras de estudios previos en El Tatio y en otros dos campos geotermales de Chile. A partir del experimento de evaporación, se estableció que, a mayor volumen evaporado, precipita más sílice, aumentando las razones Ge/Si en el fluido desde 71.9 a 81.4 μmol/mol, debido al comportamiento conservativo del Ge con respecto al Si. Los fluidos hidrotermales en El Tatio presentan razones Ge/Si entre 68.52 y 110.98 μmol/mol, mientras que los depósitos de sínter tienen razones Ge/Si que varían de 1.3 a 32.58 μmol/mol. Respecto al experimento de precipitación, se obtuvieron tasas de precipitación mayores de las ya registradas para El Tatio, entre 0.44 y 5.8 kg/año/m^2. Las tasas de precipitación aumentan a medida que el fluido se enfría al escurrir desde su fuente, desde 0.6 a 2.7 kg/año/m^2 en promedio entre la fuente y el punto más distal muestreado (4.2 metros), tanto en el chorro perpetuo como en el géiser. Además, el experimento demuestra que la razón Ge/Si de los precipitados disminuye alejarse desde la fuente. Las razones Ge/Si obtenidas en los depósitos de sínteres muestran una relación inversamente proporcional con las tasas de precipitación, lo cual es indicativo de que, a mayores tasas de precipitación, la incorporación de Ge en los depósitos disminuye, debido a la lenta cinética de incorporación del Ge respecto a la precipitación de Si.

Los resultados evidencian la lenta incorporación de elementos traza en sínteres silíceos a medida que aumenta la tasa de precipitación de sílice, subrayando la influencia de la cinética de los procesos hidrotermales en la precipitación de elementos y su partición en fases sólidas, enfatizando el uso de la razón Ge/Si como trazador de la dinámica del sílice en ambientes hidrotermales.

SUMMARY OF THE THESIS FOR THE DEGREE OF MASTER OF SCIENCE IN GEOLOGY AND FOR THE DEGREE OF GEOLOGY

BY: VALERIA ANDREA BUSTAMANTE PÉREZ
DATE: 2024
ADVISOR: ALIDA PÉREZ FODICH

CONTROLS ON GE/SI RATIOS IN SILICEOUS SINTERS IN GEOTHERMAL FIELDS

Silica sinters are opal deposits formed by the precipitation of silica-rich hydrothermal fluids near the Surface. The El Tatio geothermal field is located at 4300 m.a.s.l. in South America, hosts more than 200 hydrothermal manifestations. The precipitation dynamics can impact the incorporation of trace elements such as Ge and Al which can substitute Si atoms in the opal structure. This thesis aims to understand determine the variation of the Ge/Si ratio in fossil and modern fluids and precipitates from the El Tatio geothermal field, in addition to understanding the effect of environmental conditions on the fractionation of the Ge/Si ratio during opal precipitation.

Two thermal manifestations, Ckoitchi (perpetual spouter) and Vega Rinconada (geyser), were selected for sampling hydrothermal fluids and active sinter deposits, as well as for conducting in-situ precipitation and evaporation experiments. Additionally, sampling included a fossil sinter for comparative analysis, alongside samples from previous studies conducted in El Tatio and two other geothermal fields in Chile. The evaporation experiment shows that higher volumes of evaporation lead to increased silica precipitation, thereby increasing the Ge/Si ratios in the fluid from 71.9 to 81.4 μmol/mol, due to the conservative behavior of Ge relative to Si. Hydrothermal fluids in El Tatio exhibit Ge/Si ratios ranging from 68.52 to 110.98 μmol/mol, whereas sinter deposits have Ge/Si ratios varying from 1.3 to 32.58 μmol/mol. The results from the silica precipitation experiments show higher precipitation rates when compared to those previously documented for El Tatio, ranging between 0.44 and 5.8 kg/year/m^2. The precipitation rates increase as the fluid cools while flowing from its vent, ranging from 0.6 to 2.7 kg/year/m^2 on average between the vent and the furthest sampled point (4.2 meters), both in the perpetual spouter and the geyser. In addition, the silica precipitation experiments show that Ge/Si ratios in the precipitates decreases downstream from the vent. Overall, the results from both precipitation experiments and in-situ sinter deposits show that Ge/Si ratios show an inversely proportional relationship with precipitation rates, indicative that higher precipitation rates lead to reduced Ge incorporation into silica, due to the slow kinetics of Ge partitioning into the solid.

The results highlight the slow incorporation of trace elements into silica sinters as silica precipitation rates increase, emphasizing the influence of hydrothermal process kinetics on element precipitation and partitioning into solid phases. Additionally, it underscores the utility of the Ge/Si ratio as a tracer of silica dynamics in hydrothermal environments.

A Sandra y Juan,
Rebeca,
y Estilita.
A todas las mujeres antes de mí.

Watari ni fune

Agradecimientos

Quiero comenzar agradeciendo a los proyectos FONDECYT 11200656 y U-Inicia UI-006/20 que financiaron la gran parte de esta investigación. También al Centro de Excelencia en Geotermia de Los Andes (FONDAP-ACE210005) y la Corporación Nacional de Desarrollo Indígena (CONADI) quienes financiaron mi programa de Magíster en Ciencias, mención Geología. Quiero agradecer a la Subdirección de Pueblos Indígenas de la Facultad de Ciencias Físicas y Matemáticas de la Universidad de Chile, quienes financiaron parte de mis terrenos y pasantía, y me escucharon y apoyaron en cada momento. Gracias a las comunidades de Caspana y Toconce por permitirme realizar mi tesis en El Tatio. Agradezco enormemente al equipo del Laboratorio de Geoquímica de Fluidos, Verónica Rodríguez, Samuel Lepe y Erika Rojas, por recibirme, resolver mis dudas, y permitirme utilizar sus instalaciones, además de todas las conversaciones que compartimos durante todo el tiempo que nos encontramos. También agradezco al Dr. Louis Derry y la Dra. Nicole Fernandez por la oportunidad de visitar, utilizar sus laboratorios, y aprender directamente de ustedes durante mi pasantía en Cornell University, una de las mejores experiencias de mi vida. A Nadia y Diego, que me recibieron amablemente en Ithaca para vivir en su hogar durante ese tiempo. No puedo dejar de mencionar a Rosita, William, Mariela, Vero, Maritza y Blanca, quienes siempre están ayudando en lo que necesitemos, el Departamento de Geología no sería lo mismo sin ustedes. A don Pedro, que cuando coincidía su turno en la entrada principal de Geo, siempre con una sonrisa podía alegrarme el día.

A mi profesora guía Alida Pérez-Fodich, por toda su ayuda durante este periodo, desde los terrenos, laboratorios, reuniones, etc.; gracias por confiar en mi para esta investigación y por permitirme aprender a través de nuevas experiencias, como lo fue la pasantía y los congresos, sobre todo destaco el poder hacer ciencia desde todas sus aristas: desde adquirir las muestras en terreno, tratarlas en el laboratorio, analizarlas mediante algún instrumento e interpretarlas; realmente desafiante y entretenido a la vez, aunque también frustrante, pero es parte del proceso, prueba y error en su forma natural jaja. ¡Gracias por ser un ejemplo a seguir en la ciencia!. A Carolina Muñoz Sáez, por compartir su amor por El Tatio conmigo, gracias por tu ayuda en terreno y por las reuniones que tuvimos, eres también una gran referente para mí, tus sugerencias han sido invaluables. También agradezco a Martin Reich, quien aceptó ser parte de mi comisión; durante la pandemia me hizo reencantarme con la fisicoquímica, y también la geoquímica de los fluidos y minerales, gracias por sus enseñanzas y aportes durante esta investigación. Gracias a Rodrigo, Seth y Lauren, que nos acompañaron a terreno y me ayudaron a conocer El Tatio desde otra mirada, especialmente a Joaquín Castillo, gracias por tu compañía y conformar nuestro pequeño team Altiplano-Puna, por tu apoyo en la salita y los buenos momentos.

Gracias a todas las personas que hicieron de mi paso por la universidad algo inolvidable, ya sea desde el principio o ya a las finales, una mega mención especial a Cata Barraza, desde el mechoneo te convertiste en una de mis personas favoritas, gracias por estar en todas las penas y alegrías, sufrir juntas en plan común lo hizo más amigable y llevadero. A mi grupo de Geo, Alejo, Alonso, Cami, Deni, Joaco G., Lucho, Nico, Sofi, Tomi y Vanne, que cambiaron todo lo que pensé sería disfrutar la carrera, gracias por tan linda amistad y seguir presentes. Agradezco a quienes les

hice clases, y me recordaron lo lindo que es enseñar. A cada persona que conocí en postgrado, la mejor salita y compañía estos últimos años, a la Amanda por los llantos compartidos y el apañe mutuo en momentos de ansiedad. A los grupos que fuimos armando, "Panitas", "Ratonitas", "Lushos" jaja el nombre que tomase en el momento. Con cariño a la Javi, Diego, Gabs, Lucho, Alejo, Tomi, Deni, Kristian, Debo, y a quienes fueron llegando, gracias por tantas risas y bellos momentos. Destaco especialmente a Deni, Alejo y Lucho, full acompañando en lo que fuese, que bacán coincidir en los gustos musicales y todos los panoramas que podían ocurrir en el camino, gracias por cada abrazo y palabras cuando lo necesitaba. A la Bele, que desde las Europas siguió siendo un apoyo fundamental, gracias por todas las alegrías y confidencias, conversar contigo me genera mucha paz, muchas gracias por todos tus consejos. A la Cami, mi roomie favorita, la mejor persona que podía escoger para mi primera experiencia en busca de la independencia jaja, gracias por apañarme en todo lo que se me ocurriese, los gustos por las papitas, las series, y las caminatas en Francia, el modo fanática en conciertos quedándonos hasta el final de los tiempos para lograr un autógrafo ajaja, las risas, los chismes, las penas, sinceridad ante todo. A la Lore, quien se convirtió rápidamente en una de las personas más importantes para mí, me ayudaste a volver a amar la danza sin saberlo, gracias por compartir conmigo tus momentos importantes, por escucharme y soportar mis momentos de crisis pese a la distancia que pudiese haber, incluso por apoyarme en mis modos de fanática, trayéndome los CD's y libros; los detalles y los abrazos reconfortantes, hasta los ensayos antes de la primera presentación, gracias por tu paciencia infinita. A las chicas de danza, que los últimos meses las he perdido de vista, pero que siempre estuvieron y están para mi desde que las conocí: Carli, Carli rulitos, Ferni, Heather, Lore (again), Maca, Maca M., Vane, Vivi y Andre. A mis chiques del colegio, que siempre me han tenido más fe que yo misma, gracias por una amistad de tantos años y que no nota el paso del tiempo: Raúl, Cludia, Erik, Fran, Gómez, Jasmi, José, Lukin, Lusho, Nico y Nicole, espero que sigamos así, con peleas infantiles incluidas, y momentos full adultos de por medio, capaces de apañar en los momentos más duros de la vida y sin cuestionar, siempre les estaré infinitamente agradecida. A la Jasmi con mención también, aguantando mis llantos y escuchándome sin importar la hora o la distancia kilométrica, siempre incondicional; y a la Clau, capaz de siempre sonreír, y acompañando también en la locura que fuese, gracias por compartir conmigo uno de los momentos más mágicos.

Por último, a quienes les debo todo y no me alcanzará la vida para agradecer, a mi mamá y papá, Sandra y Juan, gracias por darlo todo por nosotros, por permitirme explorar el mundo en aquellas formas que ustedes no tuvieron oportunidad, así como enseñarme a apreciar los momentos simples e importantes de la vida, por cada sacrificio, cada lágrima y cada alegría, estoy realmente orgullosa de ustedes y no podría imaginarme llegar hasta aquí sin su apoyo, gracias por todos los abrazos que necesité estos últimos meses, y por todos los detalles y muestras de amor siempre. Gracias a mis abuelas Rebeca y Estilita por su amor incondicional, porque sin ustedes tampoco sería lo mismo, sus abrazos solucionan la vida. Gracias Jocelyn, por ser lo más parecido a una hermana mayor y tu apoyo durante todos los años viviendo juntas. A mi hermano, mis primas, mis tías/os, a quienes siempre preguntaron por mí y me desearon lo mejor. A mi Terry, el mejor compañero perruno que podría pedir, una mirada tuya y olvidaba todo lo malo.

Sobran y faltan las palabras a la vez, sólo queda agradecer siempre.

TABLE OF CONTENT

CHAPTER 1: INTRODUCTION 1
1.1. Silica sinter deposits 1
1.2. Factors controlling sinter formation and silica precipitation mechanisms in surface hydrothermal systems 1
1.3. Germanium as a tracer for silica precipitation mechanisms 2
1.4. El Tatio geyser field for investigating silica precipitation dynamics 4
1.5. Hypothesis and objectives 5
CHAPTER 2: METHODOLOGY 6
2.1. Hydrothermal springs sampling 6
2.2. Evaporation experiments 6
2.3. Silica precipitation experiments 7
2.4. Fossil and in-situ sinter deposit sampling 10
2.5. Opal alkaline digestions 12
2.6. Geochemical analytical methods 12
2.7. Reflected light petrography and scanning electron microscopy analyses 13
CHAPTER 3: RESULTS 15
3.1. Mineralogy of siliceous sinters 15
3.2. Geochemical composition and Ge/Si ratios of hydrothermal fluids across El Tatio 21
3.3. Fluid evaporation experiments 26
3.4. Opal precipitation experiments 32
3.4.1. Bulk precipitation rates 32
3.4.2. Ge partitioning in opal precipitates 37
3.5. Geochemistry and Ge partitioning of active and fossil sinter deposits from El Tatio 39
3.5.1. Active sinter deposits at El Tatio 39
3.5.2. Fossil sinter deposits at El Tatio and correlation with ages and precipitation rates derived from radiocarbon dating. 45
3.6. Geochemistry of active sinter deposits from other locations 48
CHAPTER 4: DISCUSSION 49
4.1. Ge/Si ratios in hydrothermal fluids across hot springs types in El Tatio 49

4.2. Efficiency of opal alkaline extractions in close to equilibrium solutions 51

4.3. Silica precipitation rates in El Tatio and their comparison to other kinetic models and field sites 52

4.4. Partitioning of Ge during silica precipitation from hydrothermal fluids 55

4.4.1. The effect of water evaporation in fast silica precipitation and the partitioning of Ge in supersaturated silica-rich hydrothermal fluids 55

4.4.2. The effect of fluid temperature and silica precipitation rates in the partitioning of Ge into opal 56

4.4.3. The role of organic matter and sinter maturation in the partitioning of Ge into opal 59

CHAPTER 5: CONCLUSIONS 62

BIBLIOGRAPHY 64

ANNEXES 76

ANNEX A 76

ANNEX B 78

ANNEX C 98

TABLE INDEX

Table 1: Characteristics of the sampling points of this study, considering the distance to the vent, temperature, and pH of the fluid, along with observations of the respective location. 8

Table 2: XRD parameters and phases identified for the fossil sinter (first group of samples, sinter mound 404 in Slagter et al., 2019) and for the Vega Rinconada and Ckoitchi vents (last two samples). The minerals correspond to cristobalite (Crs), albite (Ab), quartz (Qz) and biotite (Bt). 16

Table 3: Names assigned to Paleosinter samples in this work and their corresponding designation by Slagter et al. (2019), along with the ages obtained there. 18

Table 4: Composition of hydrothermal fluids from El Tatio. The table includes in-situ physicochemical parameters (T°, pH, specific conductivity (SPC)) and major ions composition. Temperatures are in °C, SpC in µS/cm. concentrations are expressed in mg/L. nd: no detected, '-': unmeasured. 22

Table 5: Trace element composition for the hydrothermal fluids in El Tatio, including Ge in µg/L, Ge/Si (µmol/mol) and Al/Si (mmol/mol) ratios. Concentrations are expressed in µg/L and mg/L for high concentrations. '-': unmeasured. 23

Table 6: Evaporation experiments with their respective sampling dates, evaporated volumes, and resulting evaporation rates. Evaporated volumes are expressed in mL, while evaporation rates are in mL/day. 27

Table 8: Trace element composition for the evaporation experiment samples, including Ge in µg/L, Ge/Si (µmol/mol) and Al/Si (mmol/mol) ratios. Concentrations are expressed in µg/L and mg/L for high concentrations. 28

Table 9: Information obtained from the precipitation experiment conducted at Ckoitchi. The positions of the slides are those in which they were found at the end of the experiment. A_{Ep}= Effectively precipitated area. H=horizontal position, V= vertical position, Subh= subhorizontal position. *= slide used for geochemical analysis. 33

Table 10: Information obtained from the precipitation experiment conducted at Vega Rinconada. The positions of the slides are those in which they were found at the end of the experiment. A_{Ep}= Effectively precipitated area. H=horizontal position, V= vertical position, Subh= subhorizontal position. *= slide used for geochemical analysis. 34

Table 11: Silica precipitation rates and geochemistry of the silica precipitation experiments. The table lists sampling temperature, silica precipitation rates, SiO_2, Ge (ppt) and Ge/Si. 37

Table 12: Geochemistry of the active sinter deposits at El Tatio. The table lists alkaline extraction month in 2022, sampling temperature, sample site of the sample, SiO_2, Ge (ppt) and Ge/Si. 41

Table 13: Geochemistry of other active sinter deposits at El Tatio, considering some additional samples extracted in this work and by Slagter et al. (2019) and Munoz-Saez et al. (2020). The table lists the alkaline extraction month in 2022, data origin, sampling temperature, SiO_2, Ge (ppm), and Ge/Si. 45

Table 14: Geochemistry of the Paleosinter deposit of this study). The table lists the alkaline extraction month in 2022, data origin, SiO_2, Ge (ppb), and Ge/Si. The asterisk (*) represents a laboratory duplicate sample of ET06-PSc1. 46

Table 15: Geochemistry of other fossil sinter deposits at El Tatio, considering additional samples from Slagter et al. (2019) and Munoz-Saez et al. (2020). The table lists the alkaline extraction month in 2022, data origin, SiO_2, Ge (ppt), and Ge/Si. 47

The silica concentrations in the examined sinters (..... 48

Table 16: Geochemistry of other active sinter deposits at Alpehue (Perez, 2019) and Puchuldiza (Sanchez-Yanez et al., 2017). The table lists the alkaline extraction month in 2022, data origin, SiO_2, Ge (ppb), and Ge/Si. 48

Table 17: Qualitative information obtained from energy-dispersive X-ray spectrometry (EDS) in scanning electron microscopy (SEM) considering three samples of sinter in-situ (from vents of Ckoitchi and Vega Rinconada, and sinter of Piscina Linzor) and samples from the precipitation experiment (nine samples, one per position without considering the Ckoitchi vent). 98

FIGURE INDEX

Figure 1: Compilation of Ge/Si ratios vs Si concentrations in hot springs around the world. The black solid square and the colorless square correspond to samples from hot springs and wells in Iceland, respectively (Arnórsson, 1984) The hexagram represents the Yellowstone hot springs samples (Gaspard et al., 2021b). Polish springs samples are represented by asterisks (Dobrzyński et al., 2018). Samples from Massif Central springs(Criaud & Fouillac, 1986) are represented by triangles., while samples from Himalayan springs (Evans & Derry, 2002) are denoted by squares. Samples from Guadeloupe hot springs (Gaspard et al., 2021a) are represented by stars. The light blue circle represents the average of the Freshwater (Mortlock & Froelich, 1987). 3

Figure 3: Location of sampling points for the precipitation experiments. (A) Top panel shows photograph of the position of the experiments around Ckoitchi (perpetual spouter). Bottom panel includes a schematic profile of the points with their respective daily average temperatures. (B) Top panel shows photograph of the Vega Rinconada sector and the position of the experiments. At the bottom, the respective schematic profile with their respective daily average temperatures. Both profiles were modified from Guido & Campbell (2011) and are not to scale. 7

Figure 4: Images associated with the Ckoitchi zone, showing (A) a general view of some of the sampling points, with the red arrow indicating point Ck-4, (B) a close-up of the precipitation experiment at point Ck-44, almost 7 months after its implementation, the red arrow indicates the precipitate (C) denominated Co04-15 and (D) samples of in-situ sinter deposits at that point. 11

Figure 5: Images of the Vega Rinconada area, showing (A) an overview of the geyser surroundings, with the red arrow indicating sampling point VR03, (B) a close-up of the experiment at VR-3, with the red arrow indicating (C) the VR03-27 precipitate, and (D) samples of in-situ sinter deposits at that point. 11

Figure 6: XRD spectrum of active sinters of the vents from Ckoitchi (ET03-Co01, spectrum at the top) and Vega Rinconada (ET02-VR01, spectrum at the bottom). The broadband of VR is centered in 25.6°2θ. The accessory minerals identified correspond to albite (Ab), detrital quartz (Qz), and cristobalite (Crs), which contributes to the identification of the samples as Opal. 16

Figure 7: XRD spectra for the analysis of clays in the ET03-Co01 sample according to the criteria of Moore and Reynolds (1997). From the bottom, the spectra of air-dried (AD, red spectrum), ethylene-glycol solvated (EG, blue spectrum), and heated (H, green spectrum) respectively. Illite (Ilt) and smectite (Sm) were identified. 17

Figure 8: XRD spectrum of paleosinter (sinter 404 of Slagter et al., 2019). The broadband is centered around 25°2θ for all samples. The accessory minerals identified correspond to albite (Ab), biotite (Bt) and detrital quartz (Qz), in addition, cristobalite (Crs) is identified, which contributes to the identification of the samples as opal. 18

Figure 9: Cross-sections of the sinter deposits from the in-situ precipitation experiment. The images are oriented with the glass slides at the bottom and the growth of the sinter upwards. (A) SEM photomicrograph of sample Co04-15 showing sinter laminations. The lower arrow indicates the boundary between the glass slide (bottom) and the precipitate, while the upper inset corresponds to the image in B. (B) Enlarged rectangle showing silicified microbial filaments and a cavity with silica microspheres. The arrow indicates a sheathed filament. (C) SEM image of sample VR01-21 showing a massive silica layer, together with free microbial filaments on top of the glass slide. The red arrow indicates the boundary between the glass slide (bottom) and the precipitate (top). (D) SEM photomicrograph of sample VR02-49 composed mainly of massive silica and exhibiting a microspicule. 19

Figure 10: SEM images of samples ET02-VR01 (A), ET03-Co01 (C) and their respective resulting profiles (B and D) of the Al/Si ratios obtained by EDS analysis. Each line represents where the profile was performed and the small lower star indicates the starting direction of the profile, i.e., the initial distance 0. 20

Figure 11: Silica (a) and germanium (b) concentrations of hydrothermal fluids from El Tatio. The pink diamonds represent the Ckoitchi (Ck) samples, the blue circles are the Vega Rinconada (VR) samples. LC: La Concha (asterisk), EA: El Asesino (cross), PC: Piscina Cristalina (star), PE: Piscina Evap. Exp. (hexagram), EH: El Horno (plus sign), CO: El Cobreloa (downward triangle), GC: Geyser Corazon (rightward triangle).... 24

Figure 12: Ge/Si (a) and Al/Si (b) ratios as a function of temperature for El Tatio geothermal fluid samples. The pink diamonds represent the Ckoitchi (Ck) samples, the blue circles are the Vega Rinconada (VR) samples. LC: La Concha (asterisk), EA: El Asesino (cross), PC: Piscina Cristalina (star), PE: Piscina Evap. Exp. (hexagram), EH: El Horno (plus sign), CO: El Cobreloa (downward triangle), GC: Geyser Corazon (rightward triangle). 24

Figure 13: Major (a and c) and trace (b and d) element concentrations as a function of in-situ temperature for the Ckoitchi (Ck, pink diamonds) and Vega Rinconada (VR, blue circles) fluids. 25

Figure 14: Fluid Ge/Si (A) and Al/Si (B) ratios as a function of temperature in-situ for Ckoitchi (Ck, pink diamonds) and Vega Rinconada (VR, blue circles). 26

Figure 15: Silica(a), germanium (b), chloride (c) and aluminum (d) concentrations of the remaining fluid as a function of the evaporated volume in the evaporation experiment. Each blue square represents a sample, while the blue triangles represent the samples extracted on the last day (October 1st). 29

Figure 16: Silica (a), germanium (b), chloride (c) and aluminum (d) concentrations of the remaining fluid as a function of the Average Evaporation Rate (mL/day) in the evaporation experiment. Each blue square represents a sample, while the blue triangles represent the samples extracted on the last day (October 1st). 30

Figure 17: Ge/Si (A) and Al/Si (B) ratios as a function of the evaporated volume in the evaporation experiment. Each blue square represents a sample, while the triangles represent the samples extracted on the last day (October 1st). 31

Figure 18: Ge/Si (A) and Al/Si (B) ratios as a function of the Average Evaporation Rate (mL/day) in the evaporation experiment. Each blue square represents a sample, while the triangles represent the samples extracted on the last day (October 1st). 31

Figure 19: Bulk silica precipitation rate (kg/year/m^2) in the glass slides as a function of temperature (°C) for each site at Ckoitchi (Ck, pink bar) and Vega Rinconada (VR, blue bar). 35

Figure 20: Adjusted silica precipitation rate (kg/year/m^2) in the glass slides as a function of temperature (°C) for each site at Ckoitchi (Ck, pink bar) and Vega Rinconada (VR, blue bar). The weighting factors (opal SiO_2 measurements) for the bulk precipitation rate used to obtain the adjusted rate were: 56% for Ck-V and Ck-1, 94% for Ck-2, Ck-3=92%, Ck-4= 85%, Ck-5= 74%, VR-1= 96% and for VR-2, VR-3 and VR-4=100%. 36

Figure 21: Silica concentrations as a function of temperature (a) and bulk precipitation rates (b) for samples from the Ckoitchi (pink diamonds) and Vega Rinconada (blue circles) precipitation experiments. Each point is associated with their respective position in the experiment, denoted as Ck-X or VR-X. 38

Figure 22: Germanium concentrations as a function of temperature (a) and bulk precipitation rates (b) for samples from the Ckoitchi (pink diamonds) and Vega Rinconada (blue circles) precipitation experiments. Each point is associated with its respective position in the experiment, denoted as Ck-X or VR-X. 38

Figure 23: Ge/Si ratios as a function of temperature in ºC (a) and silica precipitation rate (kg/yr/m^2) (b) for the silica precipitation experiments at Ckoitchi (Ck, pink diamonds) and Vega Rinconada (VR, blue circles). 39

Figure 24: Silica (wt%) and Ge concentrations (ppm) in the Ckoitchi (Ck) and Vega Rinconada (VR) sectors as a function of temperature (°C), considering the alkaline extraction groups performed in January and December separately from the Ck Org samples. (a) Silica concentrations as a function of temperature for Ck samples. (b) Silica concentrations versus temperature for VR samples. (c) Ge concentrations as a function of temperature for Ck samples. (d) Ge concentrations versus temperature for VR samples. The diamonds correspond to the Ck samples, with the January samples indicated by purple and the December samples by pink. The asterisk (*) in Ck is used to represent a duplicate December sample from the Ck-4 point. Red triangles denote the Ck Org. group samples. Vega Rinconada samples are depicted as circles, with January samples shown in green and December samples in blue. The error bars depict the uncertainty in the Ge measurement. The asterisk in VR represents the duplicate sample VR-1. 42

Figure 25: Silica (wt%) and Ge concentrations (ppm) in the Ckoitchi (Ck) and Vega Rinconada (VR) sectors as a function of the average Bulk silica precipitation rate

(kg/year/m^2), considering the alkaline extraction groups performed in January and December separately from the Ck Org samples. (a) Silica concentrations as a function of Bulk silica precipitation rate for Ck samples. (b) Silica concentrations versus Bulk silica precipitation rate for VR samples. (c) Ge concentrations as a function of Bulk silica precipitation rate for Ck samples. (d) Ge concentrations versus Bulk silica precipitation rate for VR samples. The diamonds correspond to the Ck samples, with the January samples indicated by purple and the December samples by pink. The asterisk (*) in Ck is used to represent a duplicate December sample from the Ck-4 point. Red triangles denote the Ck Org. group samples. Vega Rinconada samples are depicted as circles, with January samples shown in green and December samples in blue. The error bars depict the uncertainty in the Ge measurement. The asterisk in VR represents the duplicate sample VR-1. 43

Figure 26: Ge/Si ratios in active (in-situ) sinter deposits as a function of temperature. (a) shows the Ckoitchi samples from January (purple diamonds), December (pink diamonds) and Organic (red triangles) as a function of temperature. (b) Vega Rinconada samples from January (green circles) and December (blue circles) as a function of temperature. The error bars depict the uncertainty in the Ge measurement. 44

Figure 27: Silica (a) and germanium (b) concentrations in the Paleosinter as a function of ages obtained by radiocarbon dating according to Slagter et al. (2019) for the analogous samples. A duplicate analysis was performed to the sample corresponding to 6330 yr B.P. (ET06-PSc1), shown with an asterisk (*) in the figure. 46

Figure 28: Ge/Si ratios in Paleosinter samples as a function of ages by radiocarbon dating and precipitation rates obtained by Slagter et al. (2019) for analogous samples. A duplicate analysis was performed to the sample corresponding to 6330 yr B.P. (ET06-PSc1), shown with an asterisk (*) in the figure. 47

Figure 29: Fluid Ge/Si ratios versus Si (µmol/kg) in hot springs from El Tatio Geothermal Field in red circles, plus a compilation of hydrothermal fluids from around the world. Legend is the same as Figure 1. Ge/Si data were compiled from Arnórsson (1984), Criaud & Fouillac (1986), Dobrzyński et al. (2018), Evans & Derry (2002), Gaspard et al. (2021a) and Gaspard et al. (2021b). 50

Figure 30: Measured silica precipitation rates and modeled rates from Carroll et al. (1998) (dashed lines) and and Rimstidt & Barnes (1980) (solid lines). The pink boxes correspond to the Ckoitchi precipitates and the blue boxes to the Vega Rinconada precipitates. The modeled curves assume the fluid silica concentration is equal to those at the vents of Ck (pink) and VR (blue). 53

Figure 31: Comparative scheme of silica precipitation rates in different studies both in El Tatio and other geothermal systems around the world. The samples in color (first group) correspond to those obtained in this work. The light pink color represents the bulk silica precipitation rate, while the dark pink color corresponds to the adjusted silica precipitation rate. The other two groups of rates in El Tatio (in gray) were established by Slagter et al. (2019) through in situ precipitation experiments on sandpaper strips

and by Nicolau et al. (2014) in glass slides. Experiments in New Zealand (Handley et al., 2005; Mountain et al., 2003), Iceland (Konhauser et al., 2001; Tobler et al., 2008) and Yellowstone, U.S. (Braunstein & Lowe, 2001) were also performed on glass slides (gray color). Figure modified from Slagter et al. (2019). 54

Figure 32: Ge/Si ratios of active (in-situ) sinter deposits as a function of bulk silica precipitation rates. Panel (a) shows Ckoitchi samples from the extractions performed in January (purple diamonds), December extractions (pink diamonds) and organic matter rich samples (red triangles) as a function of the bulk precipitation rate. (b) Vega Rinconada samples from January extractions (green circles) and December extractions (blue circles). The error bars depict the uncertainty in the Ge measurement. 56

Figure 33: Ge/Si ratios for fluids (a) and for both active precipitates (in-situ) and those from the precipitation experiment (b), plotted as a function of precipitation rates from the experiment, for the Ckoitchi (pink and purple diamonds, pink squares) and Vega Rinconada (green and blue circles, blue squares) sectors. 57

Figure 34: Apparent partition coefficients ($K_D=(Ge/Si)_{solid}/(Ge/Si)_{fluid}$) as a function of the silica precipitation rates determined in this study for the precipitated samples of the experiment at Ckoitchi (pink diamonds) and Vega Rinconada (blue circles). 58

Figure 35: Apparent partition coefficients ($K_D=(Ge/Si)_{solid}/(Ge/Si)_{fluid}$) as a function of the silica precipitation rates determined in this study for the in-situ sinter deposit samples from Ckoitchi and Vega Rinconada. The diamonds correspond to the Ck samples, with the January samples indicated by purple and the December samples by pink. Red triangles denote the Ck Org. group samples. Vega Rinconada samples are depicted as circles, with January samples shown in green and December samples in blue. 58

Figure 36: Competition between kinetic and thermodynamic factors controlling Ge partitioning in siliceous sinters. Under equilibrium behavior, precipitation rates are lower and higher partition coefficients are obtained, while under kinetic behavior, precipitation rates are faster and partition coefficients are lower. 59

Figure 37: Comparison of Ge/Si ratios between samples from the precipitation experiment, in-situ sinter samples (from this work (Table 12 and 13), Slagter et al (2019) and Munoz-Saez (2020) (Table 13), and from Sanchez-Yanez et al (2017) and Perez Nuñez (2019) (TABLE 16)) and the paleosinter samples (from this work (Table 14), and from Slagter et al (2019) and Munoz-Saez (2020) (Table 15)). 61

Figure 38: Two views of the in-situ sinter deposit sample from point VR01 at Vega Rinconada denoted ET01-VR01(A) Hand sample, geyserites of different sizes formed in the Vega Rinconada vent are observed. The spicules are finely laminated. (B) Polished cross-section of the sample in (A), shows the bedrock at the bottom, and the overlying sinter deposit, initially with laminations and subsequent formation of the geyserites. The red boxes A, B, and C are presented in the figure below. 78

Figure 39: Photographs of sample ET02-VR01 from optical microscopy. A, B and C are the respective insets in Figure 38 (above). (A) Image of a spicule, in the lower zone visualizes the bedrock, with thin laminations deposited on it. (B) Closer view of the

sinter laminations, which would indicate different depositional events, at that scale, they are small geyserites that were covered by opal precipitation. (C) Close-up of a spicule, at the edges it is possible to recognize small laminations, in addition to the presence of detritus trapped during silica precipitation. 79

Figure 40: Different views of sample ET03-Co01 of in-situ sinter deposit, belonging to point Co01 at Ckoitchi. (A) Sinter hand samples. (B) Polished cross section of the larger sample in (A), mostly corresponds to silica-cemented bedrock. (C) Close-up of the bedrock-sinter deposit boundary, at the top the sinter deposit can be distinguished, with thin whitish laminations, being covered by a yellowish-blackish layer of biological material (from the bacterial mat). (D) Close-up of the sinter deposit, showing that the whitish layers fill the bedrock material, recementing the rock. 79

Figure 41: (A) Polished cross section of sample ETLIN02 from the Piscina Linzor, its fabric follows the pattern of a network of irregular silica threads, which generate a primary porosity that could be filled later. (B) Close-up of the silica network formed in this sinter. (C) Close-up of one of the sinter pores, which is inhabited by microbial filament, similar to those described by Gong et al. (2020). 80

Figure 42: In-situ sinter deposit samples from the Ckoitchi area. (A) Samples called ET03-Co02.5, associated with the Co02 point. (B) Samples ET03-Co03 from point Co03. (C) Samples ET03-Co04 corresponding to the Co04 sector. (D) Samples ET03-Co05 from the Co05 sector. (E) Samples ET03-Co06 associated with the Co04 sector. (F) Sample ET03-Co07 located 12 m from the vent. All samples present laminations in whitish tones (deposited sinter), in addition, some of these laminations are yellowish, orange or blackish, associated with bacterial mats in the sector. 81

Figure 43: In-situ sinter deposit samples from the Vega Rinconada area along with samples from the Piscina Linzor. (A) Sample ET02-VR02 corresponding to point VR01, spicules of different widths and heights. (B) Samples ET02-VR03 from point VR02, with spicules of different sizes. (C) Samples ET02-VR04 from sector VR03, with the presence of spicules and some oncoids. (D) Sample ETLIN02 from the Piscina Linzor. The cylindrical shape is because they were extracted with a tube. The silica network and primary porosity formed during precipitation are observed. 82

Figure 44: Samples from the precipitation experiment in the vent of Ckoitchi sector. (A) Complete view of one side of the CoVent-04 sample, which was found submerged in water at the time of extraction. (B) View of the vent of Ckoitchi to get a perspective in the following images. (C) Image of 24-09-2021, the day of implementation of the experiment, the slide on the left corresponds to the one in A. (D) Image two days after installation, on 26-09-2021, where the slide acquires a yellowish color due to the splashing of the perpetual spouter vent. 83

Figure 45: Images of sample Co01-39 from the precipitation experiment, associated with point Co01, red arrows indicate the position of the sample. (A) Complete view of one of the sides of the precipitate, the upper right corner is what can be seen in D. (B) Position of the samples with respect to the Vent, image from 24-09-2021 in its installation. (C) Image after a few days, on 01-10-2021, it can be seen that the slides

present yellowish and whitish layers. (D) Image on the day of extraction, 22-04-2024, the slides do not retain their original position and are almost completely covered with blackish material, especially the submerged areas. 84

Figure 46: Sample Co01-68 from point Co01 at Ckoitchi, this slide was installed on 22-04-2022. (A) Perspective view of the slide, the left part of black-greenish shades was submerged. (B) Polished cross section of the precipitate, the red arrow indicates the non-submerged part of the sample (right part in A). (C) View of the samples at point Co01 on the day of extraction (22-04-2023), the red arrow indicates position of the sheet, indicating the same area as in B. (D) Close-up by optical microscopy of the image in B, showing the precipitate in massive form, with some colorations indicating different stages of precipitation. (E) Image by optical microscopy of the box shown in B. Fine laminations are observed in the deposit, together with some detritus trapped during precipitation. 85

Figure 56: Classification of Ckoitchi hydrothermal fluids according to Piper's classification (Piper, 1944). In this case, they correspond to Na-Cl type waters. 99

CHAPTER 1: INTRODUCTION

1.1. Silica sinter deposits

Silica sinters are opal deposits formed by the precipitation of silica-rich hydrothermal fluids during the discharge and cooling of underlying geothermal systems (Cortecci et al., 2005; Lynne & Campbell, 2003). Opal as the main component (SiO_2*nH_2O), can be found in any of its phases, either as Opal-A, Opal-CT or Opal-C (e.g., Jones & Segnit, 1971; Peng & Jones, 2012; Smith, 1998), depending on the degree of maturity of the sinter (Herdianita et al., 2000b; Lynne et al., 2005; Lynne & Campbell, 2003), with opal-A being the most immature phase. Around the world, sinter deposits can be found, for example, in Yellowstone National Park (United States, Guidry & Chafetz, 2002), Kamchatka (Russia, Kyle et al., 2007), Taupo Volcanic Zone (New Zealand, Lynne & Campbell, 2003), Iceland (Álvaro et al., 2021),or Chile (Munoz-Saez et al., 2015). Silica sinter deposits preserve information about the hydrothermal fluids through textural, chemical, and biological evidence (Cortecci et al., 2005). D. M. Guido & Campbell (2011) for example, by studying paleo-hotspring deposits from the Deseado Massif were able to determine the regional structural influence on the flow of hydrothermal fluids in the area during the Late Jurassic. Sinters are also relevant in epithermal deposit exploration, as they appear as paleosurfaces that allow the determination of thermal flow zones (either upward or lateral flows), facilitating the determination of mineralization in case they are properly identified, especially considering low and intermediate sulfidation epithermal deposits (e.g. Hamilton et al., 2019; Sillitoe, 2015). The formation of sinters has also become important in geothermal energy since silica scaling is a recurring problem in power plant equipment, and studies have focused on preventing precipitation or accelerating it to control it (e.g. Rothbaum et al., 1979; Setiawan et al., 2019; Shannon et al., 1982). Even in the initial stages of geothermal exploration, the textural information related to temperature and pH gradients obtained from sinters can be associated with a specific environment, which can help to find hidden geothermal systems (Lynne, 2012). In addition, other studies have considered sinters in astrobiological exploration given the identification of opal on the surface of Mars (e.g. Ruff & Farmer, 2016; Squyres et al., 2008; Sun & Milliken, 2015), being useful in the study of life or as a paleoenvironmental tool about the past climate on Mars, either by their morphology, preservation of biosignatures such as biosedimentary structures or determined concentrations of elements and/or minerals (Barbieri et al., 2014; Barbieri & Cavalazzi, 2014; Cady et al., 2018; Ruff et al., 2020; Sun & Milliken, 2018).

1.2. Factors controlling sinter formation and silica precipitation mechanisms in surface hydrothermal systems

The precipitation and dissolution behavior of amorphous silica in water is given by the following reaction in its simplest form and considering a pH <8.5, as:

$$SiO_{2(Am.Si.)} + 2H_2O \leftrightarrow H_4SiO_{4(aq)} \qquad (1)$$

Abiotic silica precipitation is driven by thermodynamics and kinetics, where the main factors that influence silica precipitation dynamics are: 1) fluid temperature, which controls the saturation state of silica in the fluid, and also influences kinetics as precipitation rates vary as a function

of temperature (Fournier & Rowe, 1966; Guidry & Chafetz, 2002; Rimstidt & Barnes, 1980; White et al., 1956; among others); 2) the fluid composition including concentration of silicic acid, which determines the degree of supersaturation of the fluid at a given temperature, and the concentration of metals such as Al^{3+}, Be^{2+} or Fe^{3+} which decrease silica dissolution rates (Ballou et al., 1973; Hurd, 1973; Ichikuni, 1970; Iler, 1973; Lewin, 1961); 3) evaporation rates which influence the development of the different sinter morphologies such as geyserites or lilypads (Braunstein & Lowe, 2001; Orange et al., 2013; Walter, 1976); 4) surface area and nucleation mechanisms, where surface area is a direct function of polymerization rate (Fleming, 1986; Geilert et al., 2014). Homogeneous nucleation forms nano-colloids particles, which begin a process of ripening and agglomeration either by coagulation and/or flocculation to form stable critical nuclei of silica (Saunders, 1990; Scott et al., 2024; Tobler et al., 2009; van den Heuvel et al., 2020; Weres et al., 1981). On the other hand, heterogeneous nucleation contemplates polymerization from a pre-existing surfaces (Carroll et al., 1998; Handley & Campbell, 2011; Lynne et al., 2007; Rimstidt & Cole, 1983). In addition to abiotic silica precipitation, several studies have highlighted the role of biota in the formation of massive sinter silica deposits (Handley et al., 2005; Jones et al., 1999; Lowe & Braunstein, 2003; Wilmeth et al., 2020). Intermediate to low-temperature environments (between 25-60°C) can host a wide variety of organic material, including cyanobacteria, diatoms, or pollen (Cady & Farmer, 1996; Weed, 1889; among others), which can act as a template for sinter precipitation by providing heterogeneous nucleation sites where polymeric and/or colloidal silica can be adsorbed (Konhauser et al., 2004). However, these organic mats do not necessarily play a fundamental role in the precipitation itself, and do not enhance silica precipitation rates (Konhauser et al., 2004; Gong et al., 2022; Munoz-Saez et al., 2023). On the other hand, there are organisms that use silica as one of their main functional components, either as a skeletal structure in diatoms, radiolarians and siliceous sponges (Ikeda, 2021; Kroger et al., 2002; Müller et al., 2003), or as a result of plant cell metabolism, such as precipitation derived from transpiration that forms phytoliths (Cornelis et al., 2011; Kumar et al., 2017; Raven, 1983). However, these taxa are not abundant in hot spring environments.

1.3. Germanium as a tracer for silica precipitation mechanisms

Silica and germanium have analogous inorganic geochemical behavior, including aqueous and mineral environments, due to their similar ionic radius of 40 pm for Si and 53 pm for Ge and equal charge (+4), which allows them to show the same coordination in minerals and aqueous complexes, thus, germanium tends to replace silicon in mineral lattice sites (Froelich et al., 1985) following Goldschmidt's (1926) camouflage principle. Considering this behavior the Ge/Si ratio has been used as a tracer of silica dynamics as well as its sources in different environments, such as silicate rocks, rivers, oceans, soil, and even in biological incorporation in phytoliths, diatoms, sponge spicules, among others (e.g. Ellwood et al., 2006; Filippelli et al., 2000; Froelich et al., 1992; Jochum et al., 2017; Mortlock & Froelich, 1987; Tatzel et al., 2017) . Particularly, in hydrothermal waters the values of Ge/Si ratios are usually very high with an average of 122.2 µmol/mol when compared to freshwater 0.6 µmol/mol (Figure 1), these values can reach values up to 1080 µmol/mol in Himalayan springs (Evans & Derry, 2002).

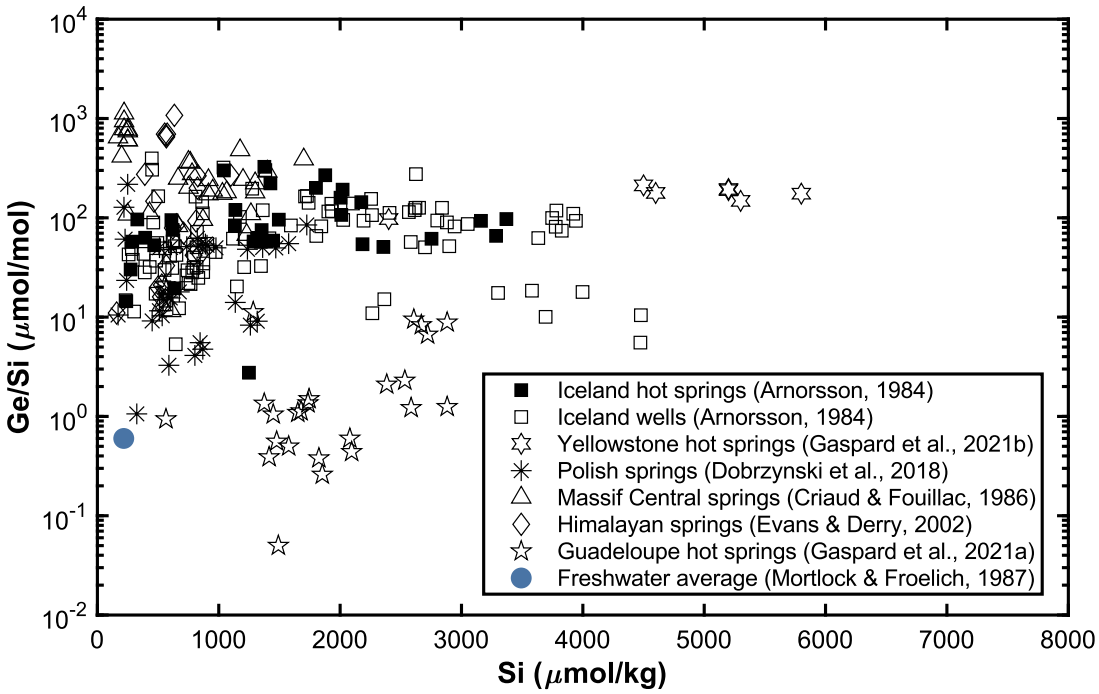

Figure 1: Compilation of Ge/Si ratios vs Si concentrations in hot springs around the world. The black solid square and the colorless square correspond to samples from hot springs and wells in Iceland, respectively (Arnórsson, 1984) The hexagram represents the Yellowstone hot springs samples (Gaspard et al., 2021b). Polish springs samples are represented by asterisks(Dobrzyński et al., 2018). Samples from Massif Central springs(Criaud & Fouillac, 1986) are represented by triangles., while samples from Himalayan springs (Evans & Derry, 2002) are denoted by squares. Samples from Guadeloupe hot springs (Gaspard et al., 2021a) are represented by stars. The light blue circle represents the average of the Freshwater (Mortlock & Froelich, 1987).

Ge/Si ratios in hydrothermal fluids depend on fluid temperature, and depletion of silica in the fluids (e.g., Arnórsson 1984; Evans & Derry, 2002). For example, research by Evans & Derry (2002) determined that quartz precipitation is a dominant factor in controlling the Ge/Si ratio in hot spring fluids in the Himalayas, as Ge/Si ratios increase due to silica removal rather than changes in Ge concentrations. In fact, in 1984, Arnórsson already stated that the Ge/Si ratio in Icelandic and New Zealand sinter silica deposits was systematically lower than in the hot spring fluids from which the deposits originate, suggesting the conservative behavior of Ge during silica precipitation. Previously, Pokrovski & Schott (1998b) established that the increase of Ge/Si ratios in the fluids with respect to temperature can be attributed to thermodynamic differences between $Ge(OH)_{4(aq)}$ and $Si(OH)_{4(aq)}$ leading to preferential partitioning of Ge with respect to Si in the fluid. According to a recent study conducted by Fernandez et al. (2021), the partition coefficients of Ge are influenced by silica precipitation rates. Specifically, under kinetically controlled conditions, the incorporation of Ge decreases as the precipitation rate decreases. Conversely, under equilibrium-controlled conditions, the partition of Ge into fluid is plausible as the silica precipitation rates are slower. This finding, derived from laboratory experiments and numerical simulations, emphasizes the potential of using germanium as a tracer in conjunction with $\delta^{30}Si$.

In addition to germanium, aluminum has also been studied in its relationship with sinters, considering that Al^{3+} can substitute for Si^{4+}. Both Ichikuni (1970) and Iler (1973) have indicated

that the presence of aluminum reduces the solubility of amorphous silica, thereby slowing down the dissolution rate of silica. Additionally, Ichikuni mentions that aluminum is incorporated into the siliceous phases. Furthermore, Yokoyama et al. (1993) have noted that aluminum is highly concentrated in the siliceous deposit despite its low concentration in thermal waters. Other investigations that study the relationship between Al and Si are associated with scaling and corrosion processes in geothermal energy (e.g. Gallup, 1998; Spinthaki et al., 2021), erosion or alteration processes (Bouchez et al., 2011; Rodgers et al., 2002) and the biogeochemical study of Al and Si cycles, as in silica of biogenic origin derived from diatoms (e.g. Liu et al., 2024).

1.4. El Tatio geyser field for investigating silica precipitation dynamics

El Tatio geothermal field, located at 4300 m.a.s.l. in the Central Andes in Chile, hosts more than 200 hydrothermal manifestations covering an area of approximately 30 km^2, with the main surface thermal features grouped within an area of 10 km^2 (Lahsen & Trujillo, 1976; Tassi et al., 2005), including geysers and perpetual spouters where fossil and modern sinter silica deposits are ubiquitous (Cortecci et al., 2005; Munoz-Saez et al., 2018). El Tatio is the largest geothermal field in the southern hemisphere and the third largest in the world (Glennon & Pfaff, 2003; Hurwitz & Manga, 2017) being specifically situated in the Altiplano-Puna Volcanic Complex (Lahsen & Trujillo, 1976; Lucchi et al., 2009; Munoz-Saez et al., 2020; Salisbury et al., 2011). Extreme environmental conditions prevail in El Tatio, including low atmospheric pressure (0.58 atm; Munoz-Saez et al., 2015; Wilmeth et al., 2020), extreme dryness due to high radiation (UV-A of 22 Wm^{-2} and UV-B of 6.0 Wm^{-2}, by Phoenix et al. (2006). The high daily oscillation of air temperature is given by a daily variation that reaches a 20°C difference, with maximum wind speeds between 4 and 6 m/s, being stronger in spring and weaker in winter, considering a data set between 2018 and 2021 (Gong et al., 2022; Munoz-Saez, 2022; Munoz-Saez et al., 2023). At the altitude of El Tatio, water boiling temperatures reach approximately 86.6°C (Cortecci et al., 2005; Cusicanqui et al., 1975; Munoz-Saez et al., 2015). Thus, silica precipitation rates at El Tatio are controlled by these extreme environmental conditions (lower boiling temperature combined with the air temperature oscillations, strong winds and high radiation) which drive fast water-cooling and high evaporation (Munoz-Saez et al., 2023). Precipitation rates in El Tatio compared to other hydrothermal systems are high, reaching up to 2.92 $kg/yr/m^2$ (Nicolau et al., 2014; Slagter et al., 2019). Therefore, the extreme environmental conditions driving fast silica precipitation rates and minimal influence of biota in silica deposition, make El Tatio geyser field an ideal location for investigating how precipitation dynamics influence trace element partitioning into opal.

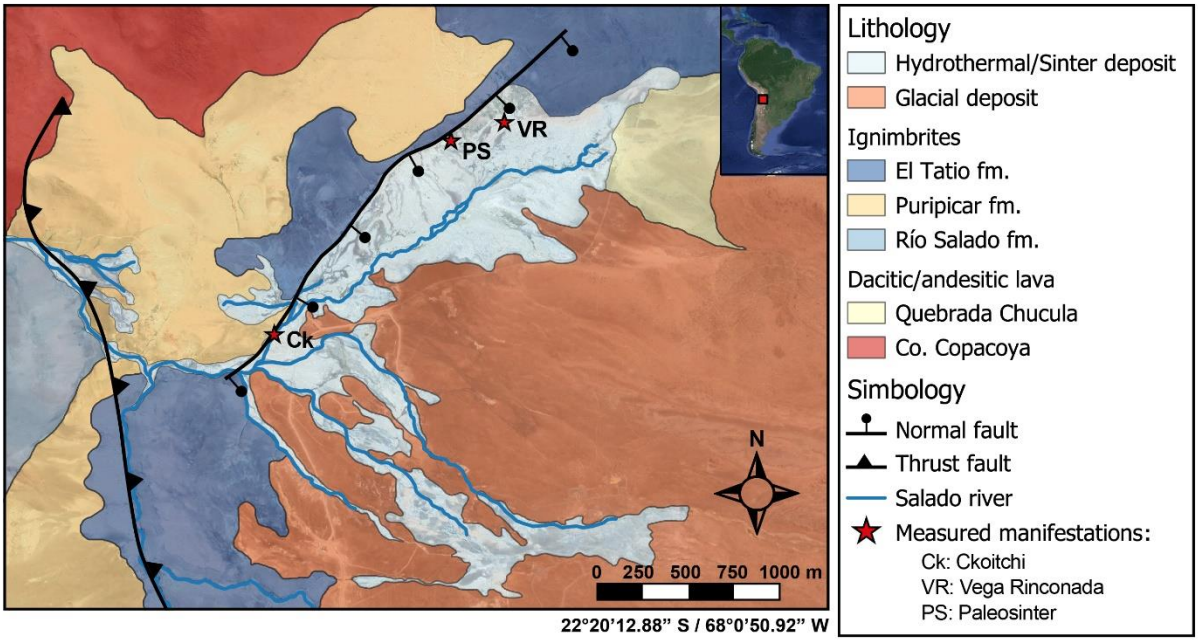

Figure 2: Simplified geological map of El Tatio geothermal field showing the two sites of interest in this study: Ckoitchi (Ck) and Vega Rinconada (VR), and the location of the paleosinter considered in this study. Modified from Lahsen & Trujillo (1976), Lucchi et al., (2009), Munoz-Saez et al. (2018, 2020), and Álvarez et al. (2023).

1.5. Hypothesis and objectives

It has been documented that Ge/Si ratios in geothermal systems show higher values due to the precipitation of Ge-poor quartz or opal (Evans & Derry, 2002) as Ge stays in the fluid. According to batch experiments of silica precipitation, this fractionation effect is enhanced during rapid silica precipitation, as the rate of Ge incorporation can be orders of magnitude lower than the rate of silicon precipitation (Fernandez et al., 2021). This study proposes that precipitation dynamics can control the incorporation of trace elements, such as Ge, substituting Si in the opal structure.

The main goal of this research is to determine the variation of the Ge/Si ratios in fluids and modern and fossil precipitates from El Tatio Geyser Field and understand the effect of environmental conditions on the behavior of Ge/Si partitioning during opal precipitation. The primary focus of the research will be to identify the mineralogy and crystalline phases present in the active siliceous sinter deposits. Following this, the study will concentrate on characterizing the physicochemical properties, determining the concentrations of major and trace elements, and analyzing the Ge/Si ratios of the associated hydrothermal fluids. In addition, the research will involve estimating the Ge/Si partitioning through fluid evaporation experiments and characterizing the remaining fluids. In-situ precipitation experiments will be carried out to estimate precipitation rates at El Tatio, and the Ge/Si ratios in active and fossil sinter deposits will be compared. These ratios will also be correlated with ages determined previously by radiocarbon dating. Moreover, the Ge/Si ratios of active sinters at El Tatio will be compared to those from other geothermal systems in Chile. Ultimately, the study aims to establish connections between Ge/Si ratios, precipitation rates, fluid temperature, and sample age.

CHAPTER 2: METHODOLOGY

To investigate the controls of Ge/Si ratios in siliceous sinters, in-situ brine evaporation and opal precipitation experiments were set up for further analyses of the evaporated fluids and silica precipitates. In addition, water samples from different hydrothermal manifestations were collected to characterize the variability of Ge/Si ratios across the El Tatio hydrothermal field. Finally, samples from fossil sinter deposits in El Tatio and two locations were collected to study the partitioning of Ge in opal across a range of extreme environmental conditions.

2.1. Hydrothermal springs sampling

In September 2021 water samples were obtained from ten thermal discharges, consisting of one perpetual spouter (named as Ckoitchi in this study), three thermal pools (Piscina Cristalina, Piscina Exp. Evap. and Piscina Linzor), and six geysers (Vega Rinconada, La Concha, El Asesino, El Horno, El Cobreloa and Géiser Corazón). During water sampling four aliquots of the hydrothermal fluid were sampled into different bottles for analyses of alkalinity, anions, cations/trace elements and silica. For alkalinity the water was extracted directly from the source (vent/pool) in deionized water-washed high-density polyethylene (HDPE) bottles, filled completely to avoid air entrapment, capped, and wrapped with parafilm. The samples for cations and trace element chemistry were collected in an acid-washed 125 ml HDPE bottles and were filtered through 0.22 μm Millipore cellulose acetate syringe filters in the field. These samples were acidified with 1.4 mL of 4M HNO3 down to pH < 2 after filtering, and were filled completely to avoid air entrapment, capped, and wrapped with parafilm. For anions analyses, we followed the same filtering protocol, and collected the samples in deionized water-washed HDPE bottles. Samples for silica and germanium were collected in an acid-washed 250 mL HDPE bottle and filtered through 0.22 μm Millipore cellulose acetate syringe filters in the field, also acidified with 2.5 mL of 4N HNO3. The samples were diluted by a factor of 10x in the field. Samples were capped and wrapped with parafilm. All samples were refrigerated at 4ºC upon returning from the field at the Geology Department, Universidad de Chile, prior to analysis.

2.2. Evaporation experiments

The evaporation experiments were performed to examine the effect of early onset silica precipitation on Al/Si and Ge/Si composition of hydrothermal fluids. For this purpose, the evaporation experiments were deployed at the Vega Rinconada geyser which corresponds to the surface hydrothermal manifestation with the highest conductivity (15.5 mS/cm) and neutral pH and silica concentrations of 319 mg/L (Munoz-Saez et al., 2015, 2018). Seven previously acid-washed graduated cylinders of 2000 mL (±20 mL) were filled with hydrothermal fluid and placed towards the SE around the vent (Figure 3) on September 25th, 2021. One test tube was sampled each following day until October 1st (2021), when the last two graduated cylinders were collected. For each tube, the remaining volume was measured each day. The collected test tubes were sampled following the same procedure described for water samples, except for alkalinity, thus, only 3 aliquots were

sampled from each graduated cylinder for silica and Ge, cations and trace elements, and anions. Prior to sampling, the remaining volume was recorded from the graduation marks in the cylinder and temperature was measured with an infrared thermometer at the surface of the cylinder. After collecting the water sample, cooled temperature, pH, conductivity, and TDS were measured with a calibrated hand-held multimeter.

2.3. Silica precipitation experiments

In-situ silica precipitation experiments were deployed at El Tatio to determine silica precipitation rates and the effect of environmental conditions on the behavior of Ge/Si. This experiment was carried out in two hydrothermal vents with different hydrodynamic characteristics and fluid compositions: the first site corresponds to a perpetual spouter identified as Ckoitchi (Ck) in this study, which was previously described as site 411 in Slagter et al., 2019); and the second site is the Vega Rinconada (VR) geyser, same location as the evaporation experiments. At each site six and four sampling points were selected respectively, to create a temperature gradient along the main discharge channel for each vent. The temperature gradient allows to investigate precipitation rates across different environmental settings in hot spring as described by Lynne (2012). The location of each point is illustrated in Figure 3.

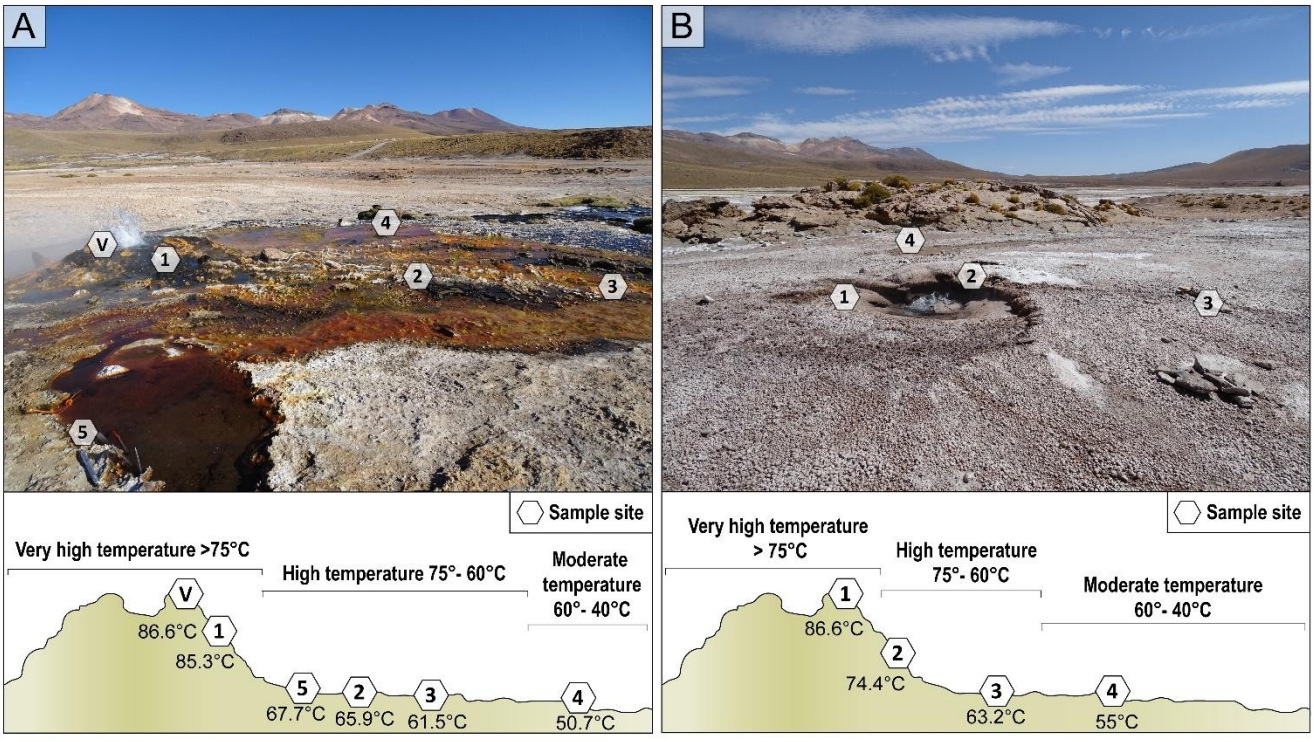

Figure 3: Location of sampling points for the precipitation experiments. (A) Top panel shows photograph of the position of the experiments around Ckoitchi (perpetual spouter). Bottom panel includes a schematic profile of the points with their respective daily average temperatures. (B) Top panel shows photograph of the Vega Rinconada sector and the position of the experiments. At the bottom, the respective schematic profile with their respective daily average temperatures. Both profiles were modified from Guido & Campbell (2011) and are not to scale.

Ckoitchi is a perpetual spouter with a sinter mound of ~0.15 m high and almost 0.5 m in diameter, notably surrounded by orange/green biofilms (Figure 3A). At each point selected for Ckoitchi, temperature sensors were installed for one week, from which the average temperature was obtained (Table 1). On the other hand, Vega Rinconada (Figure 3) is an active geyser with a vent diameter of 0.3 m (Munoz-Saez et al., 2015) opening to a small pool of about 1 m in diameter. For Vega Rinconada, temperatures were measured during the main eruption of the geyser, which causes the activation of the channels adjacent to the vent, allowing the temperature to be measured when water flows using an infrared thermometer. For more details on each sampling point, see Table 1.

Table 1: Characteristics of the sampling points of this study, considering the distance to the vent, temperature, and pH of the fluid, along with observations of the respective location.

Site	Sample point	Distance from the vent	Temperature of fluid	pH of fluid	TDS	Observations
		m	°C		mg/L	
Ckoitchi (Ck)	Ck-Vent	0	86.6	6.16	9749	Perpetual spouter vent.
	Ck-1	0.2	85.3	-	-	Splash zone of the vent at the NW.
	Ck-2	1.6	65.9	6.66	9892	Fast flowing channel to the NW from the vent, with presence of orange biofilms.
	Ck-3	2.8	61.5	6.32	9908	Fast-flowing channel to the NW from the vent, with presence of orange/green biofilms.
	Ck-4	3.8	50.7	6.63	9876	Apron area to the SW from the vent.
	Ck-5	2.3	67.7	4.82	10287	Little thermal pool, aligned with Ck to the NW from the vent.
Vega Rinconada (VR)	VR-1	0	86.6	6.25	14960	Geyser vent, with a cycle time between 1.4-2 hrs. (Munoz-Saez et al. 2015).
	VR-2	0.2	74.4	-	-	Splash zone of the vent at the W.
	VR-3	2.8	63.2	6.16	15286	Channel to the NW from the vent, intermittent overflow area.
	VR-4	4.2	55	6.26	15202	Superficial pool to the SW from the vent, formed by the fast-flowing channel during eruptions.

The silica precipitation experiments were carried out during 203 to 210 days, between September 24th (2021) and April 22nd (2022). Prior to their installation in the field, the glass slides were manually sanded to increase their surface area and roughness. After sanding or glueing the sandpaper, the slides were weighed in the laboratory before installation using a Precisa 40SM-200A Precision Digital Scale Balance. On each sampling point, three glass slides (25.4 x 76.2 mm microscope slides) and one glass slide covered with sandpaper were placed vertically and perpendicular to water flow, except for Point 1 (VR-1) and Point 3 (VR-3) of discharge channel in Vega Rinconada where they were placed horizontally. To secure the slides at each point, these were fastened to heat-resistant plastic racks or secured with wire. After ~200 days, the samples were collected and stored in either 50 mL centrifuge tubes or 100 mL sterile polyethylene containers.

Upon return to the lab the samples were left to airdry at room temperature before weighing them to determine the weight of the precipitated material by subtracting the previously measured slide weight. First, the maximum silica precipitation rates (kg/day) were calculated assuming a continuous precipitation process since the installation of each slide, no re-dissolution, and that silica is the only material that accumulates (Slagter et al., (2019). To normalize the precipitation rates to area (kg/day/m^2), the effective precipitated area in each slide was determined by discarding the areas without precipitate based on a detailed photographic analysis of each scanned slide, the calculation was performed considering Eq. 2, where A_{Ep} corresponds to the effectively precipitated area, A_o is the original area of the glass slide (1935.48 mm^2) and A_{np} is the non-precipitated area.

$$A_{Ep} = A_O - A_{np} \quad (2)$$

This is necessary, because silica deposition is irregular across each slide, where each area may differ from one sample to another depending on the position, height of the water-air interface, water flow or presence of biological material for example. Therefore, for the calculation of the bulk precipitation rate, the weight of the precipitated material must also consider the effective area of the precipitated material, then, the weight of the precipitated material (or bulk precipitate, P_{Bulk}) is given by:

$$P_{Bulk} = \text{Dry precipitate} - \text{Glass slide} \times PA_{Ep} \quad (3)$$

Where Dry precipitate is the sum of the weight of the glass slide and the precipitate after air drying, Glass slide is the measured weight of the glass slide before field installation, and PA_{Ep} is the effective area expressed as a percentage. Finally, the bulk precipitation rate is expressed according to Eq. 4, where t_{Precip} represents the time duration of the precipitation experiment.

$$\text{Bulk silica precipitation rate} = \frac{\frac{P_{Bulk}}{t_{Precip}}}{A_{Ep}} \quad (4)$$

If silica is not considered to be the only material precipitating in the experiment, an adjustment to the bulk precipitation rate should be made by correcting with the measured silica concentration (in wt.%). This correction can be critical when there is excess organic material, precipitation of other phases, or detrital material.

2.4. Fossil and in-situ sinter deposit sampling

To evaluate Ge/Si ratios in both fossil and active silica sinter deposits, seven samples were taken from fossil deposits that represent former outflow zones from a paleosinter mound (site 404) described in Slagter et al. (2019), and fourteen samples were extracted from active deposits at El Tatio (Ckoitchi, Piscina Linzor and Vega Rinconada). The paleo sinter samples obtained from site 404 followed Slagter et al. (2019) using our own nomenclature. The volume of each sample was about 10 cm per side. The samples of active deposits were obtained from the same points as in the precipitation experiments, including an additional point located 12 m from the vent in Ckoitchi. In addition, four extra samples were considered for the fossil deposits, two coming from the study of Slagter et al. (2019) and two from Munoz-Saez et al. (2020). For active sinter deposits, four samples from Slagter et al (2019) and ten samples from Munoz-Saez et al. (2020) belonging to El Tatio were also analyzed, together with samples coming from other geothermal fields, four samples from the Alpehue geyser field (Pérez Nuñez, 2019), and five samples from the Puchuldiza geothermal field (Sanchez-Yanez et al., 2017).

Examples of the in-situ experiments and sinters sampled for this study can be found Figure 4 and Figure 5. The Ckoitchi zone (Figure 4a) displays a distribution of microbial communities along the temperature gradient, similar to the research conducted by Megevand et al. (2022) in another hot spring at El Tatio. In this area, precipitation experiments (e.g., Figure 4b) revealed variations in the color associated with the presence of these organisms (e.g.,Figure 4c). Furthermore, extracting in-situ sinters requires careful consideration due to the abundance of these organisms (Figure 4d).

In the Vega Rinconada experiment (Figure 5a), there is no apparent presence of bacterial communities, unlike in Ckoitchi. Additionally, the experiment samples (Figure 5b) do not display any color variation apart from silica (Figure 5c). It's also worth noting that even in-situ sinter sampling is much easier compared to Ckoitchi (Figure 5d).

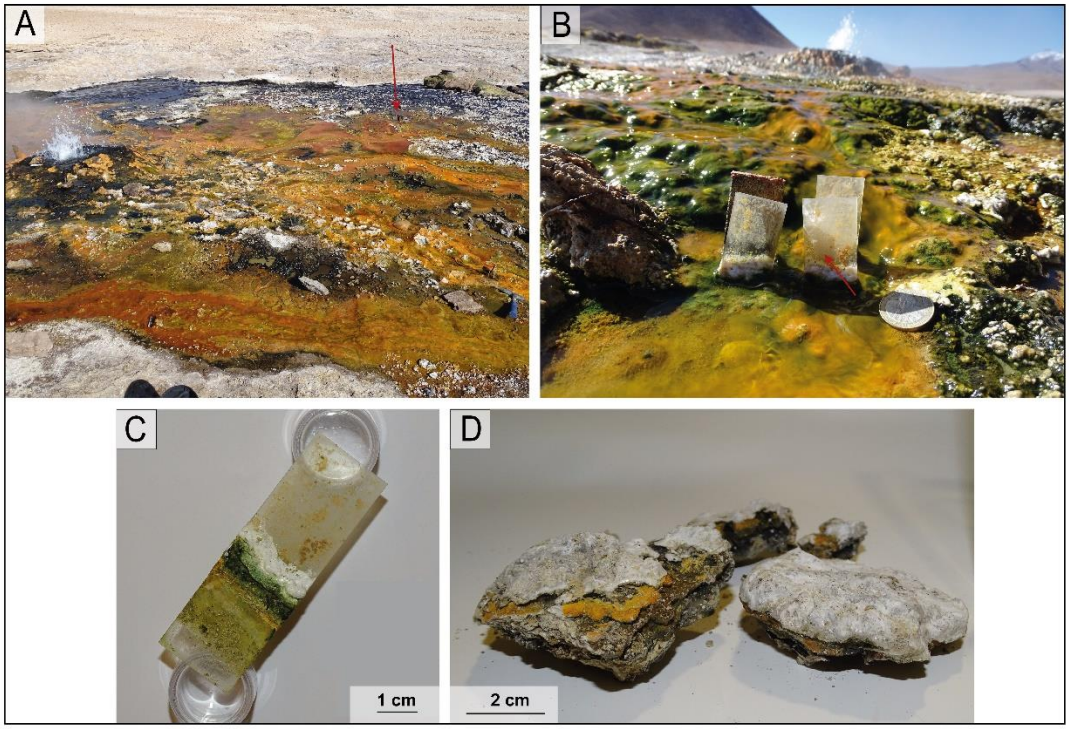

Figure 4: Images associated with the Ckoitchi zone, showing (A) a general view of some of the sampling points, with the red arrow indicating point Ck-4, (B) a close-up of the precipitation experiment at point Ck-44, almost 7 months after its implementation, the red arrow indicates the precipitate (C) denominated Co04-15 and (D) samples of in-situ sinter deposits at that point.

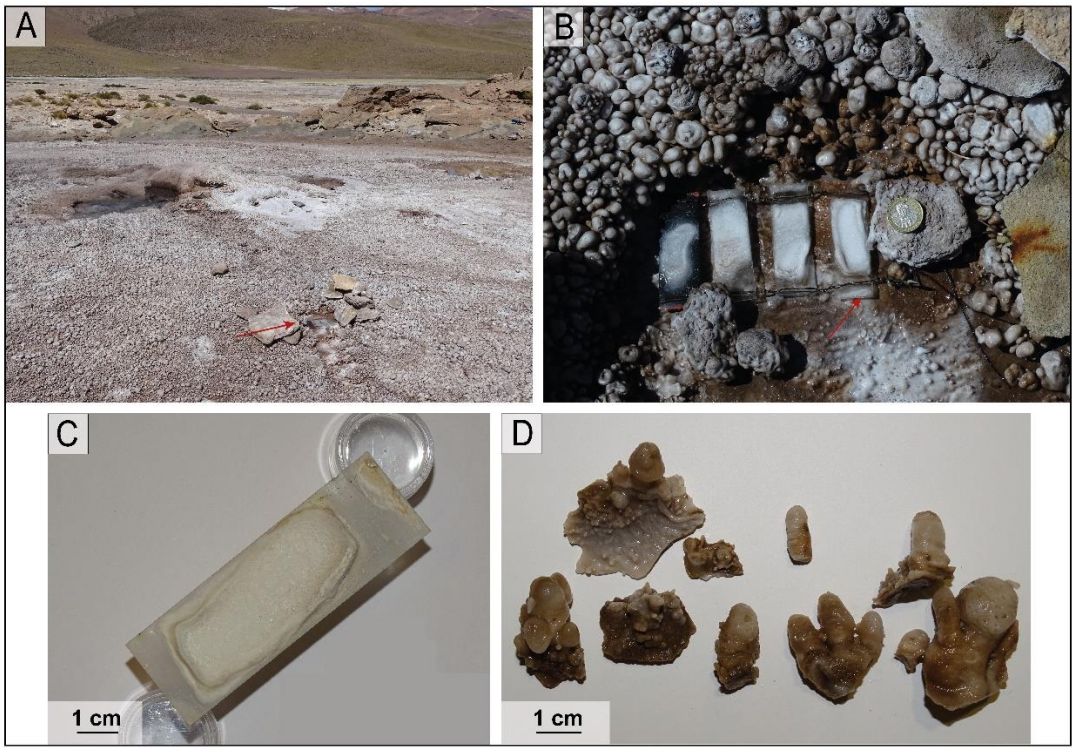

Figure 5: Images of the Vega Rinconada area, showing (A) an overview of the geyser surroundings, with the red arrow indicating sampling point VR03, (B) a close-up of the experiment at VR-3, with the red arrow indicating (C) the VR03-27 precipitate, and (D) samples of in-situ sinter deposits at that point.

2.5. Opal alkaline digestions

Due to the impurities such as dust grains or organic matter present in modern and fossil sinter deposits, it is important to separate just the silica components of these deposits to analyze their trace element geochemistry. Particularly, dust grains containing clay, iron oxides or sulfides can contain significant amounts of Ge, and thus can bias our interpretation of trace element partition into the opal (e.g.,Bernstein, 1985; Kurtz et al., 2002; Mortlock & Froelich, 1996). Thus, to analyze the trace element composition of the opal, an alkaline extraction method adapted from Mortlock & Froelich (1996) was used to purify the silica. This methodology consisted of dissolving between 10 to 25 mg of sample in 125 to 250 ml of sodium carbonate solution (2M Na_2CO_3) to reach a silica concentration of <100 ppm (below silica saturation at 25ºC). After weighing the samples, the impurities are removed by several steps of sequential leaching and weight measuring the samples, before the dissolution in sodium carbonate step. The first leach uses 30%wt hydrogen peroxide and 1N nitric acid, followed by sonification of the samples to let carbonates and organic matter react. After this, the samples are rinsed with deionized water and centrifuged to remove the supernatant from the precipitated solids (including opal, clays, iron oxides and sulfides). The supernatant is discarded before following with the alkaline dissolution step, and the precipitate is transferred to previously acid-washed 250 mL bottles, and 250 mL of 2M Na_2CO_3 were added. The bottles were capped and placed in a hot bath at 80-85°C for about 10 days. The samples of Ck followed the same procedure but using 125 mL bottles and 125 mL of 2M Na_2CO_3. Upon collection, an aliquot of the sample was neutralized with 65% nitric acid (down to pH < 6) before proceeding with the geochemical analyses. Details of each step can be found in the ANNEX A.

The alkaline extractions for the active and fossil sinter samples were performed in January 2022 and December 2022 (eleven months later), with some of the January samples being replicated in December. The alkaline extractions for the precipitates occurred in January 2023, and the silica concentration analyses using the molybdenum blue method for all samples was completed in January 2023.

2.6. Geochemical analytical methods

Major cations in opal and silica concentrations in the fluids were measured by inductively coupled plasma optical emission spectrometry on a SpectroBlue ICP-OES (Ametek, Kleve, Germany) at the Geochemistry Lab in Cornell University. Anions, trace elements and alkalinity (HCO_3, CO_3^2) were analyzed at the Fluid Geochemistry Laboratory in the Department of Geology, University of Chile. Anion concentrations were determined by ion chromatography using a Thermo Scientific Dionex™ ICS-2100 Ion Chromatograph with Dionex IonPac™ AS11-HC RFIC™ analytical 4 x 250 mm column, Dionex IonPac™ AG11-HC RFIC™ 4 x 50 mm pre-column. Carbonate and bicarbonate species concentrations were analyzed using the Giggenbach (1988) method in a Hanna HI-902C automatic titrator with a combined glass electrode. Trace element concentrations in the fluid samples were measured through mass spectrometry with a quadrupole ICP-MS Thermo Scientific Q-iCAP. Reactive silica concentrations in the opal samples were determined using the molybdenum blue colorimetric method (Geilert et al., 2014; Iler, 1979) using VWR Spectrophotometer UV-1600 PC at Cornell University. Aluminum or other major elemental concentrations in the opal were not measured because the high sodium matrix of the alkaline extractions

prevented measurement of these solutions using ICP-OES, due to dissolution of the quartz torch at the Geochemistry Lab at Cornell University. No attempts were made to purify the matrix.

Germanium concentrations in the both the fluid and the sinter samples were measured using hydride-generation ICP magnetic sector mass-spectrometry (HG-ICP-MS) (Mortlock & Froelich, 1996 Aguirre et al., 2017). The hydride generator sample introduction system used corresponds to an HGX-200 from Cetac-Teledyne. The system uses a 0.27 M sodium borohydride in ammonia solution ($NaBH_4$ powder trace grade from Thermo Scientific) and a 3 M nitric acid (Aristar Plus, trace grade quality). Ge in the fluid samples was determined through a standard calibration curve using Ge standards of 5, 10, 20, 50, 100, 250 and 500 ng/L at Cornell University using a Thermo Finnigan Element 2 magnetic sector ICP-MS with < 5% accuracy. The dissolved opal samples were quantified using isotope-dilution (ID-HG-ICP-MS) using an enriched ^{70}Ge spike to target a 70/74 ratio in the sample close to 10. These analyses were carried out using a Thermo Scientific Element II magnetic sector HR-ICP-MS at the PARI High Resolution Analysis Platform located at the Institut de Physique du Globe de Paris (IPGP). These analyses obtained an average uncertainty of ~5%.

Mineralogical characterization of ten opal samples for both active and fossil sinters was carried out by X-ray diffraction at the Andean Geothermal Center of Excellence (CEGA), in Universidad de Chile. An aliquot of the powdered samples was used to determine the mineralogy and the corresponding siliceous phase. The XRD analyses were performed using a Bruker D2 Phaser diffractometer, using Cu-Kα radiation, a voltage of 30 kV, and an applied current of 10 mA, and the samples were analyzed at angular domains of 5–80°2θ. The bulk-sample XRD diffraction patterns were treated and interpreted using the DIFFRAC.EVA software, which incorporates multiple reference databases (e.g. ICDD PDF2/PDF4+/PDF4 Minerals/PDF4 Organics databases). Additionally, the XRD pattern of sample ET03-Co01 showed a clear presence of clay minerals, so further mineral identification, the mineralogy < 2 μm fraction was studied using clay separation methods. Sample chip was washed in distilled water to remove salts, treated to remove organic matter and calcite, separated by centrifugation, and mounted in oriented aggregates following the recommendations of Moore & Reynolds (1997). Clay-mineral analysis was carried out between 4.5 and 39°2θ, with a step size of 0.006°2θ and a scanning time per step of 152 s. The minerals in the clay fraction were identified according to the position of the basal reflections of air-dried (AD), ethylene-glycol solvated (EG), and heated to 500°C for 1 h (H) XRD patterns, using the criteria of Moore & Reynolds (1997).

2.7. Reflected light petrography and scanning electron microscopy analyses

Three active sinter samples (from vents of Ckoitchi and Vega Rinconada, and sinter of Piscina Linzor) and samples from the precipitation experiment (nine samples, one per position without considering the Ckoitchi vent) were coated in epoxy resin, cut, and polished for petrographic analysis in optical microscopy and scanning electron microscopy (SEM). The samples were inspected under a Leica DM2700P Polarization Microscope by reflected light and the photographs were taken using a Nikon D5600 camera. SEM observations were carried out using a FEI Quanta 250 SEM equipped with backscattered electron (BSE) energy-dispersive X-ray spectrometry (EDS), and secondary electron (SE) detectors, at the Andean Geothermal Center of Excellence (CEGA),

Universidad de Chile. The operating conditions were a spot size of 5 μm, accelerating voltage of 20 kV, beam intensity of 1 nA and a working distance of ~9.5-10 mm.

CHAPTER 3: RESULTS

In this chapter, the findings of this study are organized into five subsections, considering the different methodologies used in this research for the study of Ge/Si ratios. First, the mineralogy of the siliceous sinters is introduced, followed by the geochemical composition and Ge/Si ratios of the hydrothermal fluids at El Tatio. Fluid evaporation experiments are then addressed, followed by silica precipitation experiments. Then, the active sinter and fossil deposits of El Tatio are reported considering their geochemistry and Ge partitioning. Finally, the geochemistry of active sinter deposits from other geothermal fields is provided.

3.1. Mineralogy of siliceous sinters

A total of nineteen samples were analyzed for mineralogical characterization, of which nine were considered for X-ray diffraction (XRD) and twelve for scanning electron microscopy (SEM), being two samples used in both analyses, those corresponding to the Ckoitchi and Vega Rinconada vents (ET03-Co01 and ET02-VR01 respectively). Seven samples from the fossil deposit (paleo-sinter mound of site 404) described by Slagter et al. (2019) were considered for the XRD samples, apart from the active sinters from the Ck and VR vents. For each sample, the curve and baseline were fitted manually to measure the Full Width at Half Maximum (FWHM) and determine the degree of silica crystal lattice order/disorder (Herdianita et al., 2000a; Herdianita et al., 2000b; Lynne et al., 2005). The resulting bulk-sample X-ray diffraction patterns for the active and fossil samples show peaks between 4.02 and 4.01 Å for all the samples except ET03-Co01, which shows a different pattern than the other samples and whose peak is shifted to 3.34 Å. Opal in all the analyzed samples corresponds to the Opal-A (Table 2), characterized by a wide peak centered at ~4.0 Å broad band extending from 15 to 30° 2θ and FWHM values ranging from 5.8° to 7.7° 2θ (Flörke et al., 1991; Herdianita et al., 2000b; Lee et al., 2022; Liesegang & Tomaschek, 2020; among others). Only one sample showed the presence of clay minerals (sample ET03-Co01), of which smectite was identified, by the peak shift from ~10.8 Å to 17.0 Å after EG solvation, and collapse to 10 Å after the heat treatment (Moore & Reynolds Jr, 1997), and illite, identified by the 10.0 Å reflection on AD preparations, which are not displaced after the EG and H treatments (Figure 6).

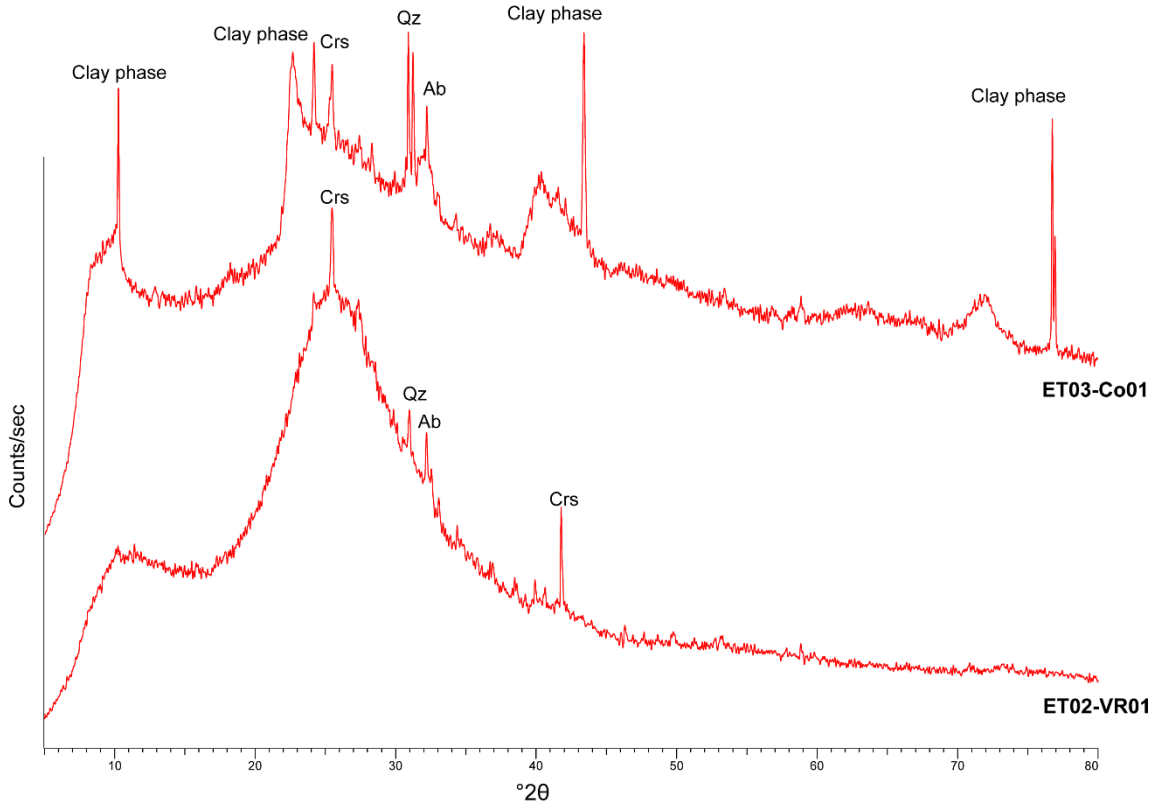

Figure 6: XRD spectrum of active sinters of the vents from Ckoitchi (ET03-Co01, spectrum at the top) and Vega Rinconada (ET02-VR01, spectrum at the bottom). The broadband of VR is centered in 25.6°2θ. The accessory minerals identified correspond to albite (Ab), detrital quartz (Qz), and cristobalite (Crs), which contributes to the identification of the samples as Opal.

Table 2: XRD parameters and phases identified for the fossil sinter (first group of samples, sinter mound 404 in Slagter et al., 2019) and for the Vega Rinconada and Ckoitchi vents (last two samples). The minerals correspond to cristobalite (Crs), albite (Ab), quartz (Qz) and biotite (Bt).

Sample Name	Peak Position	Maximum intensity	FWHM	Silica phase	Other minerals			
	Å	counts/sec	2°θ					
ET06-Psa	4.05	1021	7.571	Opal-A	Crs		Qz	
ET06-PSb1	4.10	981.674	7.649	Opal-A	Crs			
ET06-PSb2-a	4.05	1062.117	7.025	Opal-A	Crs	Ab	Qz	
ET06-PSb2-b	4.07	977.936	7.103	Opal-A	Crs			
ET06-b3	4.07	1020.023	7.337	Opal-A	Crs	Ab		
ET06-PSc1	4.07	998.365	7.921	Opal-A	Crs		Qz	Bt
ET06-PSc2	4.05	951.298	7.727	Opal-A	Crs	Ab	Qz	
ET02-VR01	4.05	880.898	6.364	Opal-A				
ET03-Co01	3.34	990.48	1.122	Opal-A				

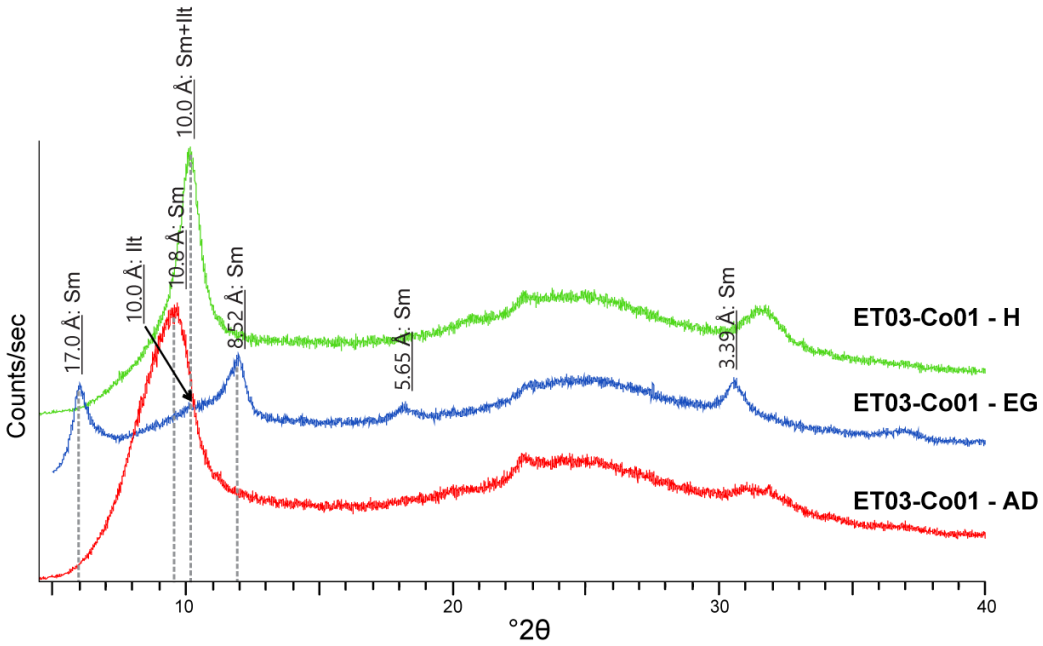

Figure 7: XRD spectra for the analysis of clays in the ET03-Co01 sample according to the criteria of Moore and Reynolds (1997). From the bottom, the spectra of air-dried (AD, red spectrum), ethylene-glycol solvated (EG, blue spectrum), and heated (H, green spectrum) respectively. Illite (Ilt) and smectite (Sm) were identified.

Regarding the paleosinter samples, Table 2 presents the names used in this work and the equivalent names for the samples of Slagter et al. (2019), along with their respective radiocarbon ages. The analyses of the paleosinter samples (Figure 8) are consistent with the phases obtained in Slagter (2019). However, more crystalline phases than Opal-A/CT were not found here. It was possible to recognize more accessory minerals besides detrital quartz, such as albite and biotite. Moreover, consequently, also the results are comparable with those previously obtained by Fernandez-Turiel et al. (2005), Garcia-Valles et al. (2008), Munoz-Saez et al. (2016), Nicolau et al. (2014) and Sanchez-Garcia et al. (2019).

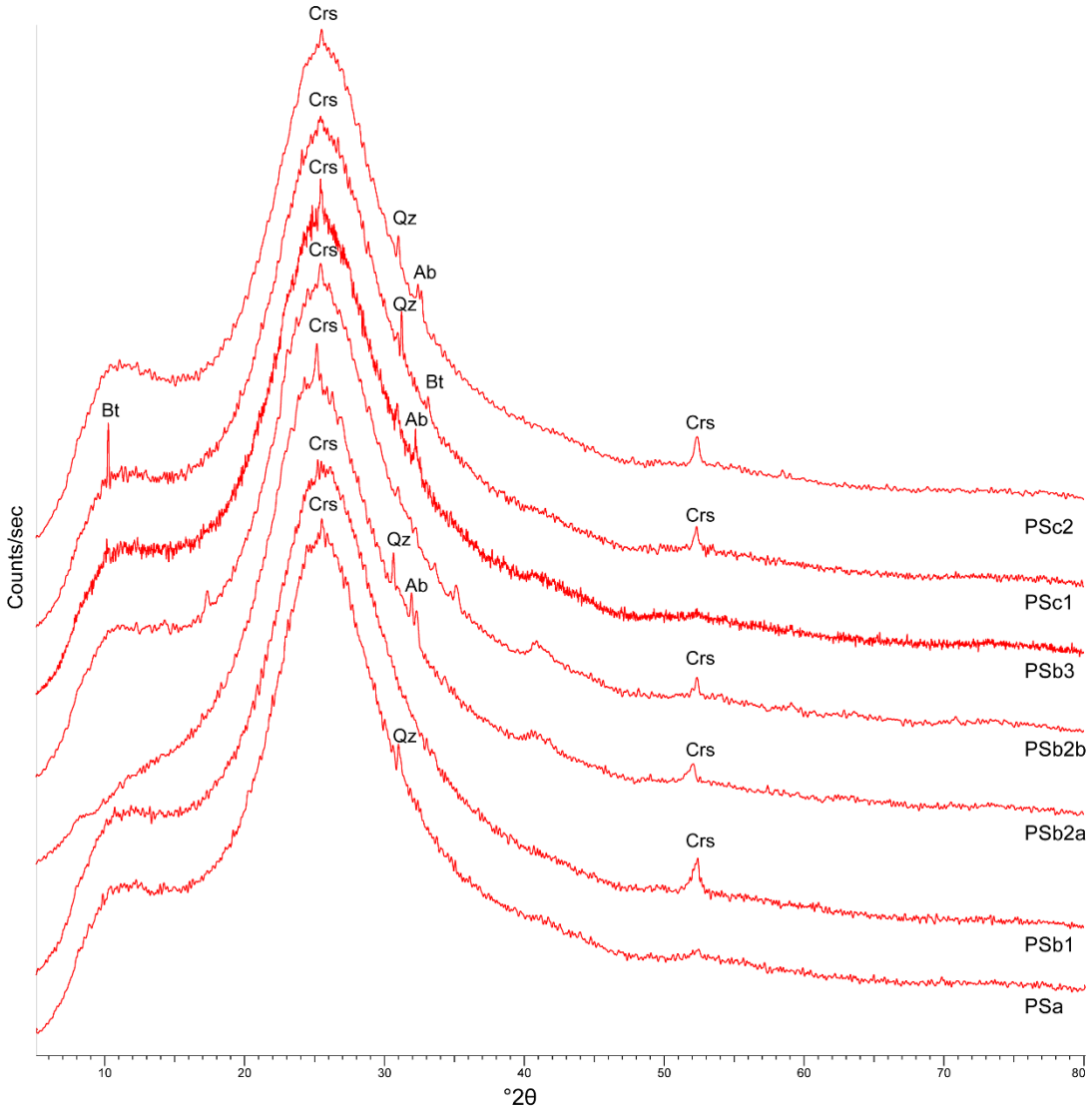

Figure 8: XRD spectrum of paleosinter (sinter 404 of Slagter et al., 2019). The broadband is centered around 25°2θ for all samples. The accessory minerals identified correspond to albite (Ab), biotite (Bt) and detrital quartz (Qz), in addition, cristobalite (Crs) is identified, which contributes to the identification of the samples as opal.

Table 3: Names assigned to Paleosinter samples in this work and their corresponding designation by Slagter et al. (2019), along with the ages obtained there.

Nomenclature		**Radiocarbon ages (Slagter et al. 2019)**	
This Work	**Slagter et al. (2019)**	**14C yr B.P.**	**±**
ET06-PSc2	404a	5860	25
ET06-PSc1	404b	6330	80
ET06-b3	404c	8230	140
ET06-PSb2-b	404d	8550	50
ET06-PSb2-a	404d	8550	50
ET06-PSb1	404e	9340	30
ET06-Psa	404f	10840	30

SEM analyses were performed on three samples from active sinter deposits (ET03-VR01, ET03-Co01 and ETLIN02) and nine samples from precipitation experiments, four of which correspond to samples from Vega Rinconada. Backscattered electrons (BSE) were used to capture images of the samples and identify the areas for qualitative chemical analysis. Subsequently, energy-dispersive X-ray spectrometry (EDS) was employed to recognize the primary chemical components present. In general, the samples display diverse features that enable distinction between Vega Rinconada and Ckoitchi. The Ck samples present mostly thin intercalations of silica laminations and silicified bacterial mats, as shown in Figure 9A, where the silica laminations are composed of silica microspheres, which also coat the filaments present (Figure 9B). In comparison, the VR samples are composed mostly of massive silica layers (Figure 9C-D). These layers also show the presence of bacterial filaments, but they either fill cavities or are present in the outer layers (Figure 9C). They are not part of the laminations; if present, these would likely be detrital material deposited during specific time intervals (Figure 10A).

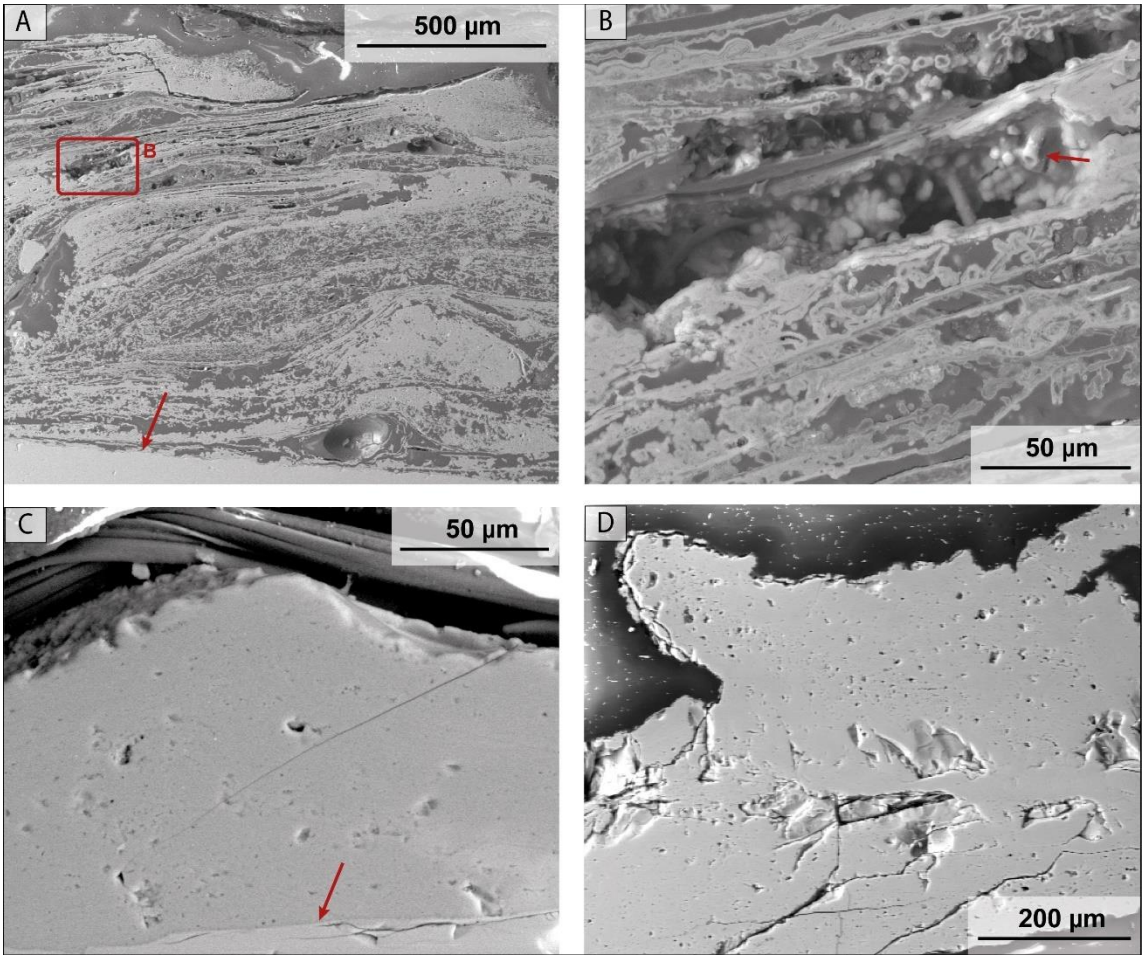

Figure 9: Cross-sections of the sinter deposits from the in-situ precipitation experiment. The images are oriented with the glass slides at the bottom and the growth of the sinter upwards. (A) SEM photomicrograph of sample Co04-15 showing sinter laminations. The lower arrow indicates the boundary between the glass slide (bottom) and the precipitate, while the upper inset corresponds to the image in B. (B) Enlarged rectangle showing silicified microbial filaments and a cavity with silica microspheres. The arrow indicates a sheathed filament. (C) SEM image of sample VR01-21 showing a massive silica layer, together with free microbial filaments on top of the glass slide. The red arrow indicates the boundary between the glass slide (bottom) and the precipitate (top). (D) SEM photomicrograph of sample VR02-49 composed mainly of massive silica and exhibiting a microspicule.

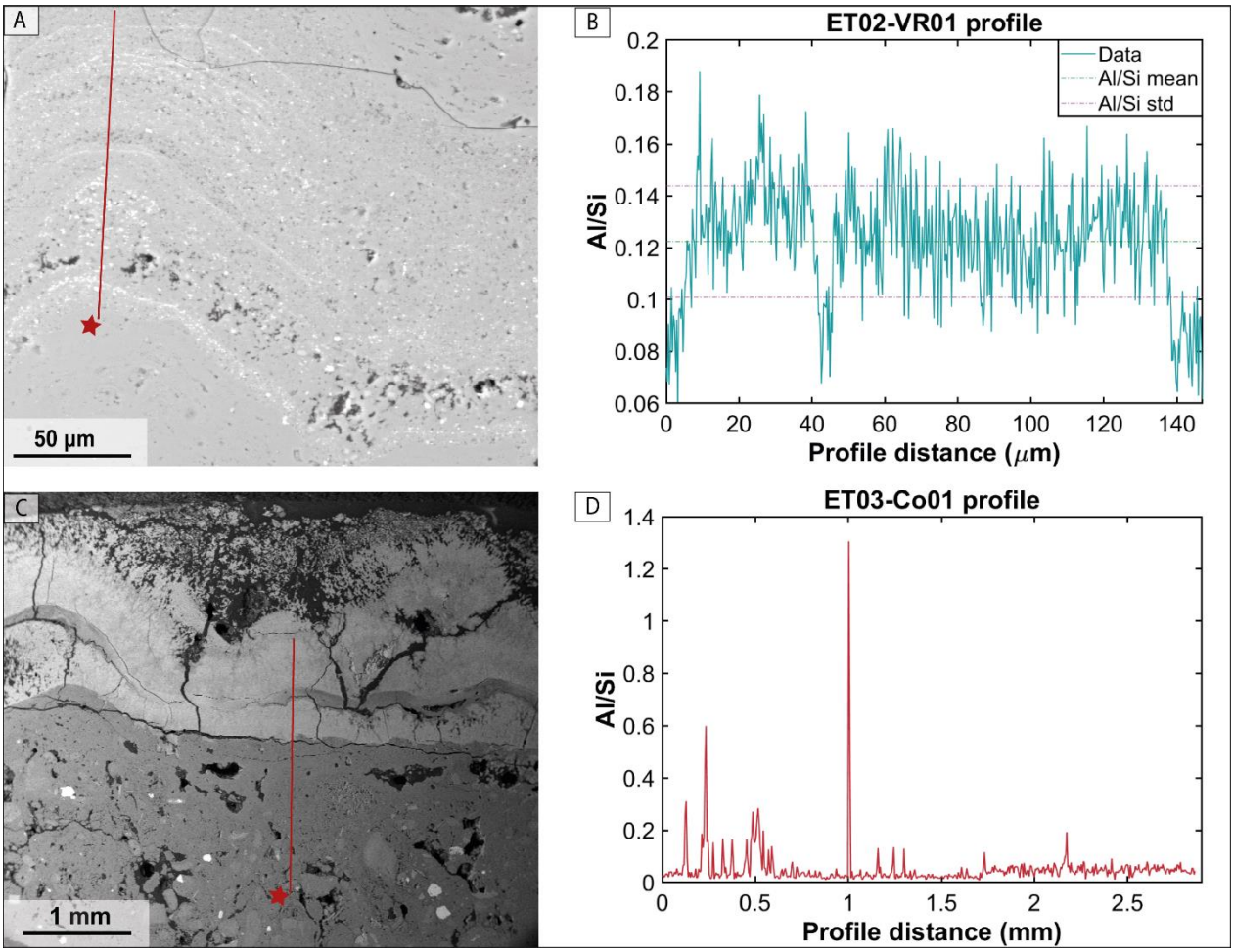

Figure 10: SEM images of samples ET02-VR01 (A), ET03-Co01 (C) and their respective resulting profiles (B and D) of the Al/Si ratios obtained by EDS analysis. Each line represents where the profile was performed and the small lower star indicates the starting direction of the profile, i.e., the initial distance 0.

Regarding the qualitative analysis of the samples, each sample was subjected to either a point, profile, or map analysis, depending on the characteristics of the sample (the detailed table of analyses can be found in Tables 17 in ANNEX C. Point EDS analysis was performed on the most homogeneous samples in the BSE analysis. Through profile analysis, it was determined that sample ET02-VR01 (Figure 10A) contained 84.73 wt.% SiO_2, while ET03-Co01 (Figure 10C) contained 79.35 wt.% SiO2. Additionally, the point analysis for samples VR01-21 (Figure 9C) and VR02-49 (Figure 9D) revealed 97.65 wt.% and 96.76 wt.% of SiO_2, respectively, for the precipitates. In contrast, sample Co04-15 (Figure 9A) displayed a SiO_2 content of 42.89 wt.%, which was comparatively lower. This discrepancy could be attributed to the presence of laminations within the sample. When polished and analyzed, a significant portion of the profile aligned with the interlaminar zones, which could have been filled with resin. Regarding sample ET02-VR01 from the Vega Rinconada vent, it exhibits a relatively consistent composition, except for some debris (Figure 10A). Furthermore, when considering measurements of aluminum and silicon in the sample and calculate the Al/Si ratio (Figure 10B), it is observed that the Al/Si values remain consistent at an average of 0.12. In other words, the ratio stays relatively constant, and any variations observed may be due to the existence of material external to the precipitated opal. On the other hand, the sample of the

Ckoitchi vent (ET03-Co01, Figure 10C) shows two colorations. The lighter color represents a bacterial mat at the top, at the sinter-air interface. The darker color in the lower part, closer to the center, corresponds to a silicified deposit. This deposit contains a mixture of different detritus in the lower part, while the upper layer consists of a more recent, cleaner-looking sinter with fewer cavities. The Al/Si values for this sample (Figure 10D) are elevated at specific points that are not directly linked to the sinter (lower zone, associated with the bedrock). Despite the compositional disparity between the bacterial and siliceous parts, the ratios between the two do not fluctuate significantly, remaining consistently less than 0.2 in value. This consistency is similar to the VR vent sample.

3.2. Geochemical composition and Ge/Si ratios of hydrothermal fluids across El Tatio

The physicochemical parameters, major and trace element compositions of hydrothermal fluids of interest at El Tatio are detailed in Tables 4 and 5. Geothermal fluid temperatures measured in this study range from 50.9° to 86.6°C, with pH ranging from 4.8 to 7.7 (Table 4). Based on the concentrations of major ions in the samples, they are classified as Na-Cl type waters (Figure 56 in ANNEX C) according to the Piper classification (Piper, 1944). Some distinguishing features can be observed upon examining the samples based on the type of hydrothermal manifestation. The different sample groups correspond to geysers (La Concha, El Asesino, El Horno, El Cobreloa, Geyser Corazón, Vega Rinconada, with Vega Rinconada being analyzed independently), thermal pools (Piscina Cristalina and Piscina Exp. Evap.), and the perpetual spouter at Ckoitchi. For temperatures, the geysers fluctuate between 83.7° and 86°C, the thermal pools average 53.6°C (Table 4). The temperature at the Ckoitchi and Vega Rinconada vents is 86.6°C. The specific conductivity is higher in the geysers, reaching in average 18904 µS/cm, the pools on the other hand average 17898 µS/cm. Vega Rinconada has an average specific conductance of 22955 µS/cm in the vent (considering the average of samples ET-002 and ET-025 in Table 4), while the Ckoitchi vent presents the lowest value in comparison with 14773 µS/cm in average (considering the samples ET-001 and ET-026 in Table 4). The major constituents of these waters are Na^+ and Cl^-. Na^+ concentrations in the geysers range from 2491.3 to 4608.5 mg/L, while the pool range is 3753.8-4849.1 mg/L. The Ckoitchi and Vega Rinconada vents have Na^+ concentrations of 3107.7 and 4026.2 mg/L, respectively. Chloride concentrations in the geysers range from 3765.2 to 7549.9 mg/L; in the pools, they range from 5845.6 to 7872.9 mg/L. The chloride concentration in the Ckoitchi vent averages 4704.73 mg/L; in the Vega Rinconada vent, it is 7760.27 mg/L. In terms of the elements of interest in this study, silica concentrations in the geysers range between 161.9 and 344.6 mg/L, the pools between 210.6 and 369.4 mg/L. While the VR vent has an average silica concentration of 313.3 mg/L and the Ckoitchi vent of 223.0 mg/L. On the other hand, germanium concentrations (Table 5) for the geysers vary between 18.7 and 25.9 µg/L, and for the thermal pools, concentrations range between 26.5 and 28.8 µg/L. While the Ckoitchi vent has a germanium concentration of 30.2 µg/L and the Vega Rinconada vent 36.1 µg/L.

Table 4: Composition of hydrothermal fluids from El Tatio. The table includes in-situ physicochemical parameters (T°, pH, specific conductivity (SPC)) and major ions composition. Temperatures are in °C, specific conductivity (SPC) in µS/cm. concentrations are expressed in mg/L. nd: no detected, '-': unmeasured.

Sample ID	Location	T °C	pH	SPC µS/cm	Ca mg/L	Mg mg/L	Mn mg/L	Na mg/L	SiO_2 mg/L	F^- mg/L	Cl^- mg/L	SO_4^{-2} mg/L	Br^- mg/L	NO_3^- mg/L	PO_4^{-3} mg/L	HCO_3^- mg/L
ET-001	Ck-Vent	86.6	6.2	14995	198.2	5.0	0.3	3012.4	225.1	0.6	4581.9	49.9	4.9	<0.25	<0.085	72
ET-002	VR-Vent	86.6	6.3	23019	260.7	0.1	0.3	4606.3	314.6	1.1	7722.0	49.7	3.8	<0.25	<0.085	19
ET-003	VR-3	63.2	6.2	23530	261.6	0.1	0.3	4488.2	312.8	1.2	7991.8	49.8	3.9	<0.25	<0.085	nd
ET-005	Ck-5	67.7	4.8	15814	230.4	5.8	0.3	3266.3	201.8	0.7	5013.7	52.4	4.7	<0.25	<0.085	nd
ET-006	Ck-2	65.9	6.7	15220	203.1	5.3	0.3	3059.1	224.7	0.6	4830.5	53.3	4.9	<0.25	<0.085	nd
ET-007	Ck-3	61.5	6.3	15245	213.1	5.4	0.3	3225.8	242.6	0.6	4932.7	53.8	5.2	<0.25	<0.085	nd
ET-008	Ck-4	50.7	6.6	15190	210.9	5.5	0.3	3191.4	239.7	0.6	5011.1	54.7	5.3	<0.25	<0.085	nd
ET-009	La Concha	84.1	6.2	18190	287.3	0.4	0.1	3750.9	233.9	1.4	5831.7	66.2	7.5	<0.25	<0.085	23
ET-011	Piscina Cristalina	50.9	5.3	18065	289.6	1.1	0.1	3884.9	264.3	1.5	5973.5	71.3	6.5	<0.25	<0.085	2
ET-012	El Asesino	85.4	6.4	18069	286.3	0.1	0.0	3770.9	253.1	1.5	5818.3	68.1	6.3	<0.25	<0.085	32
ET-015	El Horno	84.4	6.0	23300	269.9	0.0	0.1	4608.5	333.0	1.6	7544.1	50.9	9.0	<0.25	<0.085	5
ET-016	Linzor Pool	-	-	-	276.8	0.1	0.2	4849.1	369.4	1.2	7872.9	49.9	9.8	<0.25	<0.085	nd
ET-017	El Cobreloa	86.0	5.8	22588	267.1	0.4	0.3	4599.3	344.6	1.2	7549.9	49.2	9.5	<0.25	<0.085	9
ET-020	Piscina Exp. Evap.	56.3	6.0	17730	271.3	3.0	0.2	3753.8	210.6	0.9	5845.6	60.9	6.2	<0.25	<0.085	nd
ET-021	VR-4	55.0	6.3	23387	293.1	0.2	0.3	5059.8	342.9	1.6	8255.6	54.1	10.6	<0.25	<0.085	nd
ET-023	Geiser Corazón	83.7	6.6	12373	157.7	5.8	0.5	2491.3	161.9	0.6	3765.5	46.3	4.1	<0.25	<0.085	117
ET-025	VR-Vent	86.6	7.2	22890	284.0	0.7	nd	3446.0	312	3.6	7798.5	43.8	8.0	<0.1	<0.2	24
ET-026	Ck-Vent	86.6	7.7	14550	182.0	4.2	nd	3203.0	221	1.4	4827.6	43.1	4.9	<0.1	<0.2	68

Table 5: Trace element composition for the hydrothermal fluids in El Tatio, including Ge in µg/L, Ge/Si (µmol/mol) and Al/Si (mmol/mol) ratios. Concentrations are expressed in µg/L and mg/L for high concentrations. '-': unmeasured.

Sample	Ge	Li	B	Al	Mn	Cu	As	Rb	Sr	Zr	Mo	Sb	Cs	Ba	Ge/Si	Al/Si
ID	µg/L	mg/L	mg/L	µg/L	µg/L	µg/L	mg/L	µg/L	mg/L	µg/L	µg/L	mg/L	mg/L	µg/L	µmol/mol	mmol/mol
ET-001	30.2	21.5	100.9	323.9	335.2	23.8	24.8	2.3	3.06	67.4	35.2	1.4	10.0	331	110.98	3.20
ET-002	36.1	35.7	175.6	272	342.3	39.1	41.8	6.2	4.30	112.7	40.1	2.5	15.7	220.8	94.88	1.93
ET-003	25.9	35.5	178.1	396.4	342.3	36.9	42.3	6.3	4.32	113.4	40.3	2.6	16.1	223.9	68.52	2.82
ET-005	23.9	23.8	111.9	376.1	356.1	25.7	26.1	2.4	3.57	60.6	42.3	1.5	11.6	146.4	97.86	4.15
ET-006	23.3	23.1	108.5	305.4	344.5	34.5	26.7	2.4	3.24	62.2	37.4	1.5	10.7	303.5	85.58	3.03
ET-007	23.2	23.3	108.8	568.1	354.4	25.9	26.8	2.4	3.28	62.8	37.4	1.5	10.8	290.2	79.08	5.22
ET-008	22.8	23.8	114.1	274.5	355.3	26.3	26.8	2.5	3.32	67.8	38.1	1.5	10.9	295.2	78.53	2.55
ET-009	24.5	26.0	136.9	341.9	106.8	30.1	31.8	2.5	4.18	75.1	36.9	2.2	12.6	108	86.81	3.26
ET-011	27.3	26.5	142.9	326.1	125.5	33.2	31.1	2.5	4.40	73.5	37.6	2.4	13.3	122.9	85.53	2.75
ET-012	25.2	25.6	134.9	354.4	54.2	38.6	31.7	2.5	4.21	75.8	35.4	2.2	12.5	210.8	82.49	3.12
ET-015	25.9	35.8	169.4	335.9	159.3	41.8	40.9	6.2	4.23	95.2	39.1	2.6	15.9	154.2	64.32	2.25
ET-016	26.5	37.6	175.2	292.3	279.6	41.1	42.9	6.5	4.41	101.4	40.2	2.3	16.4	221.9	59.26	1.76
ET-017	25.2	35.3	167.4	352.5	275.7	39.3	40.6	6.1	4.17	96.4	37.9	2.4	15.4	202	60.53	2.28
ET-020	28.8	26.9	134.5	331.2	204.9	32.2	27.9	2.6	4.21	66.7	43.2	1.8	14.2	69.9	113.29	3.50
ET-021	29.1	38.7	181.0	292.6	357	46.7	44.8	6.7	4.62	105.6	39.4	2.5	17.2	251.1	70.26	1.90
ET-023	18.7	18.7	82.4	183.2	552.2	21.1	21.4	2.5	2.40	51.1	25.1	1.3	8.3	223.3	95.67	2.52
ET-025	-	36.4	174.7	286.6	323.9	38.5	42.1	6.3	4.34	99.9	36.8	2.8	16.1	214.5	-	2.05
ET-026	-	22.4	105.2	276.6	319.3	25	26.0	2.4	3.09	61.8	33.1	1.5	10.4	297.2	-	2.79

Figure 11 compares all geothermal fluids, including the additional samples from Ckoitchi (Ck) and Vega Rinconada (VR), which will be discussed later. Upon examining the silica concentrations (Figure 11a), it is possible to differentiate two groups: a first group with SiO_2 concentrations between 200-250 mg/L, including the samples from Ckoitchi, the thermal pools, together with La Concha and El Asesino geysers. A second group shows SiO_2 concentrations higher than 300 mg/L, and corresponds only to geysers, including Vega Rinconada, El Horno and El Cobresal. In general, no clear trend of silicon concentration with respect to temperature is observed if all samples are considered. Regarding germanium concentrations (Figure 11b), there is no apparent trend with respect to temperature, or hot spring type. However, the highest Ge concentrations correspond to the samples taken at the vents of Vega Rinconada geyser and Ckoitchi perpetual spouter.

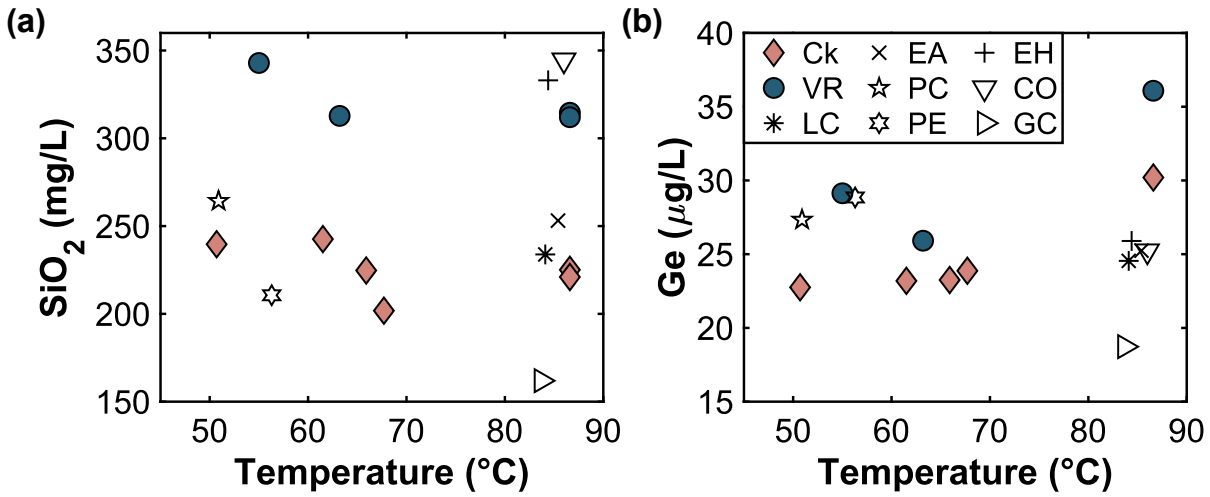

Figure 11: Silica (a) and germanium (b) concentrations of hydrothermal fluids from El Tatio. The pink diamonds represent the Ckoitchi (Ck) samples, the blue circles are the Vega Rinconada (VR) samples. LC: La Concha (asterisk), EA: El Asesino (cross), PC: Piscina Cristalina (star), PE: Piscina Evap. Exp. (hexagram), EH: El Horno (plus sign), CO: El Cobreloa (downward triangle), GC: Geyser Corazon (rightward triangle).

The Ge/Si ratios of the fluids (Figure 12a) range from 59.2 to 113.3 μmol/mol, and no relationship with temperature is observed among the different hot spring types. However, it is possible to observe a positive correlation between Ge/Si and temperature within the fluids sampled at different temperatures from the vents at Ck and VR. This will be further discussed in a following section. In addition, the Al/Si ratios in the fluids (Figure 12b) vary between 1.9 and 5.2 mmol/mol, and no trend is observed with temperature. Notably, the vents of all geysers and the perpetual spouter (Ckoitchi) are concentrated between 1.9 and 3.3 mmol/mol, with an average Al/Si ratio of 2.6 mmol/mol.

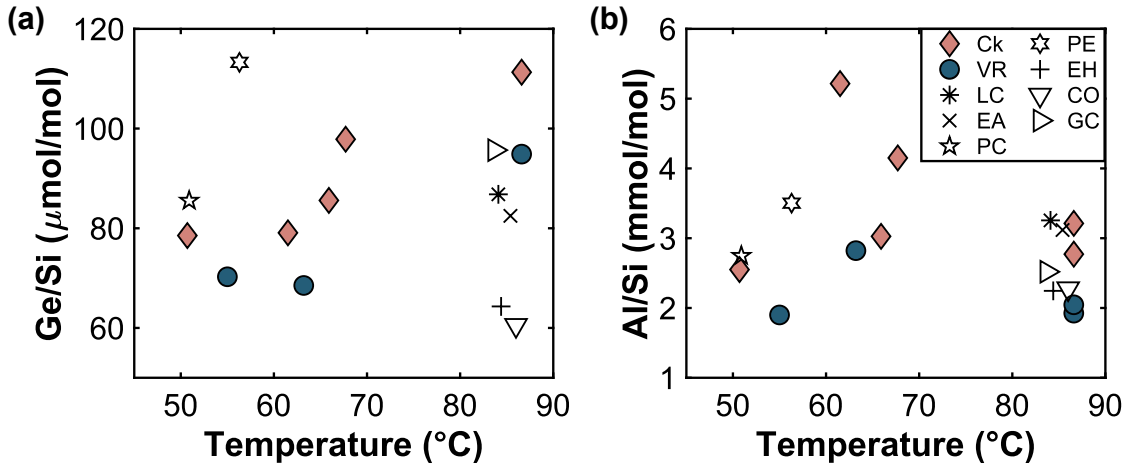

Figure 12: Ge/Si (a) and Al/Si (b) ratios as a function of temperature for El Tatio geothermal fluid samples. The pink diamonds represent the Ckoitchi (Ck) samples, the blue circles are the Vega Rinconada (VR) samples. LC: La Concha (asterisk), EA: El Asesino (cross), PC: Piscina Cristalina (star), PE: Piscina Evap. Exp. (hexagram), EH: El Horno (plus sign), CO: El Cobreloa (downward triangle), GC: Geyser Corazon (rightward triangle).

Temperatures for the Ckoitchi sampling points vary between 50.7°C and 86.6°C. The sampled fluid temperatures at Vega Rinconada are between 55° and 86.6°C. The temperatures of these points will be used to characterize both fluid and sinter samples. Silica concentrations for the Ckoitchi downstream sampling points range between 201.8 and 242.6 mg/L; while the downstream sampling points at Vega Rinconada range between 312 and 342.9 mg/L (Figure 13a). Chloride concentrations are also higher in Vega Rinconada, ranging between 7722-8255.6 mg/L, while Ckoitchi has values between 4827.6 and 5012.7 mg/L (Figure 13c). Both silica (Figure 13a) and chloride (Figure 13b) concentrations do not follow a noticeable trend with temperature. The behavior of germanium concentration with respect to temperature (Figure 13b) does not seem to follow a clear trend either. Ge concentrations at Ckoitchi vary between 22.8 and 30.2 µg/L, and those of Vega Rinconada between 25.9 and 36.1 µg/L, with higher values on average in the VR sector (30.4 µg/L, versus 24.5 µg/L in Ckoitchi). Both vents present higher concentrations than the lower temperature points. Aluminum concentrations (Figure 13d) show no trend with temperature.

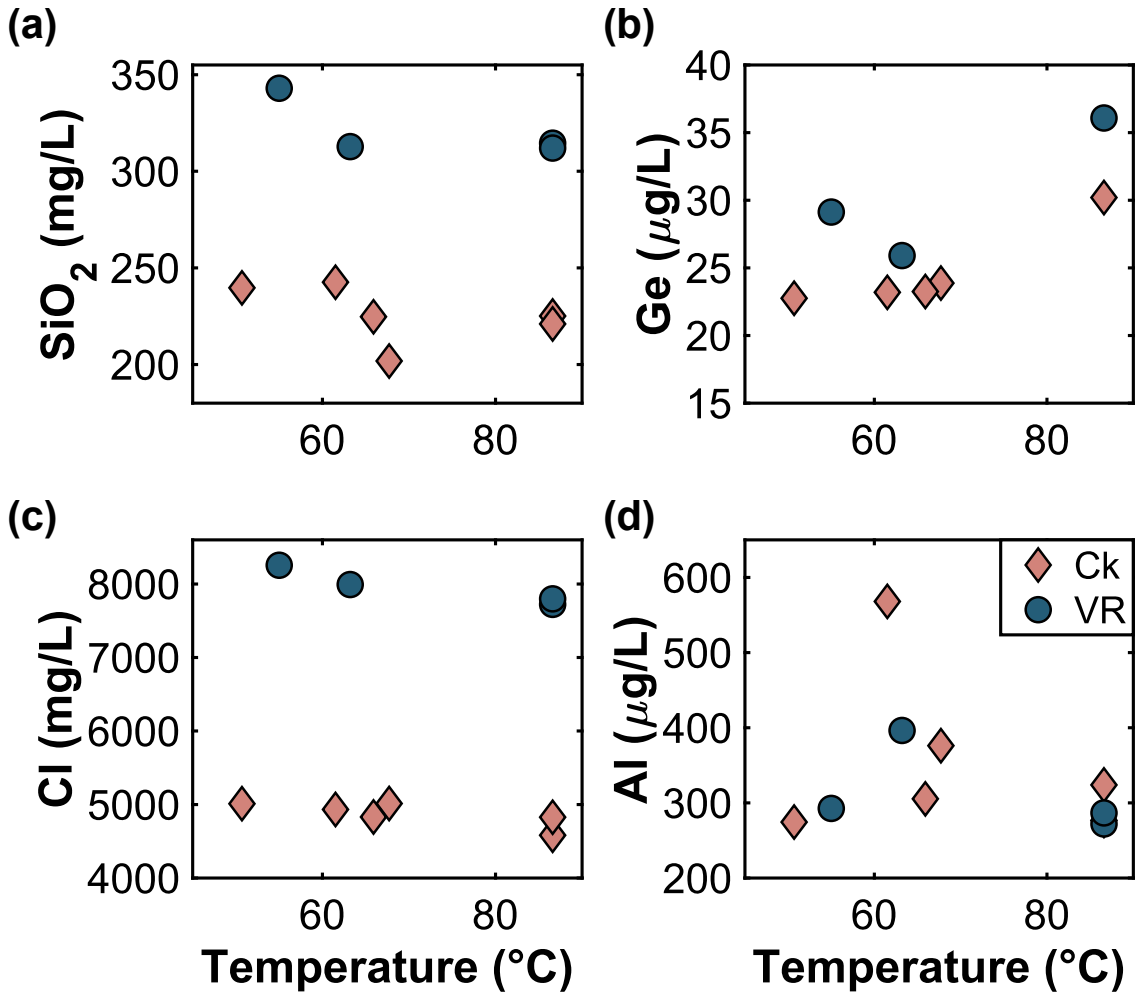

Figure 13: Major (a and c) and trace (b and d) element concentrations as a function of in-situ temperature for the Ckoitchi (Ck, pink diamonds) and Vega Rinconada (VR, blue circles) fluids.

Upon closer look at the Ge/Si ratios at the Ckoitchi and Vega Rinconada sampling points (Table 5), it can be observed that at VR, the Ge/Si ratios range from 68.5 to 94.9 µmol/mol, and the Ck ratios range from 78.5 to 111 µmol/mol. The average ratio at Vega Rinconada is 77.9 µmol/mol, while in Ck, it is higher at 90.4 µmol/mol. This difference is attributed to the varying

silica concentrations between the two zones (Figure 13a). Ge/Si ratios as a function of fluid temperature, in both VR and Ck, (Figure 14a) show an increase with temperature, upon proximity to the vent.

The Al/Si ratio ranges from 2.6 to 5.2 mmol/mol in Ckoitchi, while in Vega Rinconada, the range is between 1.9 and 2.8 mmol/mol (Figure 14b). It is worth noting that Ck has a higher average Al/Si ratio of 3.5 mmol/mol compared to VR, with 2.2 mmol/mol.

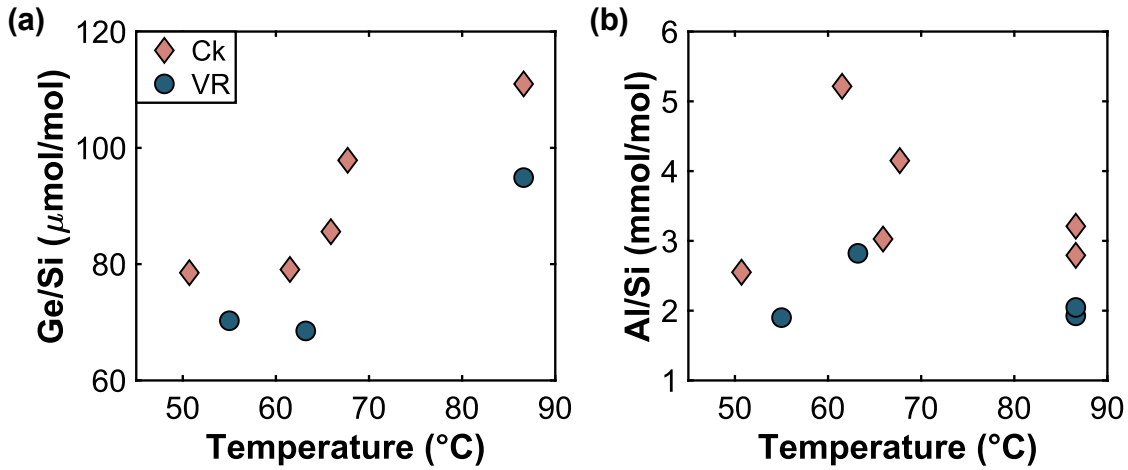

Figure 14: Fluid Ge/Si (A) and Al/Si (B) ratios as a function of temperature in-situ for Ckoitchi (Ck, pink diamonds) and Vega Rinconada (VR, blue circles).

3.3. Fluid evaporation experiments

The remaining volumes from the evaporation experiments were analyzed to determine the behavior of Ge and Al as a function of early silica precipitation and/or polymerization. Table 6 shows the remaining volumes (mL) and the dates of their implementation and extraction. The total evaporated volume across the seven days of the evaporation experiments ranges from 40 to 205 mL. The average evaporation rate is 33 mL/day with variations for each graduated cylinder throughout the experiment. The daily variations probably result from re-arrangement of the cylinders in the geyser pool during the experiment, which resulted in different heat fluxes from the bottom hot pool where they were submerged. The evaporation rates decreased from 40 to 26.7 mL/day over the first three sample extractions. On September 29th, the maximum evaporation rate of 45 mL/day was recorded, followed by a decrease to 24 mL/day on the following day, which marked the minimum evaporation rate among the samples. The evaporation rates then ranged between 28.3 and 34.2 mL/day in the samples taken on the last day, October 1st.

Table 6: Evaporation experiments with their respective sampling dates, evaporated volumes, and resulting evaporation rates. Evaporated volumes are expressed in mL, while evaporation rates are in mL/day.

Sample ID	Date of Implementation	Date of extraction	Duration of the experiment	Evaporated Volume	Evaporation Rate
			hours	mL	mL/day
ET-004 VR-EVAP-01	25-sept	26-sept	17.03	40	40
ET-010 VR-EVAP-02	25-sept	27-sept	40.28	60	30
ET-013 VR-EVAP-07	25-sept	28-sept	64.28	80	26.7
ET-014 VR-EVAP-04	25-sept	29-sept	91.20	180	45
ET-018 VR-EVAP-03	25-sept	30-sept	112.03	120	24
ET-022 VR-EVAP-05	25-sept	01-oct	137.78	205	34.2
ET-024 VR-EVAP-06	25-sept	01-oct	137.78	170	28.3

Table 7 and Table 8 show the elemental concentration of the remaining fluids from evaporation experiments. The remaining evaporated fluids at VR have a high specific conductivity, averaging 23412 µS/cm. They also have high concentrations of sodium and chloride, with concentrations of 5077.9 mg/L and 8198.4 mg/L, respectively. In general, most elements in the fluid exhibit conservative behavior, increasing in concentration as the fluid evaporates and loses volume. However, silica and calcium do not follow this pattern. Ca concentrations remain constant at 290.8 mg/L, indicating the possible presence of an external buffer. This may indicate the formation of complex compounds that regulate the calcium level in the solution, external influences, or a variety of chemical reactions. Furthermore, adsorption and desorption processes could represent another distinct mechanism potentially influencing the observed phenomena.

Table 7: Fluid composition of the evaporation experiments. The table includes in-situ physicochemical parameters (T°, pH, specific conductivity (SpC)) and major ions composition. Temperatures are in °C, SpC in µS/cm. Concentrations are expressed in mg/L.'nd': no detected.

Sample ID	T	pH	SpC	Ca	Mg	Mn	Na	SiO_2	F^-	Cl^-	SO_4^{2-}	Br^-	NO_3^-	PO_4^{-3}	HCO_3^-
	°C		µS/cm	mg/L	mg/L	mg/L	mg/L	mg/L	mg/L	mg/L	mg/L	mg/L	mg/L	mg/L	mg/L
ET-004 VR-EVAP-01	-	5.6	22061	282.0	0.1	0.3	4934.1	343.1	1.15	7796.3	49.8	3.7	<0.25	<0.085	nd
ET-010 VR-EVAP-02	34.5	6.4	22804	276.1	0.2	0.3	4823.8	329.2	1.07	7634.3	52.7	3.6	<0.25	<0.085	nd
ET-013 VR-EVAP-07	30	7.0	23049	283.8	0.2	0.3	5007.5	330.7	1.54	8141.2	54.6	9.8	<0.25	<0.085	nd
ET-014 VR-EVAP-04	31	6.7	23993	290.2	0.2	0.3	5106.1	303.2	1.62	8444.9	57.9	10.7	<0.25	<0.085	nd
ET-018 VR-EVAP-03	30	6.9	23383	292.0	0.2	0.3	5147.0	315.5	1.57	8303.6	54.5	10.3	<0.25	<0.085	nd
ET-022 VR-EVAP-05	25.4	6.9	24413	306.8	0.2	0.3	5294.6	336.9	1.66	8621.3	54.8	11.0	<0.25	<0.085	nd
ET-024 VR-EVAP-06	25.4	6.8	24181	305.0	0.2	0.3	5232.4	332.6	1.56	8447.3	56.2	10.6	<0.25	<0.085	nd

Table 8: Trace element composition for the evaporation experiment samples, including Ge in µg/L, Ge/Si (µmol/mol) and Al/Si (mmol/mol) ratios. Concentrations are expressed in µg/L and mg/L for high concentrations.

Sample ID	Ge	Li	B	Al	Mn	Cu	As	Rb	Sr	Zr	Mo	Sb	Cs	Ba	Ge/Si	Al/Si
	µg/L	mg/L	mg/L	µg/L	µg/L	µg/L	mg/L	mg/L	mg/L	µg/L	µg/L	mg/L	mg/L	µg/L	µmol/mol	mmol/mol
ET-004 VR-EVAP-01	29.8	35.6	177.6	255.1	341.9	37.6	42.3	6.2	4.3	112.0	40.0	2.7	15.9	214.5	71.87	1.66
ET-010 VR-EVAP-02	28.8	37.9	177.2	626.8	342.2	40.5	43.8	6.5	4.5	101.6	38.9	2.7	16.7	212.8	72.29	4.24
ET-013 VR-EVAP-07	29.0	38.6	180.9	364.7	355.0	42.5	44.7	6.6	4.6	106.7	39.5	2.6	16.9	246.9	72.49	2.46
ET-014 VR-EVAP-04	29.8	40.4	189.4	314.6	361.4	45.3	46.8	6.9	4.8	110.6	41.6	2.8	17.9	238.3	81.42	2.31
ET-018 VR-EVAP-03	29.1	39.2	188.0	307.7	354.3	43.3	46.1	6.8	4.7	112.3	41.2	2.8	17.6	216.2	76.30	2.17
ET-022 VR-EVAP-05	32.3	40.7	191.0	276.7	365.2	44.2	47.4	7.0	4.8	114.5	41.5	2.9	18.1	229.4	79.18	1.83
ET-024 VR-EVAP-06	31.7	40.3	192.3	216.2	365.2	47.9	47.3	7.0	4.8	114.9	41.4	2.9	18.1	234.3	78.91	1.45

Silica concentrations in the evaporation experiments ranged from 303.2 to 343.1 mg/L, with an average of 327.3 mg/L. The data presented in Figure 15a illustrates the trend of silica concentrations in relation to the evaporated volume, revealing a general decrease in silica concentration as the evaporated volume increases. An exception to this trend is observed in the samples from October 1st, which show a higher concentration. A possible explanation for the elevated Si concentration in these samples is the adjustment in the placement of the cylinders in the pool, as they were moved closer to vent when the rest of them had been retired. This proximity likely resulted in a higher fluid temperature during eruptions, which, in turn, increased the solubility of silica. Chloride (Figure 15c) exhibits a conservative behavior, increasing in concentration as fluid is lost through evaporation. Considering the concentrations of Ge and Al, due to their similarities to Si, one might expect similar behaviors. Yet, examining Ge concentrations (Figure 15b) reveals an almost conservative trend, increasing slightly upon volume change. For Al (Figure 15d), analyzing the evaporated volume does not show a clear pattern.

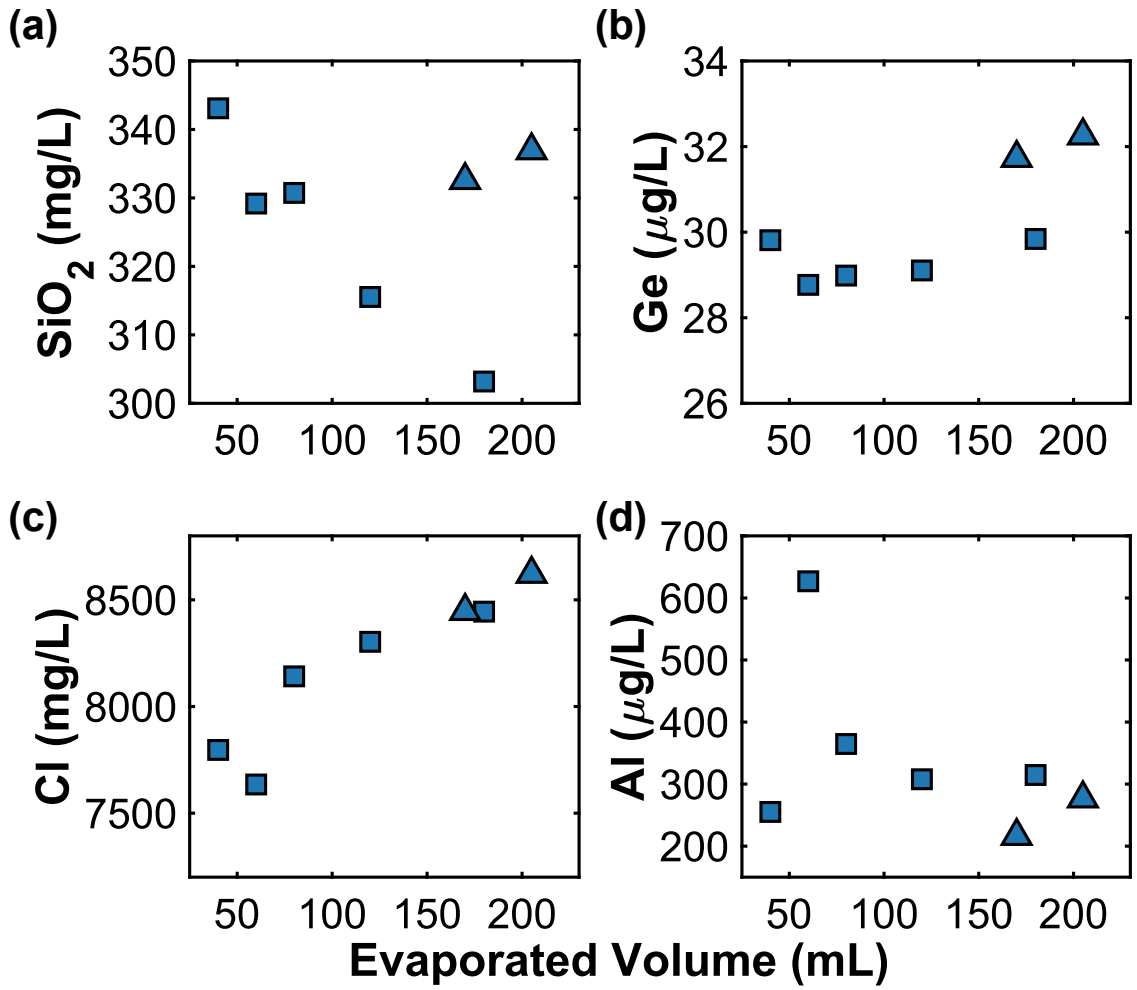

Figure 15: Silica(a), germanium (b), chloride (c) and aluminum (d) concentrations of the remaining fluid as a function of the evaporated volume in the evaporation experiment. Each blue square represents a sample, while the blue triangles represent the samples extracted on the last day (October 1st).

Concentrations of SiO_2, Cl^-, Ge, and Al as a function of average evaporation rates show that: 1) silica concentrations (Figure 16a) increase with higher evaporation rates (with exception of the sample collected on Sept. 29th); 2) no correlation between chloride, Ge or Al concentrations and evaporation rates is observed (Figure 16b, c and d).

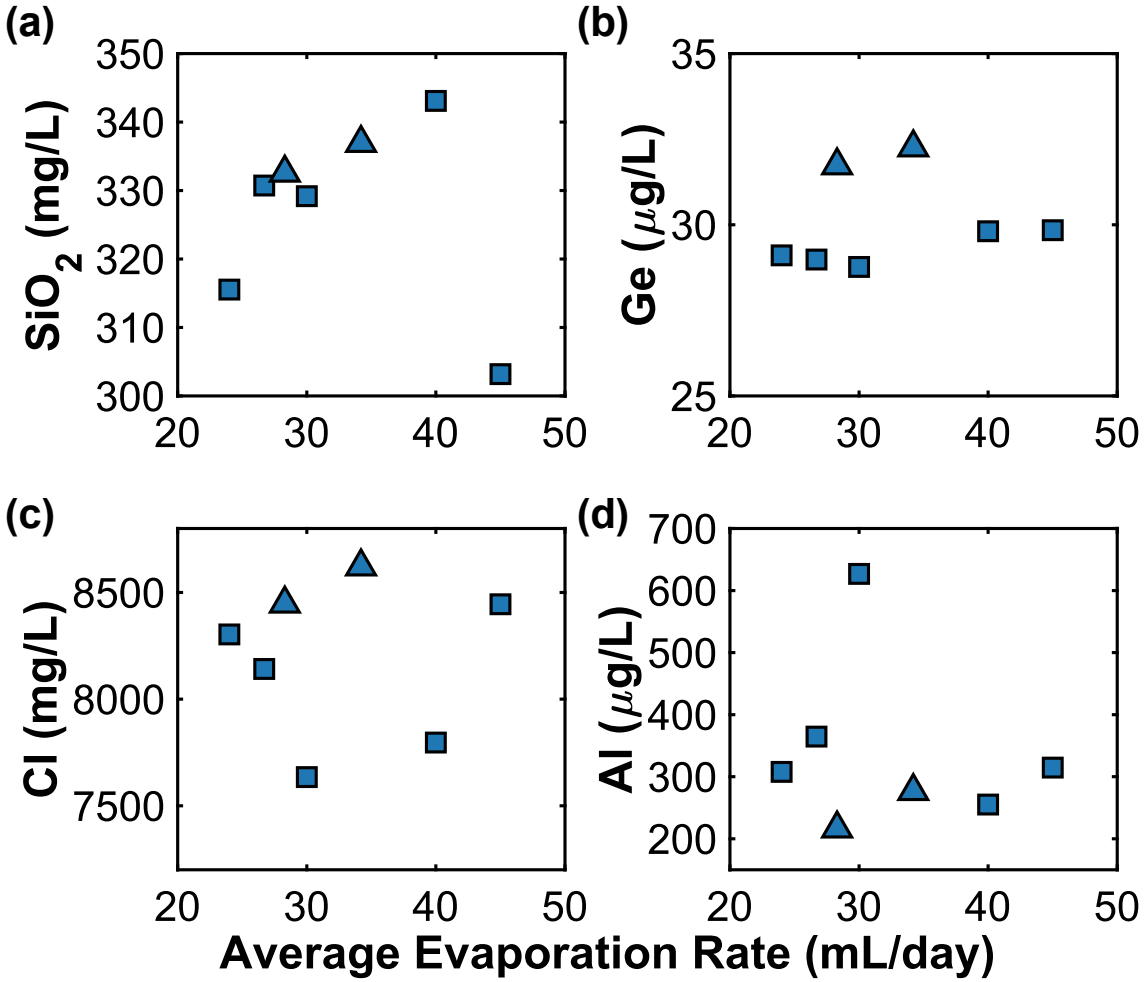

Figure 16: Silica (a), germanium (b), chloride (c) and aluminum (d) concentrations of the remaining fluid as a function of the Average Evaporation Rate (mL/day) in the evaporation experiment. Each blue square represents a sample, while the blue triangles represent the samples extracted on the last day (October 1st).

Ge/Si ratios in the evaporation experiment samples ranged from 71.9 to 81.4 μmol/mol, with an average of 76.1 μmol/mol. Al/Si ratios ranged from 1.45 to 4.24 mmol/mol, with an average Al/Si ratio of 2.3 mmol/mol. Ge/Si ratios increase with evaporated volume (Figure 17a), while the Al/Si ratios (Figure 17b), as well as the Al concentrations, do not follow a trend with respect to the evaporated volume.

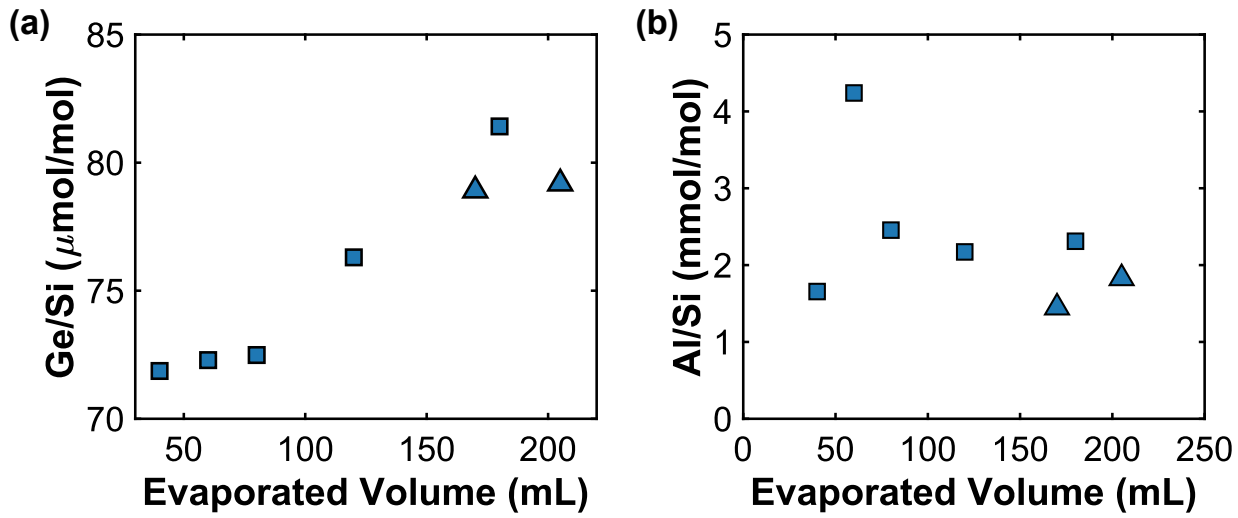

Figure 17: Ge/Si (A) and Al/Si (B) ratios as a function of the evaporated volume in the evaporation experiment. Each blue square represents a sample, while the triangles represent the samples extracted on the last day (October 1st).

Finally, when examining the Ge/Si ratios in relation to average evaporation rates (Figure 18a), two distinct trends emerge for two sample groups. Samples with a ratio higher than 75 µmol/mol show an increase with rising evaporation rates, whereas those with a ratio lower than 73 µmol/mol exhibit a slight decrease as the evaporation rate increases. For the Al/Si ratios, there are no conclusive results regarding the relationship with the average evaporation rate (Figure 18b).

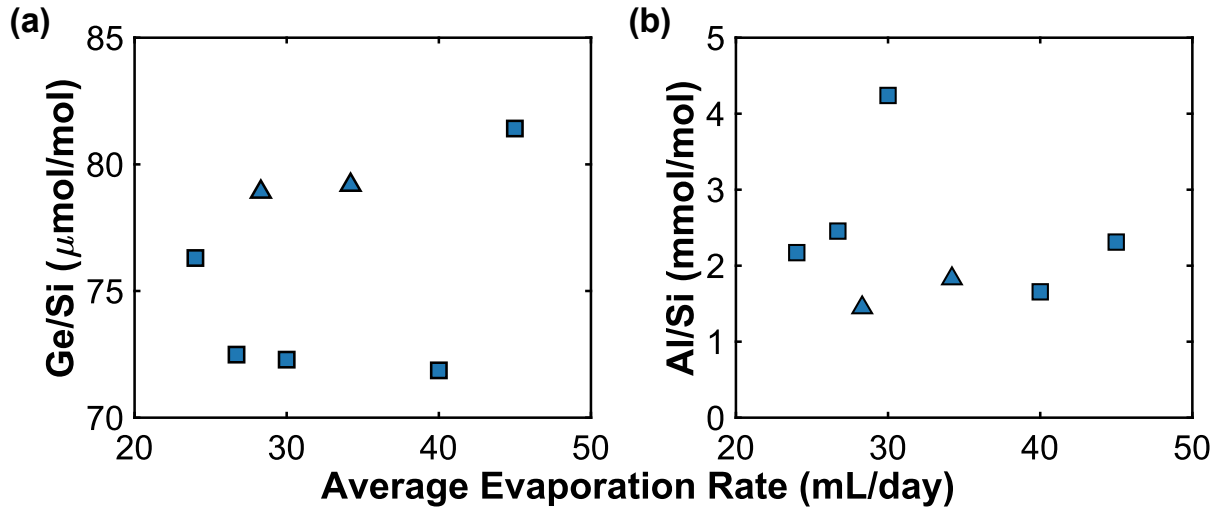

Figure 18: Ge/Si (A) and Al/Si (B) ratios as a function of the Average Evaporation Rate (mL/day) in the evaporation experiment. Each blue square represents a sample, while the triangles represent the samples extracted on the last day (October 1st).

3.4. Opal precipitation experiments

3.4.1. Bulk precipitation rates

The in-situ silica precipitation experiments at El Tatio resulted in 38 slides with precipitated material, out of which 26 were considered for calculation of precipitation rates. Nine of the discarded slides correspond to those covered with sandpaper, which failed to increase the adhesion surface for opal precipitation (some had almost no precipitated material), the remaining three slides were discarded due to low efficiency of precipitation or a significant deviation from values obtained from other slides at the same point, resulting from being submerged in the hydrothermal fluid, high accumulation of biologic material, and indirect interruption of waterflow. Measured effective precipitated area, duration of the experiment, bulk precipitated weights, precipitation rates, and observations about each sample are presented in Table 9 for the Ckoitchi samples, and Table 10 for the Vega Rinconada samples.

Table 9: Information obtained from the precipitation experiment conducted at Ckoitchi. The positions of the slides are those in which they were found at the end of the experiment. A_{Ep}= Effectively precipitated area. H=horizontal position, V= vertical position, Subh= subhorizontal position. *= slide used for geochemical analysis.

Sample site	Sample ID	Site T	Time	A_{Ep}	Bulk Precipitate	Bulk silica precipitation rate	Adjusted silica precipitation rate	Position of the slide	Observations
		°C	days	mm^2	g	$kg/year/m^2$	$kg/year/m^2$		
Ck-V	3	86.6	210	1935.48	0.805	0.723	0.405	V	
Ck-V	4*	86.6	210	1935.48	0.491	0.441	0.247	V	
Ck-1	04L	85.3	210	1935.48	1.531	-	-	V	Sample discarded for precipitation rate calculation.
Ck-1	7	85.3	210	1935.48	1.196	1.074	0.601	V	
Ck-1	8	85.3	210	1841.23	1.985	1.874	1.049	V	
Ck-1	39*	85.3	203	1859.78	1.262	1.220	0.683	V	
Ck-2	07L	65.9	210	1935.48	1.283	-	-	H	Sample discarded. Less bulk precipitate than the site average.
Ck-2	40	65.9	203	925.68	2.985	5.798	5.450	V	
Ck-2	10	65.9	210	805.25	2.424	5.233	4.919	V	
Ck-2	6*	65.9	210	1921.48	0.555	-	-	Subh	It was subhorizontal, which is why it precipitated less material. Sample discarded for precipitation rate calculation.
Ck-3	09L	61.5	210	1935.48	1.308	-	-	V	Sample discarded. Less bulk precipitate than the site average.
Ck-3	41	61.5	203	1310.62	2.419	3.318	3.053	V	
Ck-3	12*	61.5	210	1273.78	2.463	3.361	3.092	V	
Ck-3	13	61.5	210	1104.77	2.616	4.115	3.786	Subh	
Ck-4	06L	50.7	210	1935.48	0.436	-	-	V	Sample discarded. Less bulk precipitate than the site average.
Ck-4	43*	50.7	203	1143.12	2.441	3.840	3.264	V	
Ck-4	15	50.7	210	1040.24	2.625	4.387	3.729	V	
Ck-4	16	50.7	210	969.24	2.935	5.264	4.474	Subh	
Ck-5	08L	67.7	210	1935.48	-0.043	-	-	V	It has noticeable precipitate (visually), but when balancing it is lost, part of the sandpaper may have been lost. Sample discarded for precipitation rate calculation
Ck-5	17	67.7	210	1276.70	1.849	2.517	1.862	V	
Ck-5	42*	67.7	210	1935.48	0.321	-	-	V	The slide was submerged in the pool. Less bulk precipitate than the site average. Sample discarded.
Ck-5	19	67.7	210	1607.40	1.392	1.505	1.114	Subh	

Table 10: Information obtained from the precipitation experiment conducted at Vega Rinconada. The positions of the slides are those in which they were found at the end of the experiment. A_{Ep}= Effectively precipitated area. H=horizontal position, V= vertical position, Subh= subhorizontal position. *= slide used for geochemical analysis.

Sample site	Sample ID	Site T	Time	A_{Ep}	Bulk Precipitate	Bulk silica precipitation rate	Adjusted silica precipitation rate	Position of the slide	Observations
		°C	days	mm^2	g	$kg/year/m^2$	$kg/year/m^2$		
VR-1	12L	86.6	209	1935.48	-0.175	-	-	H	It has precipitate (visually), but in the balance, it is lost. Sample discarded for precipitation rate calculation
VR-1	21	86.6	209	1603.92	0.997	1.086	1.043	H	
VR-1	23	86.6	209	1307.69	1.590	2.123	2.038	H	Suspended in mid-air, it could cool the fluid faster and precipitate more.
VR-1	24	86.6	209	1703.88	0.731	0.749	0.719	H	
VR-2	15L	74.4	209	1935.48	0.560	-	-	V	Sample discarded. There is less bulk precipitate than the site average.
VR-2	28	74.4	209	1283.58	1.344	1.828	1.828	V	
VR-2	29	74.4	209	1362.64	1.441	1.847	1.847	V	
VR-2	30	74.4	209	938.09	2.690	-	-	V	It remained behind the sandpaper-covered slide without receiving the splash of water.
VR-3	13L	63.2	209	1935.48	2.032	-	-	H	Although it has precipitated material, it does not reach the precipitation values for this point concerning the other slides. Sample discarded for precipitation rate calculation.
VR-3	26	63.2	209	1549.39	2.727	3.074	3.074	H	
VR-3	27*	63.2	209	1550.66	3.390	3.818	3.818	H	
VR-3	37	63.2	209	1614.53	2.084	2.254	2.254	H	Less water reached it directly
VR-4	11L	55	205	840.62	4.549	-	-	V	It presents a greater precipitate because the area was better constrained for the glass slide. Sample discarded for precipitation rate calculation.
VR-4	33	55	205	879.27	2.792	5.655	5.655	V	It precipitated in a smaller area compared to the other uncoated slides.
VR-4	34	55	205	1098.32	2.385	3.867	3.867	V	
VR-4	38*	55	205	1231.36	2.003	2.896	2.896	V	

At the Ckoitchi sites, the bulk precipitate ranged from 0.49 to 2.99 g for the samples that were not discarded, while at Vega Rinconada the range was 0.73 to 3.39 g. The mean amount of bulk precipitate was higher in Vega Rinconada compared to Ckoitchi.

The bulk silica precipitation rates for Ckoitchi vary between 0.44 and 5.8 kg/year/m^2, while for Vega Rinconada, between 0.75 and 5.65 kg/year/m^2. By averaging the bulk precipitation rates at each point, the maximum precipitation rates at Ckoitchi were recorded at 65.9°C with an average of 5.5 kg/year/m^2 and at 1.6 m from the vent. Regarding Vega Rinconada, the highest average rate was 4.1 kg/year/m^2 at a fluid temperature of 55°C, which occurred at 4.2 m from the vent. There are no significant differences between the values obtained in Ckoitchi and Vega Rinconada. When all sites are considered together, along with the resulting slides (Figure 19), it is evident that precipitation rates as a function of temperature are higher at lower temperatures (between 50-65°C), and there is a steady increase in rate downstream of the vents (86.6°C). Thus, at both VR and Ck sites, the silica precipitation rates increase with the cooling of the fluid as it flows away from the vent. Although the VR site has fewer control positions, this tendency remains, showing the lowest silica precipitation rate at the vent despite the higher spread across the different experiments. At vent temperatures around 86.6ºC, the silica precipitation rate at Vega Rinconada is higher than at Ckoitchi. The estimation of the precipitated areas by photographic analysis could be one of the main sources of error in the precipitation rates obtained; however, despite this adjustment, the results are quite consistent with each other, especially considering that each of the slides was analyzed separately so that an overestimation or underestimation of the areas would change only the point of highest precipitation.

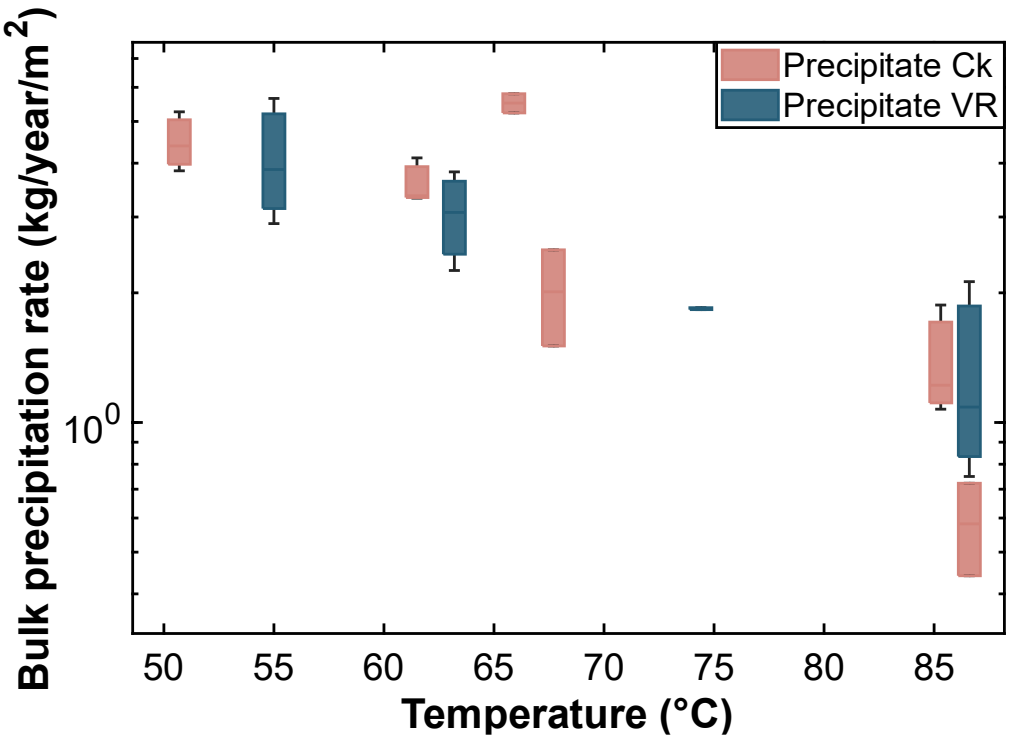

Figure 19: Bulk silica precipitation rate (kg/year/m^2) in the glass slides as a function of temperature (°C) for each site at Ckoitchi (Ck, pink bar) and Vega Rinconada (VR, blue bar).

Given the presence of biological material especially evident in Ckoitchi to the naked eye, for greater accuracy, the precipitation rate should consider only the opal content of the sample. This correction implies multiplying the bulk SiO_2 concentrations obtained from the alkaline extractions. However, due to some inconsistencies that will be detailed in subsection 3.5, for this case, only the results from the January 2022 alkaline extractions were considered as correction factors. Therefore, the rates that showed a greater change when adjusting the ratio with the silica content were those of the Ckoitchi sector, due to their higher organic material content (Figure 20). In the case of Ckoitchi, after adjusting the precipitation rates, the values decreased from a range of 0.44-5.8 kg/year/m^2 to 0.25-5.45 kg/year/m^2 (Table 9), with an average of 2.5 kg/year/m^2. For Vega Rinconada, the results were adjusted from a range of 0.75-5.65 kg/year/m^2 to a range between 0.72-5.65 kg/year/m^2. Therfore, no significant adjustent resulted from the bulk SiO_2 correction in the VR samples (Table 10).

Comparing Figure 19 and Figure 20 reveals two main changes in the samples: a narrowing in the ranges of Ckoitchi rates in Figure 20 and a greater difference in the precipitation rates of the vents, with Ckoitchi rates dropping even lower after adjustment. Although this adjustment improves the accuracy of the calculation of precipitation rates when comparing these two different zones, in the following sections, the bulk precipitation rate will be used in the comparisons to avoid confusion with the SiO_2 correction that was ineffective for some batches of the alkaline extractions. These will be discussed later on.

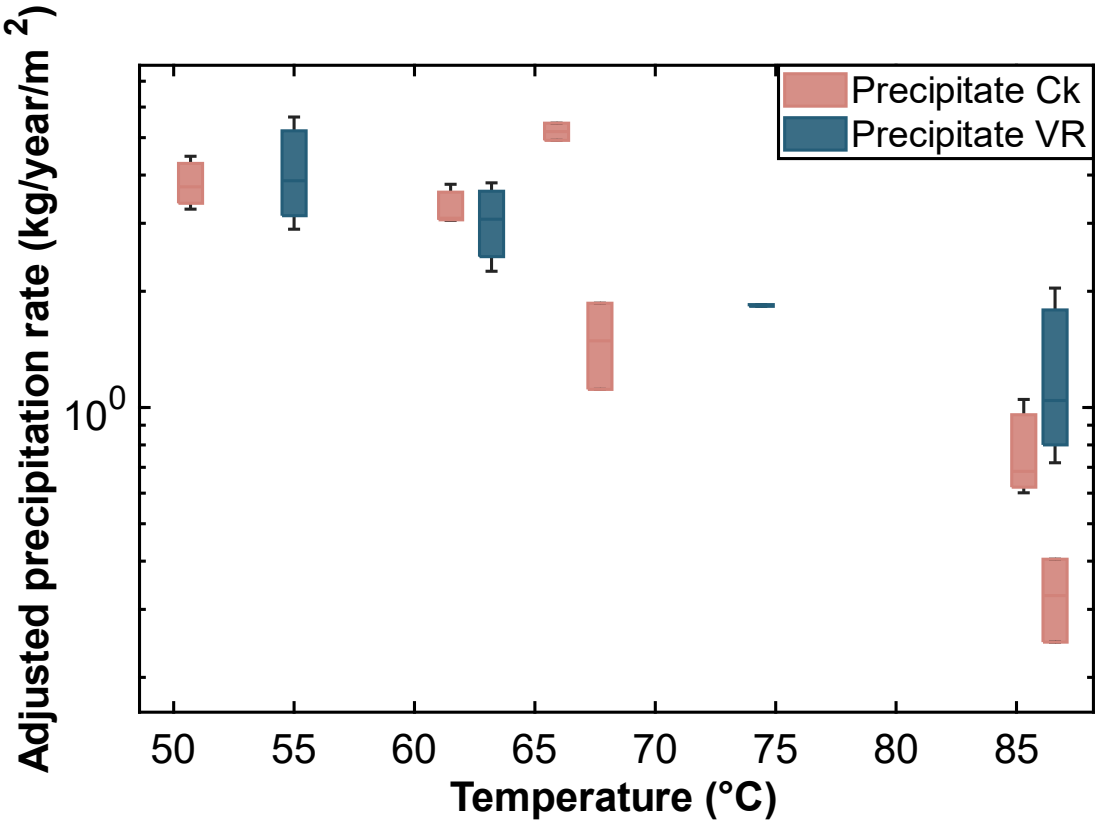

Figure 20: Adjusted silica precipitation rate (kg/year/m^2) in the glass slides as a function of temperature (°C) for each site at Ckoitchi (Ck, pink bar) and Vega Rinconada (VR, blue bar). The weighting factors (opal SiO_2 measurements) for the bulk precipitation rate used to obtain the adjusted rate were: 56% for Ck-V and Ck-1, 94% for Ck-2, Ck-3=92%, Ck-4= 85%, Ck-5= 74%, VR-1= 96% and for VR-2, VR-3 and VR-4=100%.

3.4.2. Ge partitioning in opal precipitates

For conducting the geochemical analyses of the precipitates, only one sample from each sampling point was selected, based on the premise that precipitates originating from the same location share an identical composition. These selected samples are highlighted with an asterisk (*) in Tables 9 and 10. It is worth mentioning that in the Vega Rinconada sector, it was only possible to collect precipitate samples for geochemical analysis from the two areas farthest from the vent (VR-3 and VR-4). This limitation arose because the samples from VR-1 and VR-2 had very thin precipitate layers that could not be manually separated without removing the glass slide. However, these samples were analyzed using SEM, as previously shown in Figure 9C and D.

For the selected slides for geochemisty at each point (Table 11), bulk precipitation rates at Ckoitchi vary between 0.29-3.84 kg/year/m^2, while for Vega Rinconada, the samples have a bulk precipitation rate of 2.89 and 3.82 kg/year/m^2. The precipitation rates from the slides Co02-06 and Co05-42 (equal to 0.502 kg/year/m^2 and 0.288 kg/year/m^2 respectively) (Table 11), were discarded for computing the average precipitation rates at each location due to the low precipitation yield compared to the rest of slides in points in Ck-2 and at Ck-5 (Table 9). However, their individual bulk precipitation rates will be used when examining the geochemistry results at each point, same as the rest of the samples. The silica content of the samples ranges from 28 wt.% to 64 wt.% of SiO_2 for Ckoitchi, and 66-77 wt.% of SiO_2 for the Vega Rinconada samples. For Ckoitchi these values are too low considering that the alkaline extraction procedure removes any organic material that might contribute to the low yield. Considering the SEM analysis of an in-situ sinter sample at the same point revealed approximately 79 wt.% of SiO_2 (Figure10C), and thus, it appears that these low concentrations are related to low yield of the extraction procedure in some cases, which we will discuss later. Germanium concentrations in the precipitates range from 7.2 to 43.8 ppm at Ckoitchi with an average of 19.7 ppm, while precipitates measured from Vega Rinconada average 4.3 ppm of Ge. The Ck samples have a higher Ge concentrations than the VR samples.

Table 11: Silica precipitation rates and geochemistry of the silica precipitation experiments. The table lists sampling temperature, silica precipitation rates, SiO_2, Ge (ppt) and Ge/Si.

Sample site	Measured Sample ID	T	Bulk silica precipitation rate	Adjusted silica precipitation rate	SiO_2	Ge	Ge/Si
		°C	kg/year/m^2	kg/year/m^2	wt.%	ppm	µmol/mol
Ck-V	CoVent-04	86.6	0.441	0.247	28%	20.023	59.06
Ck-1	Co01-39	85.3	1.220	0.683	33%	18.397	45.57
Ck-2	Co02-06	65.9	0.502	0.472	45%	43.833	81.02
Ck-3	Co03-12	61.5	3.361	3.092	57%	16.006	23.37
Ck-4	Co04-43	50.7	3.840	3.264	64%	7.221	9.35
Ck-5	Co05-42	67.7	0.288	0.213	36%	12.551	29.11
VR-3	VR03-27	63.2	3.818	3.818	77%	2.379	2.55
VR-4	VR04-38	55	2.896	2.896	66%	6.133	7.71

Examining silica concentrations with respect to temperature (Figure 21a) and bulk precipitation rates (Figure 21b) reveals that the highest silica concentrations are found at lower temperatures and higher precipitation rates, corresponding to points farthest from the vent.

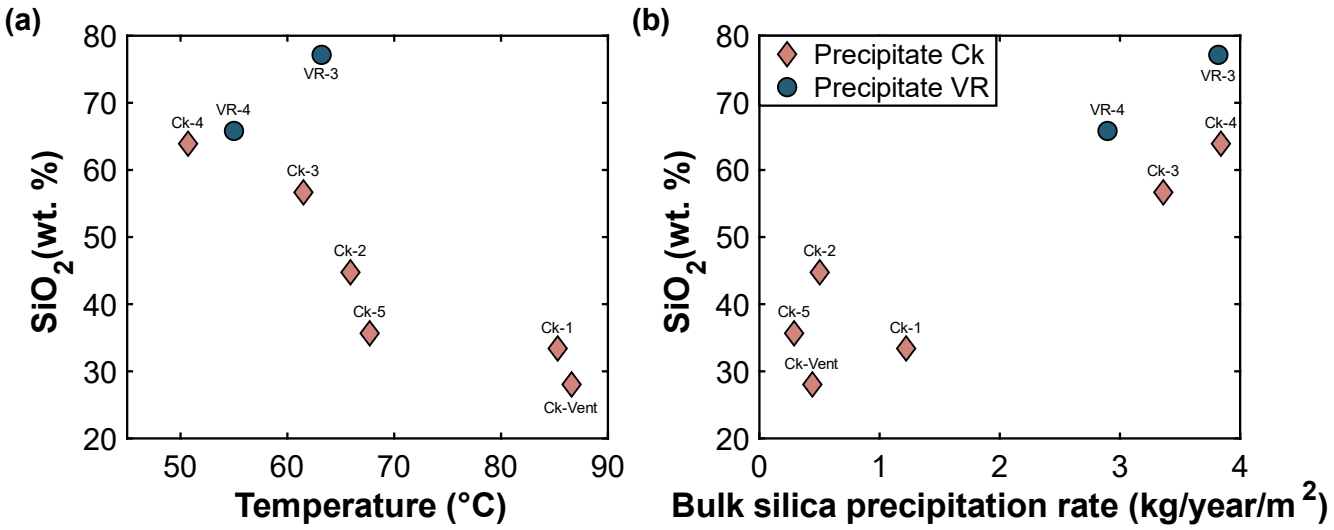

Figure 21: Silica concentrations as a function of temperature (a) and bulk precipitation rates (b) for samples from the Ckoitchi (pink diamonds) and Vega Rinconada (blue circles) precipitation experiments. Each point is associated with their respective position in the experiment, denoted as Ck-X or VR-X.

Germanium concentrations as a function of temperature (Figure 22a) and bulk precipitation rates (Figure 22b) generally show a slight increase in concentration with temperature (with exception of the Ck-2 point sample Co02-06), and thus, they increase with lower precipitation rates. Overall, the samples closer to the vent have slightly higher Ge concentrations, contrary to silica.

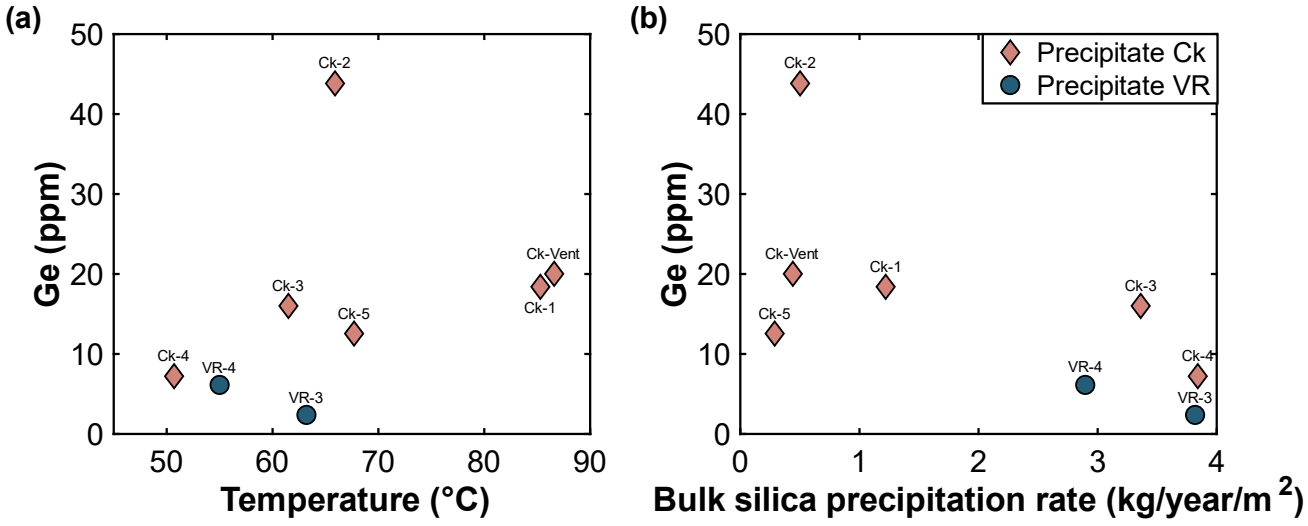

Figure 22: Germanium concentrations as a function of temperature (a) and bulk precipitation rates (b) for samples from the Ckoitchi (pink diamonds) and Vega Rinconada (blue circles) precipitation experiments. Each point is associated with its respective position in the experiment, denoted as Ck-X or VR-X.

Despite the potential difficulties in the alkaline extractions that could impact total concentrations of major and trace element constituents in the precipitates, we assume dissolution of the opal is stoichiometric, and thus, elemental ratios are preserved, particularly for Ge/Si (Kurtz et al.,

2002). Ge/Si results in the precipitation experiments range between 9.35 and 81.02 µmol/mol at Ck and 2.55 and 7.71 µmol/mol at VR (Figure 23A, same values as Table 9). The Ge/Si ratios decrease as a function of temperature at the Ckoitchi site, and consequently, they follow an inverse trend with respect to silica precipitation rates (Figure 23B), i.e., the Ge/Si ratio decreases downstream from the vent. The Co02-06 slide from the Ckoitchi site shows an anomalously high value of Ge/Si (81.02 µmol/mol) that escapes from the trend when compared to the rest of the samples as a function of temperature. It is possible that this anomalous result is derived from the significant amount of organic material deposited on the slide. The Co02-06 slide was positioned subhorizontally and was almost entirely covered by bacterial mat. The two VR samples exhibit an opposite behavior with temperature, but they still follow the general inverse trend with respect to precipitation rates.

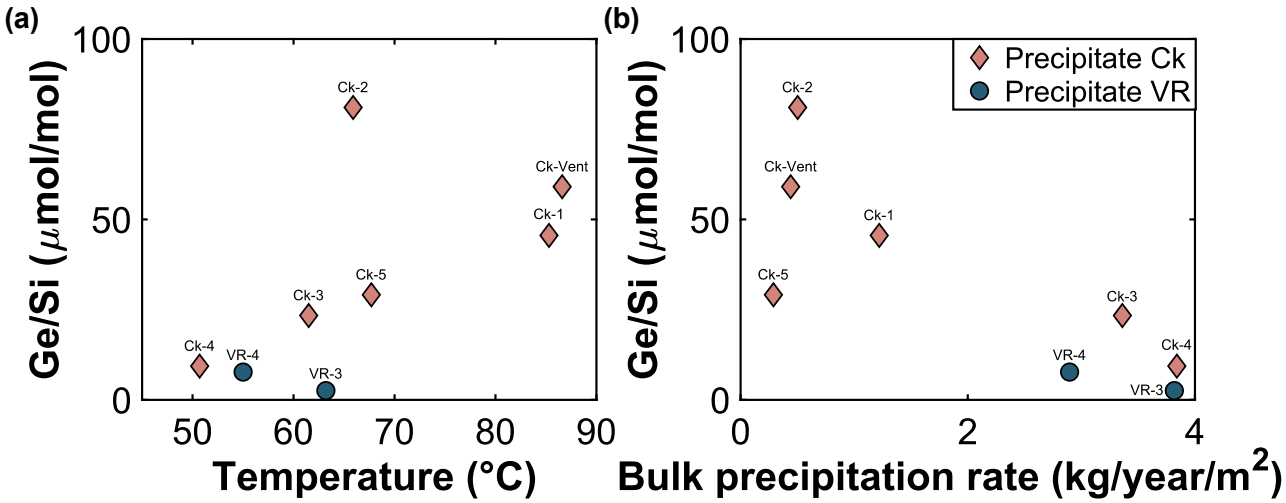

Figure 23: Ge/Si ratios as a function of temperature in ºC (a) and silica precipitation rate (kg/yr/m^2) (b) for the silica precipitation experiments at Ckoitchi (Ck, pink diamonds) and Vega Rinconada (VR, blue circles).

3.5. Geochemistry and Ge partitioning of active and fossil sinter deposits from El Tatio

3.5.1. Active sinter deposits at El Tatio

In addition to carrying out precipitation experiments, samples from active sinter deposits were collected at both Ckoitchi and Vega Rinconada for analysis. Specifically, at Ckoitchi (points 3 and 4), samples of sinter coated with microbial mats were extracted, identified as Co03-Organic, Co04-Organic, and Co04-Tofu, or collectively known as "Ck Org.". The biological material content was measured using the loss on ignition method (LOI) after air-drying the samples. The Co03-Organic sample had a LOI of 27%, while the Ck-4 samples reached 55% of LOI.

The concentrations for the active sinter samples at El Tatio are divided into two main groups based on the month in which the alkaline extraction was performed in 2022. For the January samples, the silica concentrations of the Ckoitchi samples range from 56 wt.% to 94 wt.%, averaging 82 wt.%, while those from Vega Rinconada range from 96 wt.% to 106 wt.%, which amounts to a 100 wt. % of silica concentration. The silica concentrations of the December samples in the Ckoitchi sector vary between 33 wt.% and 67 wt.%, with an average of 47 wt.%. For the Vega

Rinconada samples, the silica concentrations range from 68 wt.% to 79 wt.%, with an average of 73 wt.%. Lastly, for the Ck Org group, the silica concentrations have an average of 22 wt.%. In both the January and December groups, the silica concentrations of Vega Rinconada are higher than those of Ckoitchi. In addition, the Ck Org. samples have the lowest silica values among the samples. In terms of Ge concentrations, samples from the January Ckoitchi group range between 6.97 ppm and 13.72 ppm, with an average of 9.47 ppm. The Vega Rinconada samples range between 1.82-3.66 ppm, averaging 2.61 ppm. For the December samples, Ge concentrations at Ckoitchi range between 4.06-12.83 ppm, with an average of 6.99 ppm, and those from Vega Rinconada have concentrations between 1.27 ppm and 2.74 ppm, averaging 1.66 ppm. The Ck Org. group has concentrations between 6.42 ppm and 19.99 ppm, with an average Ge concentration of 11.34 ppm. In the January and December groups, the Ckoitchi samples consistently show higher germanium concentrations than Vega Rinconada's samples. Notably, the Ck Org group's samples stand out by achieving the highest germanium concentrations across all the samples.

Both silica concentrations at Ckoitchi (Figure 24a) and Vega Rinconada (Figure 24b) do not exhibit any discernible trend with respect to temperature. Furthermore, it is notable that for both locations, the silica levels in the January samples are higher than those in the December samples, showing a difference of 34% in the Ckoitchi samples and roughly 27% in Vega Rinconada. For Ge concentrations at Ckoitchi (Figure 24c) and Vega Rinconada (Figure 24d), there is also no trend with temperature. The January samples are slightly higher than the December samples, being almost identical in the Ck-5 point samples (67.7°C).

Table 12: Geochemistry of the active sinter deposits at El Tatio. The table lists alkaline extraction month in 2022, sampling temperature, sample site of the sample, SiO_2, Ge (ppt) and Ge/Si.

Sample ID	Alkaline Extraction Month 2022	Sample Site	T	SiO_2	Ge	Ge/Si
			°C	wt.%	ppm	µmol/mol
ET-03-Co01	January	Ck-1	85.3	56%	13.72	20.19
ET-03-Co02	January	Ck-2	65.9	94%	8.38	7.39
ET-03-Co03	January	Ck-3	61.5	92%	13.48	12.14
ET-03-Co04	January	Ck-4	50.7	85%	7.22	7.05
ET-03-Co05	January	Ck-5	67.7	74%	6.97	7.81
ET-03-Co07	January	Ck, 12 m from the vent	18	89%	7.06	6.59
ET-02-VR01	January	VR-1	86.6	96%	1.82	1.57
ET-02-VR02	January	VR-1	86.6	106%	-	-
ET-02-VR03	January	VR-2	74.4	105%	2.34	1.85
ET-02-VR04	January	VR-3	63.2	103%	3.66	2.94
ET03-Co01-1	December	Ck-1	85.3	33%	12.83	32.58
ET03-Co02.5-1	December	Ck-2	65.9	46%	7.28	13.09
ET03-Co03-1	December	Ck-3	61.5	51%	7.30	11.95
ET03-Co04-1	December	Ck-4	50.7	44%	5.25	9.89
ET03-Co05-3	December	Ck-5	67.7	44%	7.02	13.33
ET03-Co06-1	December	Ck-4	50.7	67%	4.06	5.03
ET03-Co07-3	December	Ck, 12 m from the vent	18	47%	5.19	9.17
ET02-VR01 -2	December	VR-1	86.6	68%	1.32	1.60
ET02-VR02 -1	December	VR-1	86.6	79%	1.27	1.33
ET02-VR03 -2	December	VR-2	74.4	74%	1.32	1.48
ET02-VR04 -2	December	VR-3	63.2	72%	2.74	3.15
Co03-Organic	December	Ck-3	61.5	31%	19.99	54.11
Co04-Organic	December	Ck-4	50.7	18%	7.61	34.37
Co04-Tofu	December	Ck-4	50.7	16%	6.42	33.54

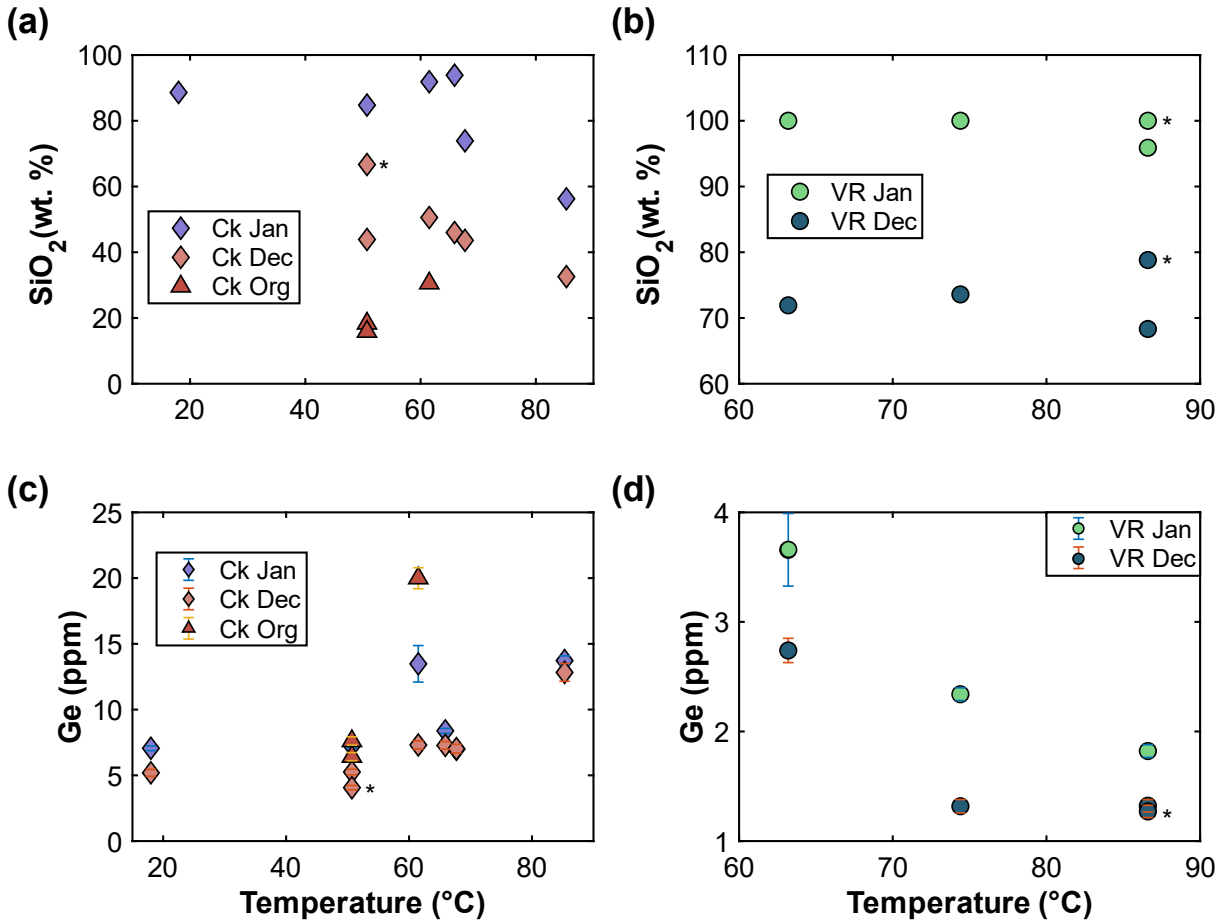

Figure 24: Silica (wt%) and Ge concentrations (ppm) in the Ckoitchi (Ck) and Vega Rinconada (VR) sectors as a function of temperature (°C), considering the alkaline extraction groups performed in January and December separately from the Ck Org samples. (a) Silica concentrations as a function of temperature for Ck samples. (b) Silica concentrations versus temperature for VR samples. (c) Ge concentrations as a function of temperature for Ck samples. (d) Ge concentrations versus temperature for VR samples. The diamonds correspond to the Ck samples, with the January samples indicated by purple and the December samples by pink. The asterisk (*) in Ck is used to represent a duplicate December sample from the Ck-4 point. Red triangles denote the Ck Org. group samples. Vega Rinconada samples are depicted as circles, with January samples shown in green and December samples in blue. The error bars depict the uncertainty in the Ge measurement. The asterisk in VR represents the duplicate sample VR-1.

Silica (Figure 25a for Ck and Figure 25b for VR) and Ge (Figure 25c for Ck and Figure 25d for VR) concentrations do not show any discernible trend as a function of bulk precipitation rate.

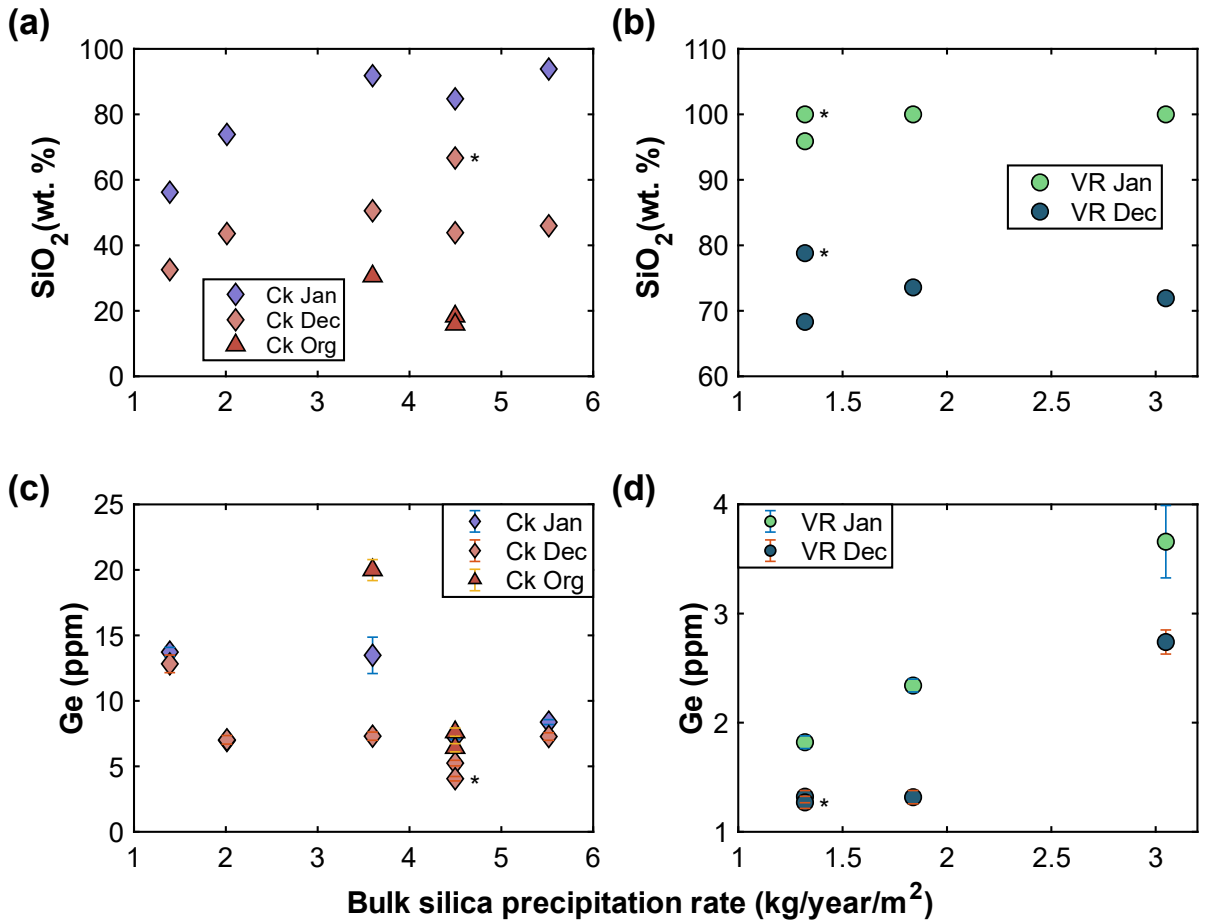

Figure 25: Silica (wt%) and Ge concentrations (ppm) in the Ckoitchi (Ck) and Vega Rinconada (VR) sectors as a function of the average Bulk silica precipitation rate (kg/year/m^2), considering the alkaline extraction groups performed in January and December separately from the Ck Org samples. (a) Silica concentrations as a function of Bulk silica precipitation rate for Ck samples. (b) Silica concentrations versus Bulk silica precipitation rate for VR samples. (c) Ge concentrations as a function of Bulk silica precipitation rate for Ck samples. (d) Ge concentrations versus Bulk silica precipitation rate for VR samples. The diamonds correspond to the Ck samples, with the January samples indicated by purple and the December samples by pink. The asterisk (*) in Ck is used to represent a duplicate December sample from the Ck-4 point. Red triangles denote the Ck Org. group samples. Vega Rinconada samples are depicted as circles, with January samples shown in green and December samples in blue. The error bars depict the uncertainty in the Ge measurement. The asterisk in VR represents the duplicate sample VR-1.

As mentioned above, assessing elemental ratios avoids the errors induced by different yields on the alkaline extractions, as Ge and Si dissolve stoichiometrically. Ge/Si ratios in the samples (Figure 26) range between 1.3 and 54.1 µmol/mol , with an average of 12.7 µmol/mol. The Ck samples show different Ge/Si ratios between those with high and low organic material content (bacterial mats). For the low organic material and silica-rich Ck active samples, the duplicate Ge/Si ratios obtained from two different digestions (Jan and Dec 2022) are shown in Figure 26a, with both datasets showing an increasing trend with respect to temperature. Mean Ge/Si ratios in the January extractions is 10.19 µmol/mol, ranging from 6.59 to 20.19 µmol/mol. For the December extractions, the average ratio is 13.58 µmol/mol, within a range of 5 to 33 µmol/mol. The organic samples show an average Ge/Si ratio of 40.7 µmol/mol, ranging from 33.54 to 54.11 µmol/mol. The VR samples show Ge/Si ratios within 1.33 and 3.15 µmol/mol (Figure 26b), and differences

between the duplicate samples are 0.23 µmol/mol on average. The VR active sinter samples show an inverse trend with respect to temperature, in contrast to the Ck samples. However, the VR samples show low variability in Ge/Si ratios (0.7 equivalent to one standard deviation), in contrast to the wider range observed in the Ck samples (14 µmol/mol standard deviation).

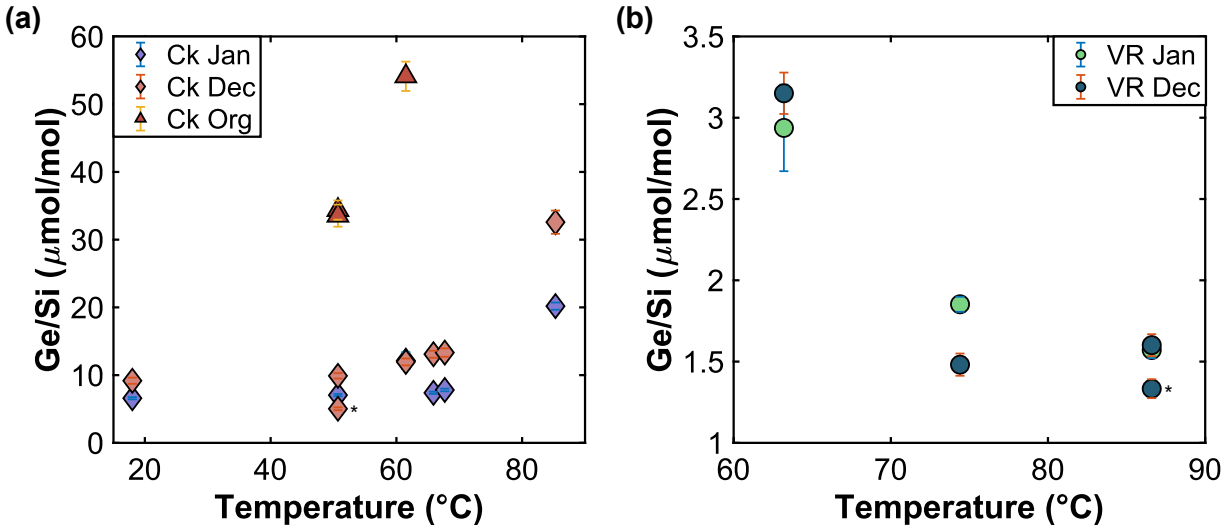

Figure 26: Ge/Si ratios in active (in-situ) sinter deposits as a function of temperature. (a) shows the Ckoitchi samples from January (purple diamonds), December (pink diamonds) and Organic (red triangles) as a function of temperature. (b) Vega Rinconada samples from January (green circles) and December (blue circles) as a function of temperature. The error bars depict the uncertainty in the Ge measurement.

Additionally, sixteen samples of other active sinter deposits from El Tatio will be considered in this study. Four of these samples are from this study, while four samples were obtained by Slagter et al. (2019) and eight by Munoz-Saez et al. (2020), the associated geochemical information is presented in Table 13. These additional samples have an average silica concentration of 93 wt.%, and an average Ge concentration of 2.8 ppm. The associated Ge/Si ratios range from 0.15 to 7.63 µmol/mol, with an average of 2.56 µmol/mol.

Table 13: Geochemistry of other active sinter deposits at El Tatio, considering some additional samples extracted in this work and by Slagter et al. (2019) and Munoz-Saez et al. (2020). The table lists the alkaline extraction month in 2022, data origin, sampling temperature, SiO_2, Ge (ppm), and Ge/Si.

Sample ID	Alkaline Extraction Date	Data Origin	T	SiO_2	Ge	Ge/Si
			°C	wt.%	ppm	µmol/mol
ET-LIN02	January	This work, Piscina Linzor	-	102%	1.98	1.61
ET-LC-01	January	This work, La Concha	84.1	98%	7.57	6.39
ET-LC-02	January	This work, La Concha	84.1	108%	3.40	2.60
ET-LC-03	January	This work, La Concha	84.1	102%	4.71	3.83
ET-414-CM	January	El Tatio, Slagter et al. (2019)	<40	79%	1.37	1.43
ET-420-CM	January	El Tatio, Slagter et al. (2019)	<40	96%	0.68	0.58
ET-435-CM	January	El Tatio, Slagter et al. (2019)	<40	97%	0.48	0.41
ET-441-CM	January	El Tatio, Slagter et al. (2019)	-	85%	3.71	3.63
ET-506-CM	January	El Tatio, Munoz-Saez et al. (2020)	<40	77%	5.42	5.82
ET-509-CM	January	El Tatio, Munoz-Saez et al. (2020)	<40	94%	2.32	2.04
ET-510DA-CM	January	El Tatio, Munoz-Saez et al. (2020)	<40	78%	7.22	7.63
ET-510NV-CM	January	El Tatio, Munoz-Saez et al. (2020)	40-75	101%	0.57	0.46
ET-512-CM	January	El Tatio, Munoz-Saez et al. (2020)	<40	100%	5.74	4.76
ET-514-CM	January	El Tatio, Munoz-Saez et al. (2020)	40-75	98%	0.27	0.22
ET-515-CM	January	El Tatio, Munoz-Saez et al. (2020)	>75	90%	1.18	1.09
ET-517-CM	January	El Tatio, Munoz-Saez et al. (2020)	40-75	103%	0.19	0.15
ETLIN02-1	December	This work, Piscina Linzor	-	70%	0.72	0.84

3.5.2. Fossil sinter deposits at El Tatio and correlation with ages and precipitation rates derived from radiocarbon dating.

The paleosinter deposit considered in this study (analogous to the paleosinter mound from Site 404 of Slagter et al., 2019) was also analyzed geochemically. The analysis revealed that silica concentrations within the paleosinter varied from 64 wt.% to 82 wt.%, averaging 76 wt.%, while germanium concentrations ranged from 244.3 ppb to 893.7 ppb, with a mean of 381.4 ppb. Additionally, the Ge/Si ratios fluctuated between 0.25-0.9 µmol/mol, averaging 0.41 µmol/mol (Table 14).

Table 14: Geochemistry of the Paleosinter deposit of this study). The table lists the alkaline extraction month in 2022, data origin, SiO_2, Ge (ppb), and Ge/Si. The asterisk (*) represents a laboratory duplicate sample of ET06-PSc1.

Sample ID	Alkaline Extraction Date	Data Origin	SiO_2	Ge	Ge/Si	Precipitation rates (Slagter et al. 2019)
			wt.%	ppb	µmol/mol	kg/years/m^2
ET06-PSa-2	December	This work, paleosinter	76%	277.05	0.30	0.988
ET06-PSb1-1	December	This work, paleosinter	72%	295.98	0.34	0.355
ET06-PSb2-a-2	December	This work, paleosinter	77%	352.57	0.38	0.563
ET06-PSb2-b-1	December	This work, paleosinter	75%	352.49	0.39	0.563
ET06-PSb3-1	December	This work, paleosinter	78%	385.11	0.41	0.189
ET06-PSc1-1	December	This work, paleosinter	64%	250.13	0.33	0.383
ET06-PSc1-B-2*	December	This work, paleosinter	82%	893.68	0.90	0.383
ET06-PSc2-2	December	This work, paleosinter	80%	244.34	0.25	-

Silica concentrations from the alkaline extractions in the paleosinter range between 64 to 82 wt.%. No trend is observed for the silica concentrations in the paleosinter mound as a function of age (Table 3, Figure 27a). Ge concentrations for the paleosinter extractions range between 244-385 ppb, with an average of 308 ppb. Similarly to SiO_2, Figure 27b shows no evident trend in Ge concentrations as a function of sample age. It is evident that the duplicate sample (marked with an asterisk *) exhibits abnormally high Ge when compared to the rest of the samples.

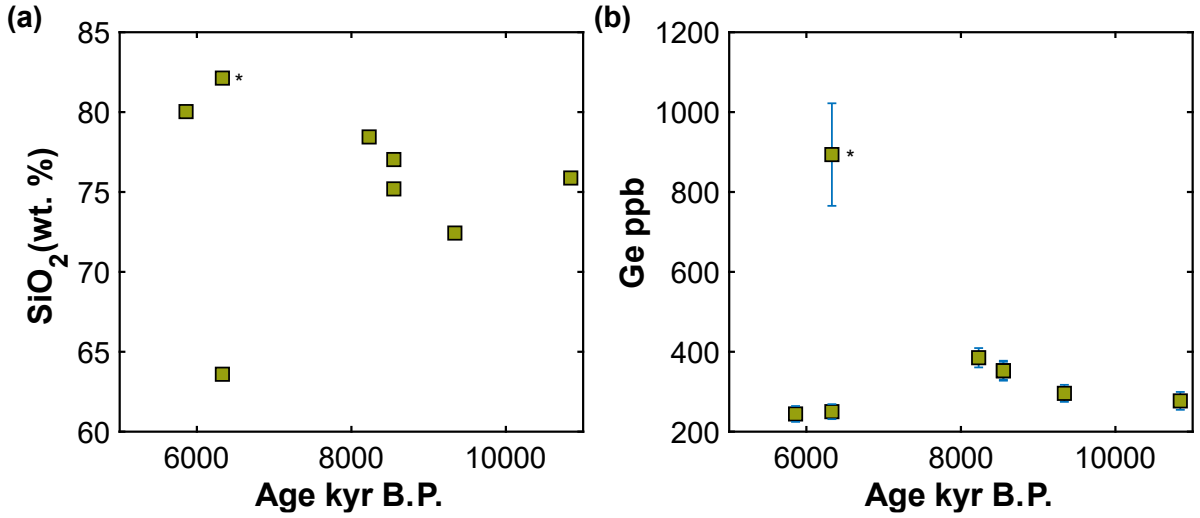

Figure 27: Silica (a) and germanium (b) concentrations in the Paleosinter as a function of ages obtained by radiocarbon dating according to Slagter et al. (2019) for the analogous samples. A duplicate analysis was performed to the sample corresponding to 6330 yr B.P. (ET06-PSc1), shown with an asterisk (*) in the figure.

Upon analyzing the Ge/Si ratios as a function with sample age (Figure 28), the results mirror those of Ge concentrations as expected due to the relatively constant silica contents, and thus, no distinct trend for Ge/Si ratios is observed as a function of age. Similarly, no trend can be identified

when comparing Ge/Si data with average precipitation rates derived from radiocarbon dating (Table 14, Figure 28).

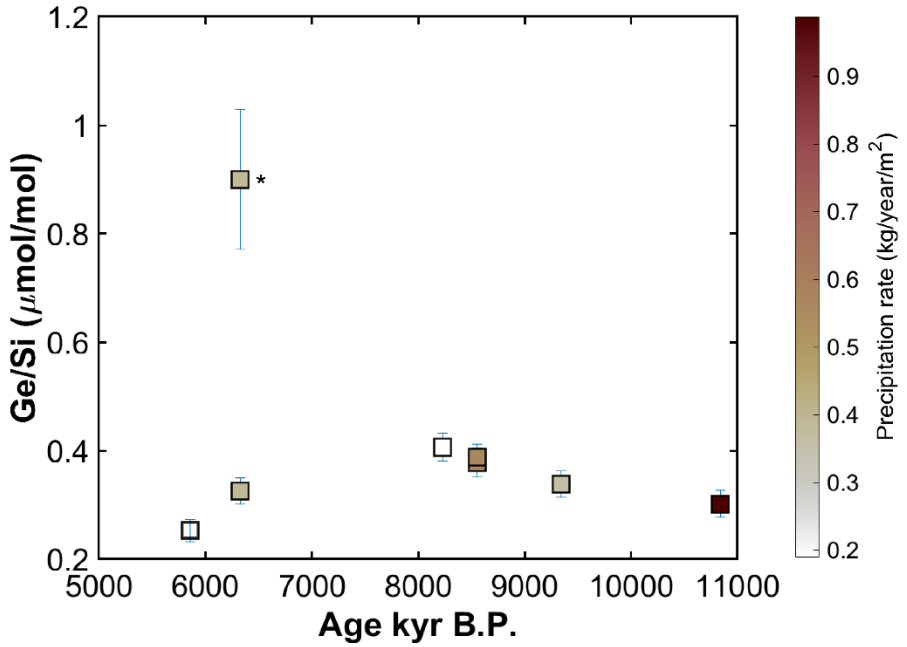

Figure 28: Ge/Si ratios in Paleosinter samples as a function of ages by radiocarbon dating and precipitation rates obtained by Slagter et al. (2019) for analogous samples. A duplicate analysis was performed to the sample corresponding to 6330 yr B.P. (ET06-PSc1), shown with an asterisk (*) in the figure.

For geochemical analysis, four additional samples of El Tatio fossil sinters were included from studies by Slagter et al. (2019) and Munoz-Saez et al. (2020), the results of which are presented in Table 15. The silica concentrations in these samples are fairly consistent, varying between 82 wt.% and 95 wt.%, with the average concentration being around 90 wt.%. The germanium concentrations, on the other hand, span from 695 to 6869 ppb, with an average concentration of 2675 ppb. Analyzing the resulting Ge/Si ratios, these fall between 0.6 to 6.4 µmol/mol, averaging at 2.5 µmol/mol.

Table 15: Geochemistry of other fossil sinter deposits at El Tatio, considering additional samples from Slagter et al. (2019) and Munoz-Saez et al. (2020). The table lists the alkaline extraction month in 2022, data origin, SiO_2, Ge (ppt), and Ge/Si.

Sample ID	Alkaline Extraction Date	Data Origin	SiO_2	Ge	Ge/Si
			wt.%	ppb	µmol/mol
ET-408-CM	January	El Tatio, Slagter et al. (2019)	82%	1502.50	1.52
ET-500-CM	January	El Tatio, Munoz-Saez et al. (2020)	94%	694.67	0.61
ET-501-CM	January	El Tatio, Munoz-Saez et al. (2020)	95%	1635.23	1.42
ET-502-CM	January	El Tatio, Slagter et al. (2019)	89%	6868.90	6.36

3.6. Geochemistry of active sinter deposits from other locations

To evaluate Ge/Si ratios in active siliceous sinter deposits as a function of other geothermal fields besides El Tatio, samples from the Alpehue (Pérez, 2019) and Puchuldiza (Sanchez-Yanez et al., 2017) geothermal fields were included in this study. The Alpehue geyser field is located on the southeast flank of the Sollipulli volcano (38°58′26”S, 71°31′11”W), at an elevation of 1350 m.a.s.l., in the Southern Volcanic Zone of Chile. This area encompasses at least four geysers within approximately 0.2 km^2 (Munoz-Saez et al., 2020). Conversely, the Puchuldiza geothermal field is situated at an altitude of 4200 m.a.s.l., in northern Chile (19°24’46.5”S, 68°57’35.6”W), and spans an area of about 1 km^2 (Lahsen, 1978; Sanchez-Yanez et al., 2017) with about 170 thermal sources (Trujillo, 1970).

The silica concentrations in the examined sinters (Table 16) average 76 wt.% in Alpehue and reach 80 wt.% of SiO_2 in Puchuldiza. Ge concentrations in the samples range between 686.5 ppb and 3307.8 ppb in Alpehue, with an average of 2074.9 ppb. In Puchuldiza, the concentrations vary between 152.2 ppb and 6382.5 ppb, with an average of 2576.7 ppb. Ge/Si ratios range between 0.7 and 3.7 μmol/mol in Alpehue and between 0.2 and 7.8 μmol in Puchuldiza. Alpehue has lower average ratios compared to Puchuldiza (2.3 vs. 2.9 μmol/mol respectively).

Table 16: Geochemistry of other active sinter deposits at Alpehue (Perez, 2019) and Puchuldiza (Sanchez-Yanez et al., 2017). The table lists the alkaline extraction month in 2022, data origin, SiO_2, Ge (ppb), and Ge/Si.

Sample ID	Alkaline Extraction Date	Data Origin	SiO_2	Ge	Ge/Si
			wt.%	ppb	μmol/mol
ALP-02-M1-1	December	Alpehue, Perez Nuñez (2019)	73%	3307.77	3.74
ALP-05-M2-1	December	Alpehue, Perez Nuñez (2019)	78%	1830.20	1.95
ALP-05-M7ISO-1	December	Alpehue, Perez Nuñez (2019)	76%	2474.96	2.69
ALP-01-M4-1	December	Alpehue, Perez Nuñez (2019)	78%	686.47	0.73
D2P2R-1	December	Puchuldiza, Sanchez-Yanez et al. (2017)	83%	-	-
D2P5-1	December	Puchuldiza, Sanchez-Yanez et al. (2017)	84%	2220.35	2.19
D2P6R (EN)-1	December	Puchuldiza, Sanchez-Yanez et al. (2017)	80%	1551.83	1.60
D3P1mondat-1	December	Puchuldiza, Sanchez-Yanez et al. (2017)	68%	6382.50	7.77
D3P6B-1	December	Puchuldiza, Sanchez-Yanez et al. (2017)	86%	152.16	0.15

CHAPTER 4: DISCUSSION

4.1. Ge/Si ratios in hydrothermal fluids across hot springs types in El Tatio

El Tatio hydrothermal fluids of chloride-rich composition analyzed in this study are subdivided into three categories: geysers, thermal pools, and a perpetual spouter. Based on the specific conductance and chloride concentrations of the three groups, it is possible to establish that the perpetual spouter (Ckoitchi) is the most diluted, which could be explained due to its closer proximity to the Salado River (i.e., Cortecci et al., 2005; Munoz-Saez et al., 2018). It is not possible to establish a correlation between Si and Ge concentrations and temperature, nor it is possible to establish any trend with respect to the type of hot spring. Similarly, there is no apparent relationship between Ge/Si ratios and temperature or manifestation type. This observation agrees with Gaspard et al. (2021a), who suggest that Ge/Si ratios in hot springs do not necessarily reflect the compositional type of the fluid or type of hydrothermal manifestation.

To contextualize the Ge/Si ratios of El Tatio fluids globally, Ge/Si ratios and silica concentrations were compiled from hot springs worldwide (Figure 29). Ge/Si in thermal fluids from El Tatio show the highest Ge concentrations and Ge/Si ratios between 80 to 100 µmol/mol when compared to those from geothermal fields hosted in volcanic provinces such as Yellowstone or Iceland, with a dominance of Cl-rich fluids with high silica concentrations, (Arnórsson, 1984; Gaspard et al., 2021a). The main difference between the El Tatio and the Icelandic hydrothermal fluids is given by their chloride concentration, as the El Tatio samples are more concentrated by a factor of almost 70. The higher salinity of the hydrothermal fluids enhances the surface reactivity of silica in solution (Icenhower & Dove, 2000). The rest of the hydrothermal fluids surveyed worldwide exhibit different silica and Ge compositions and lower temperatures. For example, the Polish springs from the Sudetes Mountains, associated with a basin and fault tectonics, have low Ge concentrations (0.025 to 10.62 µg/L) and temperatures ≤ ~30°C (Dobrzynski et al., 2018). These fluids are characterized by being rich in CO_2, rather than chloride, and their Ge/Si ratios are ~40 µmol/mol. The Massif Central hot springs, from an intracontinental rifting and extensional tectonic setting, generally have temperatures below 20°C, with two springs reaching nearly 60°C, and are also rich in CO_2, showing Ge/Si ratios of 337 µmol/mol on average (Criaud & Fouillac, 1986). The Himalayan springs—associated with continental collision and orogeny—range in temperature from 20°C to 70°C and are mainly Na^+-HCO_3^-- Ca^{2+}-Cl^- waters with pH around neutrality and showing Ge/Si ratios of 260 µmol/mol on average (Evans & Derry, 2002; Evans et al., 2004). Finally, the Guadeloupe hot springs located in around the volcanic field show different compositions from sulfate, carbonate, and chloride richs fluids, but their Ge/Si ratios are lower compared to El Tatio, reaching an average Ge/Si ratio of only 4 µmol/mol (Gaspard et al., 2021a).

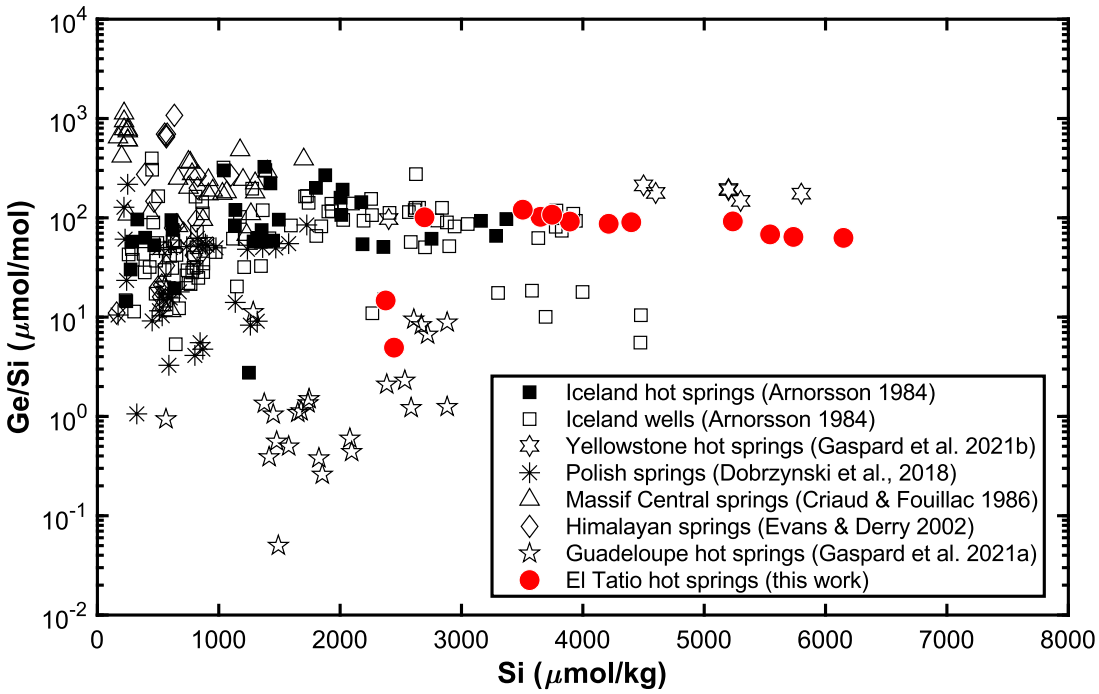

Figure 29: Fluid Ge/Si ratios versus Si (μmol/kg) in hot springs from El Tatio Geothermal Field in red circles, plus a compilation of hydrothermal fluids from around the world. Legend is the same as Figure 1. Ge/Si data were compiled from Arnórsson (1984), Criaud & Fouillac (1986), Dobrzyński et al. (2018), Evans & Derry (2002), Gaspard et al. (2021a) and Gaspard et al. (2021b).

As for the different sampling points considered for Ckoitchi and Vega Rinconada, silica concentrations in the fluids remain relatively uniform at different temperatures, and hence different distances from the vent, with slightly lower concentrations at the vent (Figure 13a). Ge concentrations, show a similar trend, and present lower Ge concentrations downstream (Figure 13b). This is in agreement with Kraynov (1967), who associated high Ge concentrations in carbonate thermal waters with high temperatures. Ge/Si ratios obtained from both the perpetual spouter and the geyser of interest range from 68.5 μmol/mol to 111 μmol/mol. Although the fluid concentrations are relatively uniform, the Ge/Si ratios do show trends as a function of temperature. This study shows that the Ge/Si ratios in the fluids increase with temperature. This observation agrees with the model proposed by Evans & Derry (2002), which predicts an increase in the Ge/Si fluid ratio with rising temperature. These authors propose that Si is scavenged from the fluid through quartz or opal precipitation, thus increasing the Ge/Si ratio of the fluids (e.g., Evans et al., 2004). This is in agreement with previous findings by Mortlock et al. (1993), who observed a trend of increasing Ge/Si towards lower silica concentrations in hydrothermal fluids from black smoker vents. The conservative behavior of Ge in the fluid also agrees with batch silica precipitation experiments showing high Ge/Si ratios in the fluid associated to faster removal of silica in opal at 25ºC (Fernandez et al., 2021). Given that the variability in silica concentrations is more pronounced than that of Ge concentrations when comparing Ckoitchi and Vega Rinconada, it could be argued that the observed disparities in their ratios, notably higher in Ckoitchi, may be attributable to its diminished silica concentration, similar to the finding of Mortlock et al. (1993), where the Ge/Si ratio increases at lower Si concentrations in the fluid.

4.2. Efficiency of opal alkaline extractions in close to equilibrium solutions

The alkaline extractions used here for dissolving only the opaline silica in the collected samples resulted in varying total silica concentrations in all the solid samples (including precipitates, in-situ modern sinters, and paleo sinters), with ranges between 28 and 108 wt.% SiO_2. Although some variability in silica concentrations is expected between depending on the amount of either detrital material, salts, organic matter, or other neo-formed minerals such as clays, iron oxides or sulfides; silica concentrations should range between 60-94 wt.% SiO_2 (Lynne et al., 2005 ; Inagaki et al., 1997; Nicolau, 2013). Additionally, our SEM semiquantitative data indicates that silica concentrations in the precipitates show average silica concentrations of 88.7 wt.% for Ckoitchi and 89.1 wt.% for Vega Rinconada, while the in-situ sinter samples in the vents would reach 77 wt.% for Ck and 85 wt.% in VR (Table 17 in ANNEX C), and thus any additional material might only amount up to ~20% weight of the total sample. Moreover, silica concentrations in one paleosinter from El Tatio show 90 wt.% SiO_2 (Wilmeth et al., 2020), while this study, here we only obtained an average silica concentration of 76 wt.% in the paleosinter, and an average of 90 wt.% for other fossil sinter deposits at El Tatio. The Puchuldiza samples in this study yielded an average silica content of 80 wt.%, whereas Sanchez-Yanez et al. (2017) reported for the same samples an average of 87.1 wt.%. The disparity of our silica concentration data among the solid samples, and their discrepancy with both the SEM semiquantitative concentration analyses, and the published data in El Tatio and other systems, suggests that the silica concentrations obtained through the alkaline extractions are not necessarily accurate. For further insight, we analyze a set of duplicate samples that were digested eleven months apart (January 2022 and December 2022), but analyzed during the same round (January 2023).

The analyses of the alkaline extractions performed in January 2022 for both Ckoitchi and Vega Rinconada yielded higher silica concentrations compared to the samples from the December 2022 alkaline extractions. The Vega Rinconada samples show an average difference of 26% (with differences between 21-28%), while the Ckoitchi samples show an average difference of 38% (with a minimum difference of 24% and a maximum of 48%). That is, silica concentrations are higher in samples whose alkaline extraction was performed eleven months prior to the analysis. A plausible explanation for the differences observed between the duplicate samples that were allowed to react for either one or eleven months prior to their analysis is due to slow silica dissolution kinetics. The alkaline extraction process to purify the samples, considered that the alkaline extraction solutions had a pH over > 9 and were allowed to react for over a week at 85ºC to promote faster dissolution (Mortlock and Froelich, 1996). However, the disparity between both batches, shows that the sampled that solutions that allowed dissolution at room temperature for a longer period, yielded higher silica concentrations which are close to 90-100% wt. as expected. It is important to note that the alkaline solutions were close to silica saturation, as the method was limited by the volume of the batch dissolution containers (250 mL for VR, and 125 mL for Ck), and the stability of the analytical balance to weight less than 20 mg of powdered sample. Such small amount of sample is required to make sure each extraction solution is below amorphous silica saturation (< 100 mg/L). However, weighting less than 20 mg of sinter samples is hard given the highly charge surface of amorphous silica, which affects the stability of the electronic balance. The slow kinetics of silica dissolution are explained by an initial fast dissolution stage due to the elimination of chemisorbed silicic acid, followed by slower dissolution stage due to the surface reorganization of amorphous silica, which causes the fast dissolution to not be favored (Fleming, 1986). Previously, Krauskopf

(1956) proposed that the slower dissolution of opal is caused by its smaller surface area. Additionally, Demarest et al. (2009) suggested that the dissolution rate of biogenic silica decreases probably due to a reduction in the total surface area. Despite the mechanisms determining the slow dissolution kinetics of amorphous silica, slower dissolution rates are enhanced when dissolution is carried out under under near equilibrium conditions (e.g., Dove et al., 2005; Maher et al., 2009; A. F. White et al., 2008; White & Brantley, 2003)These characteristics would have affected the alkaline extraction efficiency for the opal solutions in the near-equilibrium conditions of the samples in this study.

4.3. Silica precipitation rates in El Tatio and their comparison to other kinetic models and field sites

Following the discussion by Munoz-Saez et al. (2023), the measured silica precipitation rates were compared with two precipitation rate models obtained by Rimstidt & Barnes (1980) (Equation 6) and Carroll et al. (1998) (Equation 7). Equation 6 was determined from laboratory experiments, considering a pre-exponential factor A = 2.02 (mol/m^2/s), and activation energy Ea = 49.8 (kJ/mol). Equation (7) was determined from field experiments. For both cases, [H_4SiO_4(aq)] corresponds to the silica concentration in the fluid (in mol/kg) and K_{eq} is the temperature-dependent solubility constant for amorphous silica (Gunnarsson & Arnorsson, 2000).

$$R_{R\&B}(\mathrm{mol/m^2/s}) = -A\exp(-E_a/RT) \times (1 - [H_4SiO_{4(aq)}]/Keq) \quad (6)$$

$$R_{Carroll}(\mathrm{mol/m^2/s}) = 10^{-10.00\pm0.06}\exp([H_4SiO_{4(aq)}]/K_{eq})^{4.4\pm0.3} \quad (7)$$

$$logK_{eq}(T) = -8.476 - 485.24\,x\,T^{-1} - 2.268\,x\,10^{-6}\,x\,T^2 + 3.068\,x\,log(T) \quad (8)$$

Figure 30 shows the curves resulting from both silica precipitation models together with box plots representing the multiple precipitation rates obtained in our precipitation experiments at each temperature point in both Ckoitchi and Vega Rinconada. The data obtained in this study do not fit any of the models employed. However, the equation of Carroll et al. (1998) captures the inverse relationship between precipitation rate and temperature observed in our data. The laboratory-based model (Rimstidt & Barnes, 1980) appears to underestimate silica precipitation rates, while the field-based model (Carroll et al., 1998) does the opposite especially at lower temperatures.

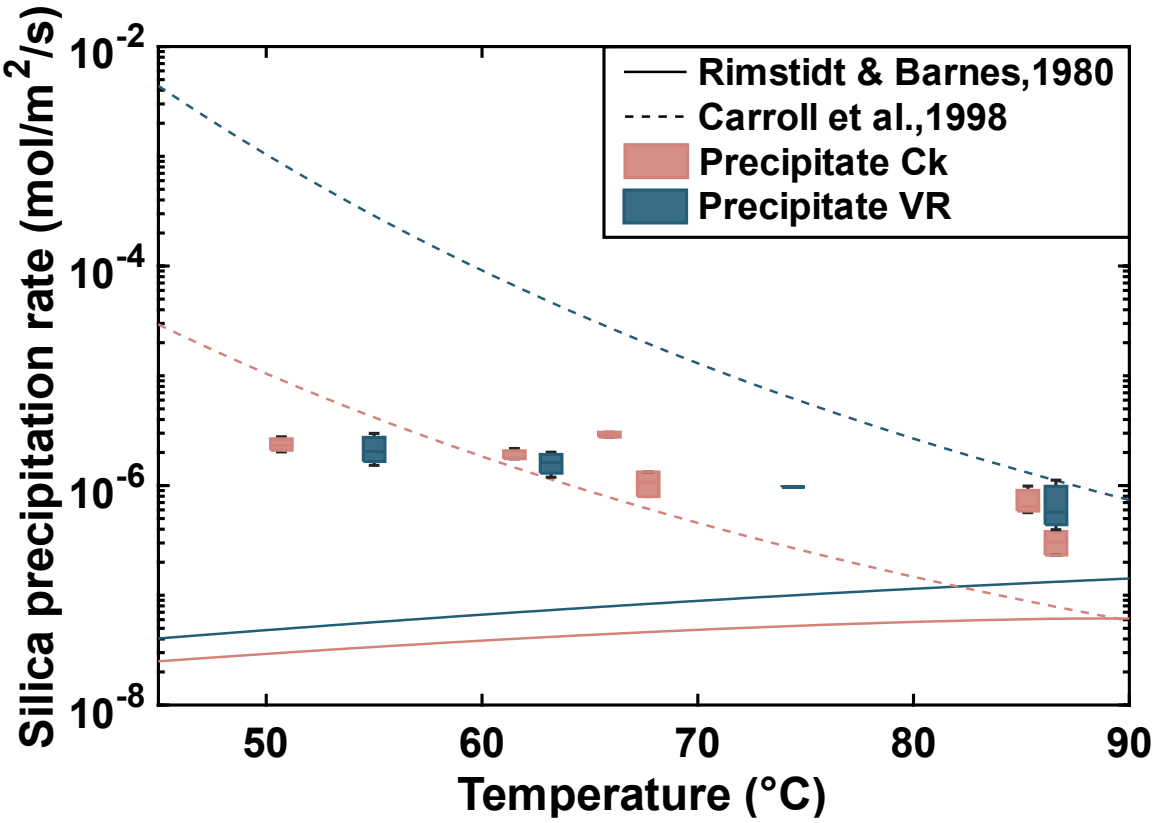

Figure 30: Measured silica precipitation rates and modeled rates from Carroll et al. (1998) (dashed lines) and and Rimstidt & Barnes (1980) (solid lines). The pink boxes correspond to the Ckoitchi precipitates and the blue boxes to the Vega Rinconada precipitates. The modeled curves assume the fluid silica concentration is equal to those at the vents of Ck (pink) and VR (blue).

In Figure 31, the rates derived from this study are compared with silica precipitation rates obtained in El Tatio (Nicolau et al., 2014; Slagter et al., 2019) and other geothermal fields in the world (Braunstein & Lowe, 2001; Handley et al., 2005; Konhauser et al., 2001; Mountain et al., 2003; Tobler et al., 2008). The silica precipitation rates measured in this study agree with previous results obtained in El Tatio, showing that precipitation rates here are among the highest recorded globally. The silica precipitation rates obtained in our experiments are slightly higher than those obtained previously. Our investigation yielded a range of 0.6 to 5.5 kg/yr/m^2 with an average of 2.7 kg/yr/m^2. In contrast, Nicolau et al. (2014) shows an average of 2.5 kg/yr/m^2, while Slagter et al. (2019) reported an average of 1.9 kg/yr/m^2. Our differences with previous studies in El Tatio might stem from methodological differences regarding the type of material used to collect the precipitates: etched glass slides (our experiment), versus sandpaper strips (Slagter et al., 2019), or smooth glass slides (Nicolau et al., 2014). Additionally, the experiments by Nicolau et al. (2014) were conducted in another hot spring vent in El Tatio with different hydrodynamics and chemistry than the Ck and VR hot springs. Besides silica, water, salts and organic matter can add up to the total accumulated mass that gets factored into the rates with up to 15-20% of weight (Garcia-Valles et al., 2008; Jones & Renaut, 2004; among others). Despite these corrections, the silica precipitation rates measured in this study are much higher than those reported in other geothermal fields.

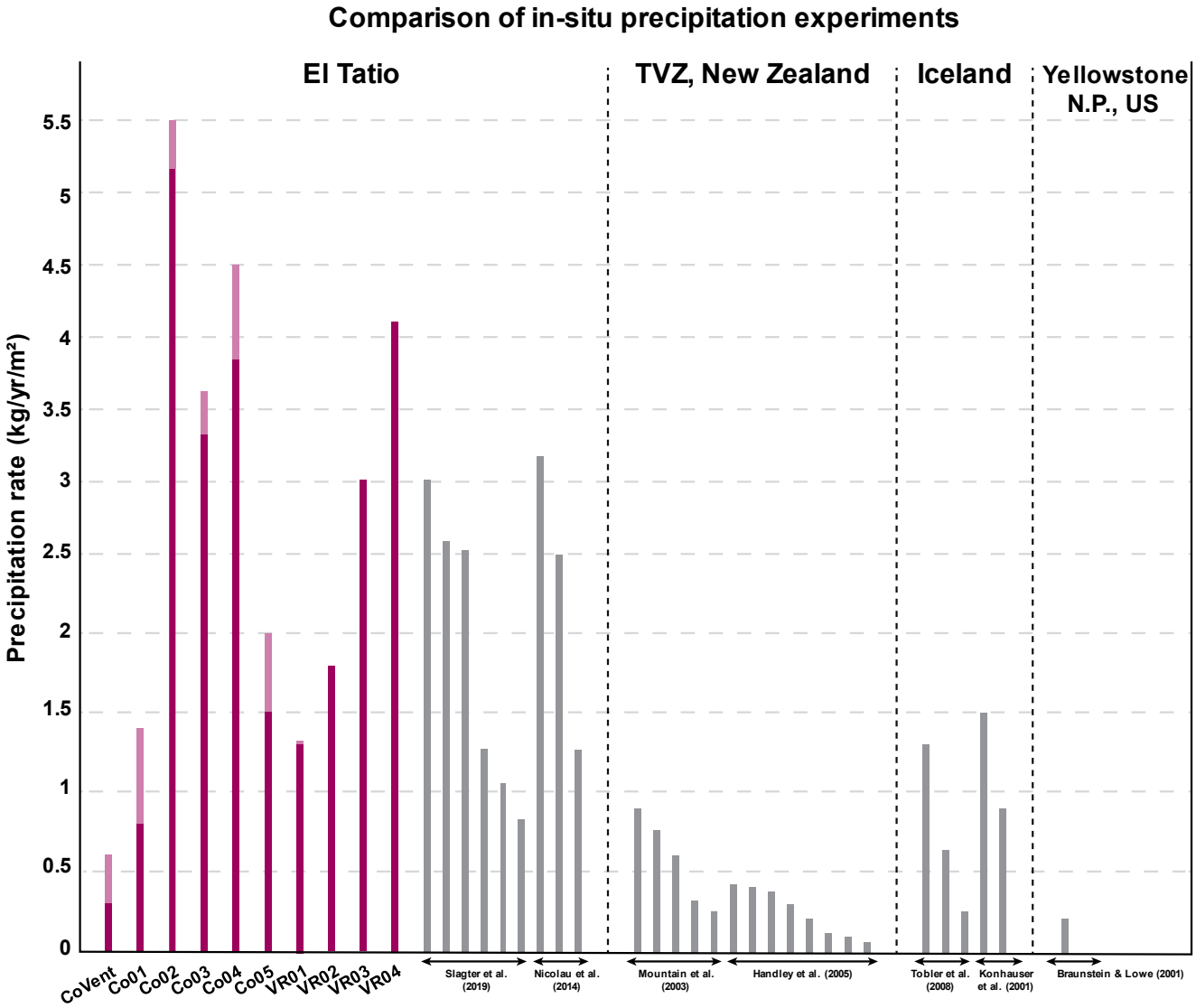

Figure 31: Comparative scheme of silica precipitation rates in different studies both in El Tatio and other geothermal systems around the world. The samples in color (first group) correspond to those obtained in this work. The light pink color represents the bulk silica precipitation rate, while the dark pink color corresponds to the adjusted silica precipitation rate. The other two groups of rates in El Tatio (in gray) were established by Slagter et al. (2019) through in situ precipitation experiments on sandpaper strips and by Nicolau et al. (2014) in glass slides. Experiments in New Zealand (Handley et al., 2005; Mountain et al., 2003), Iceland (Konhauser et al., 2001; Tobler et al., 2008) and Yellowstone, U.S. (Braunstein & Lowe, 2001) were also performed on glass slides (gray color). Figure modified from Slagter et al. (2019).

The findings of this investigation show a correlation between precipitation rates and temperature, with higher precipitation rates as the hydrothermal fluid cools downstream from the vent. These results agree with the observations from Carroll et al. (1998). Lower temperatures lead to the oversaturation of geothermal waters due to decreased solubility in this temperature range (Gunnarsson & Arnorsson, 2000). Additionally, Scott et al. (2024) proposed that the gradual decrease in silica polymerization rate with increasing temperature may be attributed to higher concentrations of $Si(OH)_{4(aq)}$ at equilibrium, which inhibits polymer formation by reducing reactive surfaces.

Based on the precipitation rates observed in this study, the different geochemical and hydrodynamic characteristics of two thermal manifestations, a perpetual spouter, and a geyser, do not affect the consistent results of the rates, as demonstrated in Figure 14. The precipitation rates in El Tatio are primarily influenced by extreme conditions such as fluid temperatures, temperature fluctuations, strong winds, and high radiation, as noted by Nicolau et al. (2014) and Slagter et al. (2019).

4.4. Partitioning of Ge during silica precipitation from hydrothermal fluids

Trace elements are selectively incorporated in the different phases during precipitation, with their distribution being sensitive to fractionation processes. The distribution of trace elements in minerals can be described by partition coefficients (K_D), which evaluate the incorporation of the trace element in the solid versus liquid phase. Lorens (1981) determined partition coefficients as a function of precipitation rates of some metals in calcite by using laboratory precipitation experiments. He observed that in addition to solution composition, precipitation rate is an important factor in the concentration of trace metals in calcite. Studies of metals and metalloids in sinters, such as arsenic, gold, or silver, have focused on their relationship to mineral exploration. (e.g. Guido et al., 2002; Parker & Nicholson, 1990; Pope et al., 2005). The study by Sanchez-Yanez et al. (2017), for example, aimed to investigate the effects of silica precipitation and diagenetic maturation on the incorporation of trace elements in sinters. The findings indicated that diagenetic transitions play an important role in the absorption of trace elements in sinters, with gold and silver becoming enriched in more crystalline phases, while boron and arsenic are enriched in more amorphous or immature phases.

4.4.1. The effect of water evaporation in fast silica precipitation and the partitioning of Ge in supersaturated silica-rich hydrothermal fluids

Since evaporation of hydrothermal fluids plays a role in the formation of sinters, some studies have focused on this factor (e.g., Orange et al., 2013; White et al., 1956). Previously at El Tatio, Nicolau et al. (2014) measured in-situ open-field evaporation rates at El Tatio concluding/estimating that evaporation contributes to silica precipitation by increasing the concentration of silica in the fluid, leading to its supersaturation and thus promoting opal precipitation. Additionally, the temperature of the hydrothermal fluids and heat from the ground can enhance evaporation beyond open-field values. For this work, evaporation rates were assessed through daily measurements of evaporated and remaining volumes using graduated cylinders. Consequently, the ground temperature to which each cylinder was exposed influenced the observed evaporation rates. Furthermore, this method restricts the exposed evaporation surface to the cross-sectional area of each cylinder. As a result, it does not accurately replicate ideal surface conditions in an open field, but it allows for tighter control over the volume of evaporated fluid.

The Ge/Si ratios in the remaining fluid increase as evaporation progresses, controlled by the decreasing concentrations of silica in the fluid. In the experiment, silica precipitates while Ge is not incorporated into the solid phase, due to the conservative behavior of Ge observed in the remaining fluid. This agrees with the study by Evans & Derry (2002), which suggests that high Ge/Si ratios in hot springs are attributed to subsurface precipitation of opal or quartz that is low in Ge.

High evaporation rates enhance fast silica removal from the fluid through fast silica precipitation (Nicolau et al., 2014), plus, fast opal precipitation leads to a delay in the partitioning of Ge into the solid phase (Fernandez et al., 2021). Therefore, the increasing Ge/Si ratios throughout the evaporation experiments are consistent with fast silica removal in nano-colloids and SiO_2 nuclei as observed experimentally (Fernandez et al., 2021).

4.4.2. The effect of fluid temperature and silica precipitation rates in the partitioning of Ge into opal

The silica precipitation experiments in this work allowed to constrain the effect of both fluid temperatures, and thus silica precipitation rates, in the partitioning of Ge into the opal precipitates. Here I discuss the results obtained from both opal precipitates obtained through a precipitation experiment, and from in-situ sinter samples collected along the same thermal gradient as the precipitates. The first observation from our results is that Ge/Si ratios in both precipitates and in-situ sinter deposits decrease with temperature downstream from the vent, meaning that the highest ratios observed are found closer to the vent, where precipitation rates are slow at high Tº (Figure 23b and 32), while the lowest Ge/Si ratios are found far from the vents where precipitation rates are high. Additionally, as mentioned before, the same behavior is observed for Ge/Si ratios in the hydrothermal fluids: meaning that Ge/Si in the fluids increase with faster precipitation rates (Figure 33). This effect was also seen in the evaporation experiments, as Ge/Si ratios in the fluid increase when higher volumes of the fluid evaporates, which allows further silica precipitation, which, in turn, inhibits Ge incorporation, causing the appearance of a conservative behavior during the duration of the experiment (six days), in agreement with what was also reported by Fernandez et al. (2021).

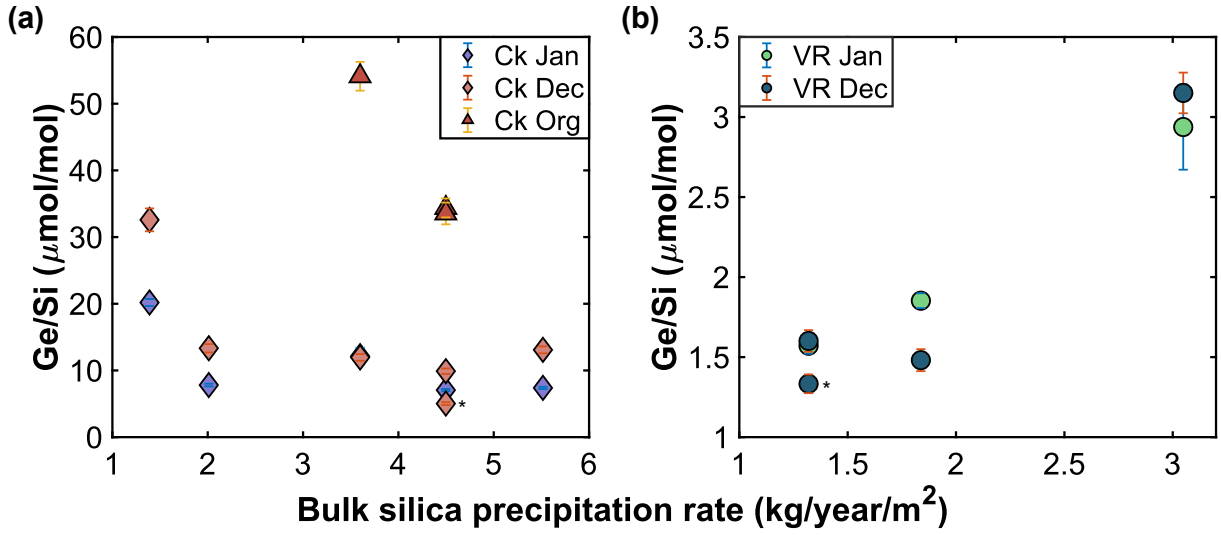

Figure 32: Ge/Si ratios of active (in-situ) sinter deposits as a function of bulk silica precipitation rates. Panel (a) shows Ckoitchi samples from the extractions performed in January (purple diamonds), December extractions (pink diamonds) and organic matter rich samples (red triangles) as a function of the bulk precipitation rate. (b) Vega Rinconada samples from January extractions (green circles) and December extractions (blue circles). The error bars depict the uncertainty in the Ge measurement.

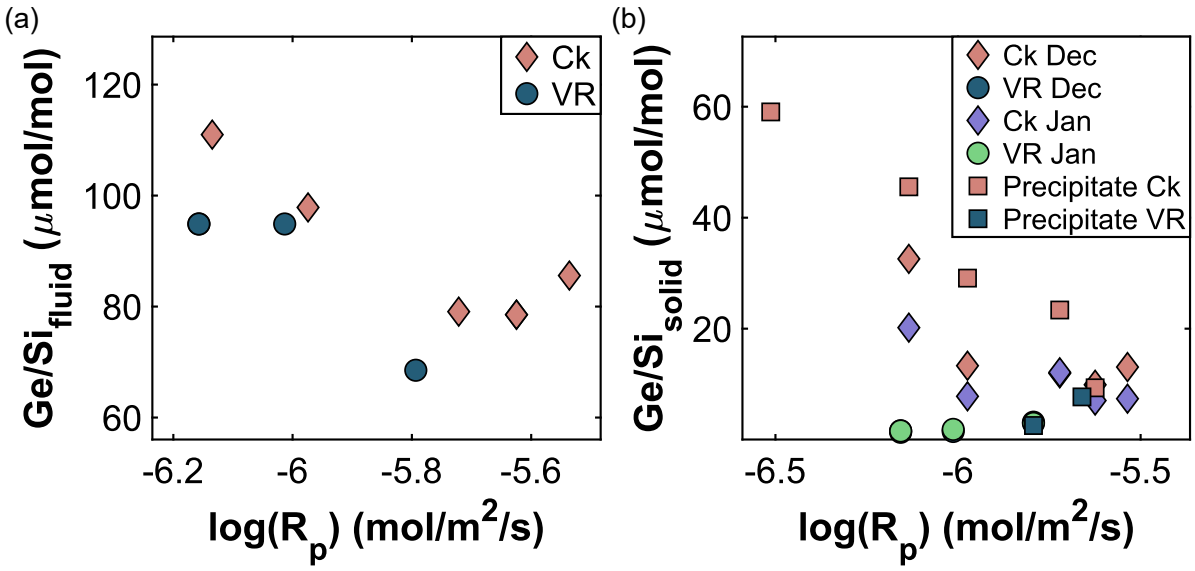

Figure 33: Ge/Si ratios for fluids (a) and for both active precipitates (in-situ) and those from the precipitation experiment (b), plotted as a function of precipitation rates from the experiment, for the Ckoitchi (pink and purple diamonds, pink squares) and Vega Rinconada (green and blue circles, blue squares) sectors.

The observed behavior in both solids (precipitates and in-situ samples) and fluids can be either explained by: 1) non-favorable equilibrium partitioning of Ge into the opal structure; or 2) a kinetic effect which delays Ge partitioning into the solid at higher silica precipitation rates. Although the equilibrium partition coefficient of Ge into amorphous silica has not been experimentally determined, themodynamic data from quartz and its Ge-bearing analog—argutite ($GeO_{2(hex)}$)— indicates that Ge should partition into the quartz¸and thus, the opal structure (Fernandez et al., 2021; Pokrovski et al., 2005; Pokrovski & Schott, 1998b). Therefore, the first hypothesis can be ruled out. To investigate the kinetic delay of Ge partitioning into amorphous silica, Fernandez et al. (2021) examined the relation between the apparent partition coefficient K_D (Eq. 5) and opal precipitation rates. Based on their modeled projections, it is anticipated that extensive incorporation of Ge would occur under conditions close to equilibrium, with a projected equilibrium K_D = 12.8 at 25°C. This means that apparent K_D should increase over time as equilibrium is achieved. In Fernandez et al. (2021) 35-day laboratory experiment, the apparent partition coefficient shows a decreasing trend due to the fast removal of silica from the fluid, which should over turn as silica removal slows down, resulting in an increase in K_D. In our study, the precipitation experiment spanned over 200 days, allowing to observe this over turn as silica precipitation rates decrease (Figure 34). Additionally, this same trend can be observed in the in-situ sinter samples (Figure 35). These relations would support the model projections by Fernandez et al. (2021) in which Ge incorporation becomes favorable at equilibrium-controlled conditions, where silica precipitation rates are slow.

$$K_D = \frac{(Ge/Si)_{solid}}{(Ge/Si)_{fluid}} \qquad (5)$$

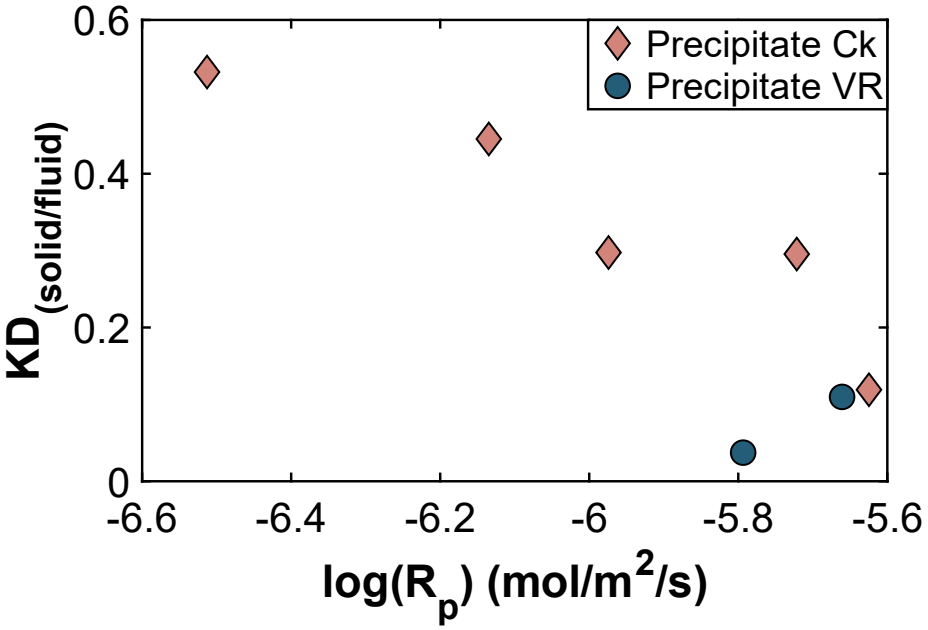

Figure 34: Apparent partition coefficients (K_D=(Ge/Si)$_{solid}$/(Ge/Si)$_{fluid}$) as a function of the silica precipitation rates determined in this study for the precipitated samples of the experiment at Ckoitchi (pink diamonds) and Vega Rinconada (blue circles).

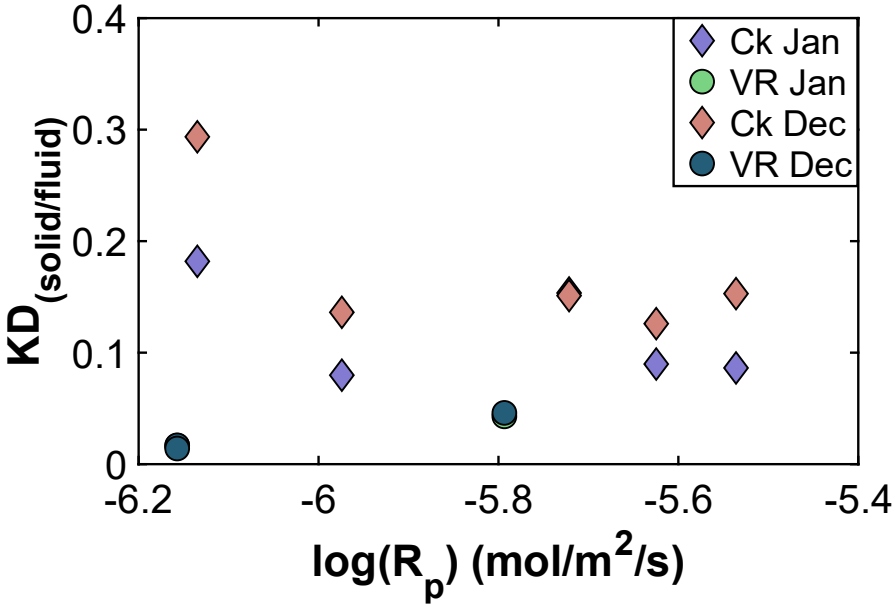

Figure 35: Apparent partition coefficients (K_D=(Ge/Si)$_{solid}$/(Ge/Si)$_{fluid}$) as a function of the silica precipitation rates determined in this study for the in-situ sinter deposit samples from Ckoitchi and Vega Rinconada. The diamonds correspond to the Ck samples, with the January samples indicated by purple and the December samples by pink. Red triangles denote the Ck Org. group samples. Vega Rinconada samples are depicted as circles, with January samples shown in green and December samples in blue.

Therefore, considering the study by Fernandez et al. (2021) and the results of this research, the competition between kinetic and thermodynamic factors controlling Ge partitioning in siliceous sinters can be summarized in Figure 36: Under equilibrium-controlled conditions (1), the partition coefficient is inversely proportional to silica precipitation rates, meaning the partition coefficient

increases as precipitation rates decrease. In this regime, the partitioning of Ge into the solid phase is feasible due to the slower precipitation rates and the fact that the silica concentration stabilizes over time. Ge/Si ratios of the solid phase are higher than Ge/Si ratios in the fluids. While, under kinetically controlled conditions (2), the partition coefficient decreases with temperature, meaning they are proportionally related, leading to very slow or almost negligible incorporation of Ge due to the rapid precipitation of silica. In this regime, the Ge/Si ratios in the fluids are higher than the Ge/Si ratios in the sinters.

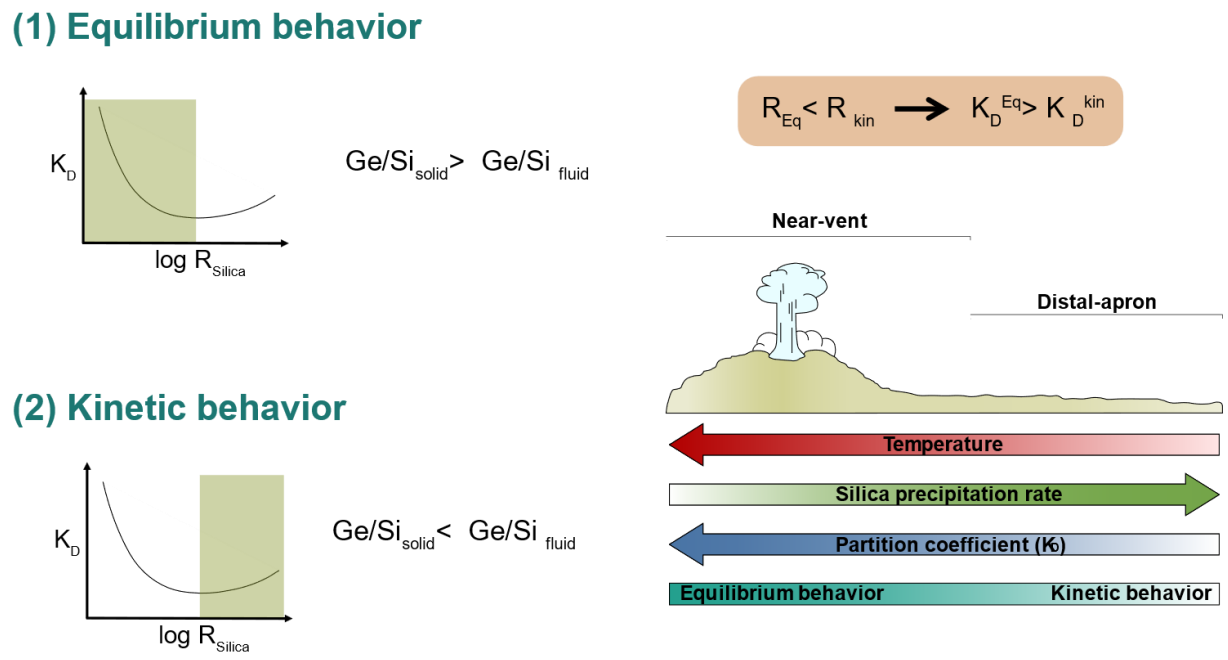

Figure 36: Competition between kinetic and thermodynamic factors controlling Ge partitioning in siliceous sinters. Under equilibrium behavior, precipitation rates are lower and higher partition coefficients are obtained, while under kinetic behavior, precipitation rates are faster and partition coefficients are lower.

4.4.3. The role of organic matter and sinter maturation in the partitioning of Ge into opal

In general terms, the Ge/Si ratios obtained in fluids, precipitates and in-situ deposits are higher in Ckoitchi than in Vega Rinconada. The studied vent at Ckoitchi is covered by microbial mats, whereas the vent at Vega Rinconada is bare and does not shows any macroscopic evidence of biological activity. Particularly, the fluids at Ckoitchi are more dilute due to its proximity to a local freshwater stream; plus the Ckoitchi vent is a perpetual spouter with a continuous flow of water, and thus, both features provide favorable conditions for the proliferation of organic matter, such as microcial mats (e.g., Damer & Deamer, 2020; Fox-Powell et al., 2018; Megevand et al., 2022). The organic rich samples obtained at Ckoitchi show the highest Ge/Si ratios (from 33.5 up to 81 µmol/mol) when compared to precipitates and active sinter samples at Ck and VR. So far we have established that a kinetic delay in the partitioning of Ge into opal is the main factor controlling Ge/Si ratios in the opal precipitates, implying that the highest Ge/Si ratios are observed at slow precipitation rates at high temperatures and closer to the vent. However, the high Ge/Si ratios in the organic samples, may be due to Ge having a higher affinity for complexation with organic

ligands when compared to Si (Dobrzyński et al., 2018; Pokrovski & Schott, 1998a). Moreover, Shen et al. (2011) suggest that Ge can bind to organic molecules that are attached to clay particles, forming Ge-organic complexes adsorbed on clays. Dong et al. (2015) speculate that this could result in higher Ge/Si ratios in clays. However, the effect of organic complexation of Ge at the clay surface remains to be tested, particularly, since clays already incorporate Ge into the tetrahedral clay site (Perez-Fodich & Derry, 2020).

To examine the effect of aging in Ge/Si ratios in the opal we compare the results obtained for three different groups: 1) samples from the precipitation experiment (labeled as precipitates); 2) samples collected from active in-situ sinter deposits; and 3) paleosinters. In this last group we also include paleosinter samples from El Tatio collected by Slagter et al. (2019), and Munoz-Saez et al. (2020), in addition to paleosinter samples from the Puchuldiza geothermal field (Sanchez-Yanez et al., 2017), and the Alpehue geysers (Pérez Nuñez, 2019) (Tables 13, 14 and 15). The comparison between the three groups shows that the ratios are higher in the precipitates, followed by the active sinters, and lower in the paleosinters (Figure 37), suggesting that sinter maturation and aging results in decreasing Ge/Si ratios. Opal maturation, which involves gradual changes from amorphous opal (opal-A), requires internal re-organization of the opal structure as it loses water, and becomes more stable (e.g., (Day & Jones, 2008; Herdianita et al., 2000b; Kastner & Gieskes, 1983; Liesegang et al., 2018; Liesegang & Tomaschek, 2020). Instead, opal recrystallization to more complex phases such as opal-C or quartz occurs in the later stages of diagenesis and involves morphological restructuring that might result in changes in the trace element composition of the solid (e.g., Cady & Farmer, 1996; Lynne et al., 2005; Lynne & Campbell, 2004). It is worth noting that all samples in this study correspond to opal-A, thus, the samples analyzed here did not undergo una recrystallization that could explain the decreasing Ge/Si ratios as a function of sample age. However, the depositional maturity of opal-A itself could explain these differences, considering that the X-ray diffraction patterns between the fossil and modern samples analyzed here vary in the degree of order/disorder of the silica crystal lattice. The paleosinter samples show more defined peaks along with a smoother pattern, reflecting a greater degree of homogeneity, while the modern samples exhibit more diffuse peaks and greater variability in counts. Another hypothesis for the decreasing Ge/Si ratios in the older sinter samples is leaching of Ge from the opal through fluid recirculation. Given the porous nature of sinters (Munoz-Saez et al., 2016), it is possible that the circulating fluids remobilize Ge, although there is no experimental data to corroborate this effect.

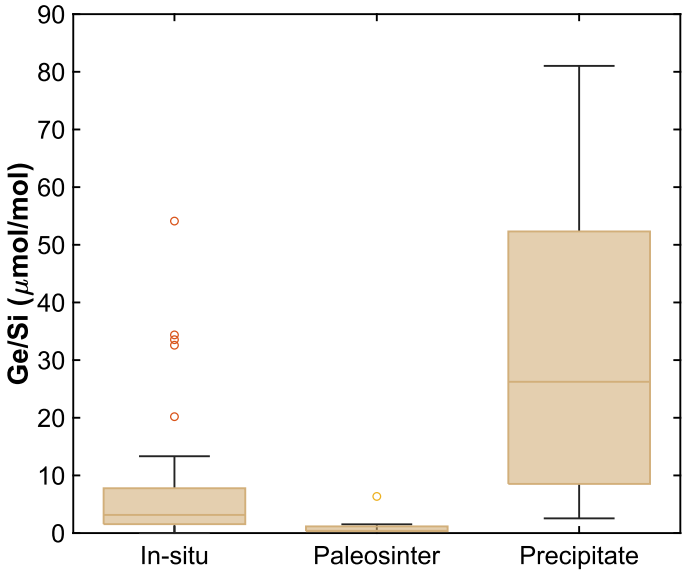

Figure 37: Comparison of Ge/Si ratios between samples from the precipitation experiment, in-situ sinter samples (from this work (Table 12 and 13), Slagter et al (2019) and Munoz-Saez (2020) (Table 13), and from Sanchez-Yanez et al (2017) and Perez Nuñez (2019) (TABLE 16)) and the paleosinter samples (from this work (Table 14), and from Slagter et al (2019) and Munoz-Saez (2020) (Table 15)).

CHAPTER 5: CONCLUSIONS

The variety of hot spring environments at El Tatio geothermal field with its extreme environmental conditions make it an ideal location to study the influence of silica precipitation dynamics on the fractionation of trace elements in siliceous sinters. This study has focused on two geothermal manifestations with contrasting hydrodynamics and abundance of microbial mats at El Tatio geothermal field: the first site Ckoitchi is a perpetual spouter covered by multi-colored microbial mats, while the second site Vega Rinconada corresponds to a geyser with no apparent surface microbial communities. These sites were selected with the purpose to investigate the partitioning of the Ge/Si ratio during opal precipitation. In each of these sites hydrothermal fluid and in-situ sinter deposits were collected along a thermal gradient downstream from the vent that conditions the type of depositional environment for silica precipitation. In addition, in-situ precipitation experiments were carried out in each of the sampling points, as well as an evaporation experiment in the Vega Rinconada area.

The hydrothermal fluids in El Tatio present Ge/Si ratios ranging between 68.52 and 110.98 μmol/mol among both sampling locations. The Ge/Si ratios in the fluids from Ckoitchi and Vega Rinconada, along with other hot springs in El Tatio, show typical ranges for neutral chloride-rich hydrothermal fluids. Particularly, the sampled fluids along the thermal gradient show that the Ge/Si fluid ratios decrease with decreasing temperatures downstream from vent, which is in agreement with previous studies, with a direct relationship between Ge/Si ratio in the fluid and temperature. The evaporation experiments show the silica readily precipitates as the fluid becomes supersaturated due to cooling and evaporation rates. However, Ge partitioning into the solid phase is minimal, with Ge/Si ratios increasing as silica is removed from solution. This behavior highlights the slow kinetics of Ge partitioning into silica precipitates, including amorphous silica, opal-A, or even quartz, as shown by previous studies. The silica precipitation experiments show that silica precipitation rates increase along the thermal gradient as the fluid cools downstream from the vent at both the geyser and perpetual spouter sites. Here, the Ge/Si ratios in the opal precipitates show an inverse trend as a function of bulk silica precipitation rates. This means that the highest Ge/Si ratios in the solids correspond to those point with the slowest precipitation rates (i.e., high temperature, closer to the vents). These results are consistent with numerical simulations and lab experimental data, in which Ge partitioning into the solids is favored at near equilibrium conditions, while fast kinetics retard its incoporation into the opal structure. Finally, the fossil sinters Ge/Si data at El Tatio shows a relationship with sample age, with the younger samples having higher Ge/Si ratios than the older ones. Additionally, as all fossil samples correspond to opal-A, it is possible to conclude that these are not necessarily linked to the degree of depositional maturity.

This study emphasizes that higher silica precipitation rates occurying at cooler fluid temperatures hinder the partitioning of Ge into the solid phase, while Ge behaves almost conservatively in the fluid phase. The findings show the slow incorporation of trace elements into siliceous sinters as the silica precipitation rate increases, aligning with previous laboratory experiment simulations. The study underscores the significant kinetic control in trace element partitioning into silica precipitates in hot spring environments. Therefore, the results presented here emphasize the potential of Ge and the Ge/Si ratio as a tracer of silica dynamics in hydrothermal systems. Studying Ge/Si ratios in siliceous sinters of hydrothermal systems may have an impact on

the knowledge of trace element partitioning in minerals formed in hydrothermal systems, and moreover, on the continental biogeochemical cycle of silica.

Future experimental silica precipitation and trace element partitioning studies should consider a longer precipitation time along with higher spatial resolution regarding precipitation rates. They should also include different hydrothermal manifestations with varying hydrodynamics and fluid compositions both in El Tatio, and other sites with surface geothermal activity.

BIBLIOGRAPHY

Aguirre, A. A., Derry, L. A., Mills, T. J., & Anderson, S. P. (2017). Colloidal transport in the Gordon Gulch catchment of the Boulder Creek CZO and its effect on C-Q relationships for silicon. *Water Resources Research*, *53*(3), 2368–2383. https://doi.org/10.1002/2016WR019730

Álvarez, P., Tunik, M., Giambiagi, L., & Rodríguez, C. (2023). Geología de las áreas Cupo-Toconce y Cerros de Tocorpuri, región de Antofagasta. *Servicio Nacional de Geología y Minería, Carta Geológica de Chile*.

Álvaro, J. J., Sánchez-Román, M., Nierop, K. G. J., & Peterse, F. (2021). Multiscale microbial preservation and biogeochemical signals in a modern hot-spring siliceous sinter rich in co2 emissions, Krýsuvík geothermal field, Iceland. *Minerals*, *11*(3), 1–31. https://doi.org/10.3390/min11030263

Arnórsson, S. (1984). *Germanium in Icelandic geothermal systems* (Vol. 48).

Ballou, E. V., Leban, M. I., & Wydeven, T. (1973). Solute Rejection by Porous Glass Membranes 111. Reduced Silica Dissolution and Prolonged Hyperfiltration Service with Feed Additivesa. In *J. appl. Chem. Biotechnol* (Vol. 23).

Barbieri, R., & Cavalazzi, B. (2014). How Do Modern Extreme Hydrothermal Environments Inform the Identification of Martian Habitability? The Case of the El Tatio Geyser Field. *Challenges*, *5*(2), 430–443. https://doi.org/10.3390/challe5020430

Barbieri, R., Cavalazzi, B., Stivaletta, N., & López-García, P. (2014). Silicified Biota in High-Altitude, Geothermally Influenced Ignimbrites at El Tatio Geyser Field, Andean Cordillera (Chile). *Geomicrobiology Journal*, *31*(6), 493–508. https://doi.org/10.1080/01490451.2013.836691

Bernstein, L. R. (1985). *Germanium geochemistry and mineralogy* (Vol. 49).

Bouchez, J., Gaillardet, J., France-Lanord, C., Maurice, L., & Dutra-Maia, P. (2011). Grain size control of river suspended sediment geochemistry: Clues from Amazon River depth profiles. *Geochemistry, Geophysics, Geosystems*, *12*(3). https://doi.org/10.1029/2010GC003380

Braunstein, D., & Lowe, D. R. (2001). Relationship between spring and geyser activity and the deposition and morphology of high temperature (>73°C) siliceous sinter, Yellowstone National Park, Wyoming, USA. In *JOURNAL OF SEDIMENTARY RESEARCH* (Vol. 71, Issue 5). http://pubs.geoscienceworld.org/sepm/jsedres/article-pdf/71/5/747/2816923/747.pdf

Cady, S. L., & Farmer, J. D. (1996). *Fossilization processes in siliceous thermal springs: trends in preservation along thermal gradients*.

Cady, S. L., Skok, J. R., Gulick, V. G., Berger, J. A., & Hinman, N. W. (2018). Siliceous Hot Spring Deposits: Why They Remain Key Astrobiological Targets. In *From Habitability to Life on Mars* (pp. 179–210). Elsevier. https://doi.org/10.1016/B978-0-12-809935-3.00007-4

Carroll, S., Mroczek, E., Alai, M., & Ebert, M. (1998). *Amorphous silica precipitation (60 to 120°C): Comparison of laboratory and field rates*.

Cornelis, J. T., Delvaux, B., Georg, R. B., Lucas, Y., Ranger, J., & Opfergelt, S. (2011). Tracing the origin of dissolved silicon transferred from various soil-plant systems towards rivers: A review. In *Biogeosciences* (Vol. 8, Issue 1, pp. 89–112). https://doi.org/10.5194/bg-8-89-2011

Cortecci, G., Boschetti, T., Mussi, M., Lameli, C. H., Mucchino, C., & Barbieri, M. (2005). New chemical and original isotopic data on waters from El Tatio geothermal field, northern Chile. In *Geochemical Journal* (Vol. 39).

Criaud, A., & Fouillac, C. (1986). Etude des eaux thermominkales carbogazeuses du Massif Central Francais. II. Comportement de quelques mbtaux en trace, de l'arsenic, de l'antimoine et du germahium. In *Geochmica ef Cosmochimica Acla* (Vol. 50).

Cusicanqui, H., Mahon, W. A. J., & Ellis, A. J. (1975). The geochemistry of the El Tatio geothermal field, Northern Chile. *Second United Nations Symposium on the Development and Utilization of Geothermal Resources, San Francisco, 1975*, 703.

Damer, B., & Deamer, D. (2020). The hot spring hypothesis for an origin of life. *Astrobiology*, *20*(4), 429–452. https://doi.org/10.1089/ast.2019.2045

Day, R., & Jones, B. (2008). Variations in water content in opal-A and opal-CT from geyser discharge aprons. *Journal of Sedimentary Research*, *78*(4), 301–315. https://doi.org/10.2110/jsr.2008.030

Demarest, M. S., Brzezinski, M. A., & Beucher, C. P. (2009). Fractionation of silicon isotopes during biogenic silica dissolution. *Geochimica et Cosmochimica Acta*, *73*(19), 5572–5583. https://doi.org/10.1016/j.gca.2009.06.019

Dobrzyński, D., Boguszewska-Czubara, A., & Sugimori, K. (2018). Hydrogeochemical and biomedical insights into germanium potential of curative waters: A case study of health resorts in the Sudetes mountains (Poland). *Environmental Geochemistry and Health*, *40*(4), 1335–1375. https://doi.org/10.1007/s10653-017-0061-0

Dong, L., Shen, B., Lee, C. T. A., Shu, X. J., Peng, Y., Sun, Y., Tang, Z., Rong, H., Lang, X., Ma, H., Yang, F., & Guo, W. (2015). Germanium/silicon of the Ediacaran-Cambrian Laobao cherts: Implications for the bedded chert formation and paleoenvironment interpretations. *Geochemistry, Geophysics, Geosystems*, *16*(3), 751–763. https://doi.org/10.1002/2014GC005595

Dove, P. M., Han, N., & De Yoreo, J. J. (2005). *Mechanisms of classical crystal growth theory explain quartz and silicate dissolution behavior Scheme 1. Scheme 2* (Vol. 25). www.pnas.orgcgidoi10.1073pnas.0507777102

Ellwood, M. J., Kelly, M., Maher, W. A., & De Deckker, P. (2006). Germanium incorporation into sponge spicules: Development of a proxy for reconstructing inorganic germanium and silicon concentrations in seawater. *Earth and Planetary Science Letters*, *243*(3–4), 749–759. https://doi.org/10.1016/j.epsl.2006.01.016

Evans, M. J., Deny, L. A., & France-Lanord, C. (2004). Geothermal fluxes of alkalinity in the Narayani river system of central Nepal. *Geochemistry, Geophysics, Geosystems*, *5*(8). https://doi.org/10.1029/2004GC000719

Evans, M. J., & Derry, L. A. (2002). Quartz control of high germanium/silicon ratios in geothermal waters. In *Geology* (Issue 11). www.geosociety.org/pubs/

Fernandez, N. M., Perez-Fodich, A., Derry, L. A., & Druhan, J. L. (2021). A first look at Ge/Si partitioning during amorphous silica precipitation: Implications for Ge/Si as a tracer of fluid-silicate interactions. *Geochimica et Cosmochimica Acta*, *297*, 158–178. https://doi.org/10.1016/j.gca.2021.01.007

Fernandez-Turiel, J. L., Garcia-Valles, M., Gimeno-Torrente, D., Saavedra-Alonso, J., & Martinez-Manent, S. (2005). The hot spring and geyser sinters of El Tatio, northern Chile. *Sedimentary Geology*, *180*(3–4), 125–147. https://doi.org/10.1016/j.sedgeo.2005.07.005

Filippelli, G. M., Carnahan, J. W., Derry, L. A., & Kurtz, A. (2000). Terrestrial paleorecords of Ge/Si cycling derived from lake diatoms. *Chemical Geology*, *168*(1–2), 9–26.

Fleming, B. A. (1986). *Kinetics of Reaction between Silicic Acid and Amorphous Silica Surfaces in NaCI Solutions*.

Flörke, O. W., Graetsch, H., Martin, B., Röller, K., & Wirth, R. (1991). Nomenclature of micro- and non-crystalline silica minerals, based on structure and microstructure. *Neues Jahrbuch Für Mineralogie. Abhandlungen*, *163*(1), 19–42.

Fournier, R. O., & Rowe, J. J. (1966). Estimation of underground temperatures from the silica content of water from hot springs and wet-steam wells. *American Journal of Science*, *264*(9), 685–697.

Fox-Powell, M. G., Channing, A., Applin, D., Cloutis, E., Preston, L. J., & Cousins, C. R. (2018). Cryogenic silicification of microorganisms in hydrothermal fluids. *Earth and Planetary Science Letters*, *498*, 1–8. https://doi.org/10.1016/j.epsl.2018.06.026

Froelich, P. N., Blanc, V., Mortlock, R. A., Chillrud, S. N., Dunstan, W., Udomkit, A., & Peng, T. (1992). River fluxes of dissolved silica to the ocean were higher during glacials: Ge/Si in diatoms, rivers, and oceans. *Paleoceanography*, *7*(6), 739–767.

Froelich, P. N., Hambrick, G. A., Andreae, M. O., Mortlock, R. A., & Edmond, J. M. (1985). The geochemistry of inorganic germanium in natural waters. *Journal of Geophysical Research: Oceans*, *90*(C1), 1133–1141.

Gallup, D. L. (1998). Aluminum silicate scale formation and inhibition (2): scale solubilities and laboratory and field inhibition tests. *Geothermics*, *27*(4), 485–501.

Garcia-Valles, M., Fernandez-Turiel, J. L., Gimeno-Torrente, D., Saavedra-Alonso, J., & Martinez-Manent, S. (2008). Mineralogical characterization of silica sinters from the El Tatio geothermal field, Chile. *American Mineralogist*, *93*(8–9), 1373–1383. https://doi.org/10.2138/am.2008.2583

Gaspard, F., Opfergelt, S., Dessert, C., Robert, V., Ameijeiras-Mariño, Y., & Delmelle, P. (2021a). Imprint of chemical weathering and hydrothermalism on the Ge/Si ratio and Si isotope composition of rivers in a volcanic tropical island, Basse-Terre, Guadeloupe (French West Indies). *Chemical Geology*, *577*. https://doi.org/10.1016/j.chemgeo.2021.120283

Gaspard, F., Opfergelt, S., Hirst, C., Hurwitz, S., McCleskey, R. B., Zahajská, P., Conley, D. J., & Delmelle, P. (2021b). Quantifying Non-Thermal Silicate Weathering Using Ge/Si and Si Isotopes in Rivers Draining the Yellowstone Plateau Volcanic Field, USA. *Geochemistry, Geophysics, Geosystems*, *22*(11). https://doi.org/10.1029/2021GC009904

Geilert, S., Vroon, P. Z., Roerdink, D. L., Van Cappellen, P., & van Bergen, M. J. (2014). Silicon isotope fractionation during abiotic silica precipitation at low temperatures: Inferences from flow-through experiments. *Geochimica et Cosmochimica Acta*, *142*(1), 95–114. https://doi.org/10.1016/j.gca.2014.07.003

Giggenbach, W. F. (1988). *Geothermal solute equilibria. Derivation of Na-K-Mg-Ca geoindicators* (Vol. 52).

Glennon, J. A., & Pfaff, R. M. (2003). *The Extraordinary Thermal Activity of El Tatio Geyser Field, Antofagasta Region, Chile*. https://www.researchgate.net/publication/284255246

Goldschimdt, V. H. (1970). Geochemistry (Geoquímica). *Alex Muir Oxford University*.

Goldschmidt, V. M. (1926). Über das krystallochemische und geochemische Verhalten des Germaniums. *Naturwissenschaften*, *14*(14), 295–297.

Gong, J., Munoz-Saez, C., Wilmeth, D. T., Myers, K. D., Homann, M., Arp, G., Skok, J. R., & van Zuilen, M. A. (2022). Morphogenesis of digitate structures in hot spring silica sinters of the El Tatio geothermal field, Chile. *Geobiology*, *20*(1), 137–155. https://doi.org/10.1111/gbi.12471

Guido, D., De Barrio, R., & Schalamuk, I. (2002). La Marciana Jurassic sinter—implications for exploration for epithermal precious-metal deposits in Deseado Massif, southern Patagonia, Argentina. *Applied Earth Science*, *111*(2), 106–113.

Guido, D. M., & Campbell, K. A. (2011). Jurassic hot spring deposits of the Deseado Massif (Patagonia, Argentina): Characteristics and controls on regional distribution. *Journal of Volcanology and Geothermal Research*, *203*(1–2), 35–47. https://doi.org/10.1016/j.jvolgeores.2011.04.001

Guidry, S. A., & Chafetz, H. S. (2002). Factors governing subaqueous siliceous sinter precipitation in hot springs: Examples from Yellowstone National Park, USA. *Sedimentology*, *49*(6), 1253–1267. https://doi.org/10.1046/j.1365-3091.2002.00494.x

Gunnarsson, I., & Arnorsson, S. (2000). *Amorphous silica solubility and the thermodynamic properties of H 4 SiO° 4 in the range of 0° to 350°C at P sat*.

Hamilton, A. R., Campbell, K. A., Rowland, J. V., Barker, S., & Guido, D. (2019). Characteristics and variations of sinters in the Coromandel Volcanic Zone: application to epithermal exploration. *New Zealand Journal of Geology and Geophysics*, *62*(4), 531–549. https://doi.org/10.1080/00288306.2018.1519514

Handley, K. M., & Campbell, K. A. (2011). Character, analysis, and preservation of biogenicity in terrestrial siliceous stromatolites from geothermal settings. *Stromatolites: Interaction of Microbes with Sediments*, 359–381.

Handley, K. M., Campbell, K. A., Mountain, B. W., & Browne, P. R. L. (2005). Abiotic-biotic controls on the origin and development of spicular sinter: in situ growth experiments, Champagne Pool, Waiotapu, New Zealand. In *Geobiology* (Vol. 3).

Herdianita, N. R., Browne, P. R. L., Rodgers, K. A., & Campbell, K. A. (2000a). Mineralogical and textural changes accompanying ageing of silica sinter. *Mineralium Deposita*, *35*(1), 48–62. https://doi.org/10.1007/s001260050005

Herdianita, N. R., Rodgers, K. A., & Browne, P. R. L. (2000b). *Routine instrumental procedures to characterise the mineralogy of modern and ancient silica sinters*.

Hurd, D. C. (1973). Interactions of biogenic opal, sediment and seawater in the Central Equatorial Pacific. *Geochimica et Cosmochimica Acta*, *37*(10), 2257–2282.

Hurwitz, S., & Manga, M. (2017). *The Fascinating and Complex Dynamics of Geyser Eruptions*. https://doi.org/10.1146/annurev-earth-063016

Icenhower, J. P., & Dove, P. M. (2000). *The dissolution kinetics of amorphous silica into sodium chloride solutions: Effects of temperature and ionic strength*.

Ichikuni, M. (1970). Incorporation of aluminum and iron into siliceous sinters. *Chemical Geology*, *6*, 273–279.

Ikeda, T. (2021). Bacterial biosilicification: a new insight into the global silicon cycle. *Bioscience, Biotechnology, and Biochemistry*, *85*(6), 1324–1331.

Iler, R. K. (1973). *Effect of Adsorbed Alumina on the Solubility of Amorphous Silica in Water*.

Iler, R. K. (1979). The chemistry of silica, Solubility, Polymerization. *Colloid and Surface Properties, and Biochemistry*, *866*.

Inagaki, F., Hayashi, S., Doi, K., Motomura, Y., Izawa, E., & Ogata, S. (1997). Microbial participation in the formation of siliceous deposits from geothermal water and analysis of the extremely thermophilic bacterial community. *FEMS Microbiology Ecology*, *24*(1), 41–48. https://doi.org/10.1111/j.1574-6941.1997.tb00421.x

Jochum, K. P., Schuessler, J. A., Wang, X. H., Stoll, B., Weis, U., Müller, W. E. G., Haug, G. H., Andreae, M. O., & Froelich, P. N. (2017). Whole-Ocean Changes in Silica and Ge/Si Ratios During the Last Deglacial Deduced From Long-Lived Giant Glass Sponges. *Geophysical Research Letters*, *44*(22), 11,555-11,564. https://doi.org/10.1002/2017GL073897

Jones, B., & Renaut, R. W. (2004). Water content of Opal-A: Implications for the origin of laminae in geyserite and sinter. In *JOURNAL OF SEDIMENTARY RESEARCH* (Vol. 74, Issue 1). SEPM (Society for Sedimentary Geology. http://pubs.geoscienceworld.org/sepm/jsedres/article-pdf/74/1/117/2818613/117.pdf

Jones, B., Renaut, R. W., & Rosen, M. R. (1999). Actively growing siliceous oncoids in the Waiotapu geothermal area, North Island, New Zealand. In *Journal of the Geological Society* (Vol. 156).

Jones, J. B., & Segnit, E. R. (1971). The nature of opal I. nomenclature and constituent phases. *Journal of the Geological Society of Australia*, *18*(1), 57–67. https://doi.org/10.1080/00167617108728743

Kastner, M., & Gieskes, J. M. (1983). Opal-A to opal-CT transformation: a kinetic study. In *Developments in Sedimentology* (Vol. 36, pp. 211–227). Elsevier.

Konhauser, K. O., Jones, B., Phoenix, V. R., Ferris, G., & Renaut, R. W. (2004). The microbial role in hot spring silicification. *Ambio*, *33*(8), 552–558. https://doi.org/10.1579/0044-7447-33.8.552

Konhauser, K. O., Phoenix, V. R., Bottrell, S. H., Adams, D. G., & Headà, I. M. (2001). *Microbial-silica interactions in Icelandic hot spring sinter: possible analogues for some Precambrian siliceous stromatolites*.

Krauskopf, K. B. (1956). *Dissolution and precipitation of silica at low temperatures* (Vol. 10).

Kraynov, S. R. (1967). Geochemistry of germanium in the thermal carbonate waters (illustrated by examples from the Pamirs and Greater Caucasus). *Geochem Int*, *4*, 309–320.

Kroger, N., Lorenz, S., Brunner, E., & Sumper, M. (2002). Self-assembly of highly phosphorylated silaffins and their function in biosilica morphogenesis. *Science*, *298*(5593), 584–586.

Kumar, S., Soukup, M., & Elbaum, R. (2017). Silicification in grasses: Variation between different cell types. In *Frontiers in Plant Science* (Vol. 8). Frontiers Research Foundation. https://doi.org/10.3389/fpls.2017.00438

Kurtz, A. C., Derry, L. A., & Chadwick, O. A. (2002). *Germanium-silicon fractionation in the weathering environment*.

Kyle, J. E., Schroeder, P. A., & Wiegel, J. (2007). Microbial silicification in sinters from two terrestrial hot springs in the Uzon Caldera, Kamchatka, Russia. *Geomicrobiology Journal*, *24*(7–8), 627–641. https://doi.org/10.1080/01490450701672158

Lahsen, A. (1978). Evaluación de los resultados de la exploración del campo geotérmico de Puchuldiza I Región Tarapacá. *Informe Inédito Para Comité Para El Aprovechamiento de La Energía Geotérmica, CORFO*.

Lahsen, A., & Trujillo, P. (1976). The geothermal field of El Tatio, Chile. *Proceeding, Second United Nations Symposium on the Development and Use of Geothermal Resources, San Francisco*, *1*, 170–177.

Lee, S., Xu, H., & Xu, H. (2022). Reexamination of the structure of opal-A: A combined study of synchrotron X-ray diffraction and pair distribution function analysis. *American Mineralogist*, *107*(7), 1353–1360. https://doi.org/10.2138/am-2022-8017

Lewin, J. C. (1961). The dissolution of silica from diatom walls. *Geochimica et Cosmochimica Acta*, *21*(3–4), 182–198.

Liesegang, M., Milke, R., & Berthold, C. (2018). Amorphous silica maturation in chemically weathered clastic sediments. *Sedimentary Geology*, *365*, 54–61. https://doi.org/10.1016/j.sedgeo.2018.01.001

Liesegang, M., & Tomaschek, F. (2020). Tracing the continental diagenetic loop of the opal-A to opal-CT transformation with X-ray diffraction. *Sedimentary Geology*, *398*. https://doi.org/10.1016/j.sedgeo.2020.105603

Liu, D., Tian, Q., Li, M., Mi, M., Yuan, P., Yu, R., Zhou, J., Du, P., Wei, H., Guo, H., & Deng, L. (2024). Coupled Si–Al Biogeochemistry: Occurrence of Aluminum in Diatom-Derived Biogenic Silica. *Journal of Geophysical Research: Biogeosciences*, *129*(1). https://doi.org/10.1029/2023jg007467

Lorens, R. B. (1981). Sr, Cd, Mn and Co distribution coefficients in calcite as a function of calcite precipitation rate. *Geochimica et Cosmochimica Acta*, *45*(4), 553–561.

Lowe, D. R., & Braunstein, D. (2003). Microstructure of high-temperature (>73 °C) siliceous sinter deposited around hot springs and geysers, Yellowstone National Park: The role of biological and abiological processes in sedimentation. *Canadian Journal of Earth Sciences*, *40*(11), 1611–1642. https://doi.org/10.1139/e03-066

Lucchi, F., Tranne, C. A., Rossi, P. L., Gallardo, C., De Astis, G., & Pini, G. A. (2009). *Volcanic and tectonic history of El Tatio area (central Andes, northern Chile): explanatory notes to the 1:50000 scale geological map*. https://www.researchgate.net/publication/48330178

Lynne, B. Y. (2012). Mapping vent to distal-apron hot spring paleo-flow pathways using siliceous sinter architecture. *Geothermics*, *43*, 3–24. https://doi.org/10.1016/j.geothermics.2012.01.004

Lynne, B. Y., & Campbell, K. A. (2003). Diagenetic transformations (opal-A to quartz) of low- and mid-temperature microbial textures in siliceous hot-spring deposits, Taupo Volcanic Zone, New Zealand. *Canadian Journal of Earth Sciences*, *40*(11), 1679–1696. https://doi.org/10.1139/e03-064

Lynne, B. Y., & Campbell, K. A. (2004). Morphologic and mineralogic transitions from opal-A to opal-CT in low-temperature siliceous sinter diagenesis, Taupo Volcanic Zone, New Zealand. *Journal of Sedimentary Research*, *74*(4), 561–579.

Lynne, B. Y., Campbell, K. A., James, B. J., Browne, P. R. J., & Moore, J. (2007). Tracking crystallinity in siliceous hot-spring deposits. *American Journal of Science*, *307*(3), 612–641. https://doi.org/10.2475/03.2007.03

Lynne, B. Y., Campbell, K. A., Moore, J. N., & Browne, P. R. L. (2005). Diagenesis of 1900-year-old siliceous sinter (opal-A to quartz) at Opal Mound, Roosevelt Hot Springs, Utah, U.S.A. *Sedimentary Geology*, *179*(3–4), 249–278. https://doi.org/10.1016/j.sedgeo.2005.05.012

Maher, K., Steefel, C. I., White, A. F., & Stonestrom, D. A. (2009). The role of reaction affinity and secondary minerals in regulating chemical weathering rates at the Santa Cruz Soil Chronosequence, California. *Geochimica et Cosmochimica Acta*, *73*(10), 2804–2831. https://doi.org/10.1016/j.gca.2009.01.030

Megevand, V., Carrizo, D., Lezcano, M. Á., Moreno-Paz, M., Cabrol, N. A., Parro, V., & Sánchez-García, L. (2022). Lipid Profiles From Fresh Biofilms Along a Temperature Gradient on a Hydrothermal Stream at El Tatio (Chilean Andes), as a Proxy for the Interpretation of Past

and Present Biomarkers Beyond Earth. *Frontiers in Microbiology*, *13*. https://doi.org/10.3389/fmicb.2022.811904

Moore, D. M., & Reynolds Jr, R. C. (1997). *X-ray Diffraction and the Identification and Analysis of Clay Minerals.* Oxford University Press (OUP).

Mortlock, R. A., & Froelich, P. N. (1987). Continental weathering of germanium: GeSi in the global river discharge. *Geochimica et Cosmochimica Acta*, *51*(8), 2075–2082.

Mortlock, R. A., Froelich, P. N., Feely, R. A., Massoth, G. J., Butterfield, D. A., & Lupton, J. E. (1993). Silica and germanium in Pacific Ocean vents and plumes hydrothermal. In *Earth and Planetary Science Letters* (Vol. 119).

Mortlock, R. A., & Froelich, Philip. N. (1996). Determination of germanium by isotope dilution-hydride generation inductively coupled plasma mass spectrometry. *Chimica Acta*, *332*, 277–284.

Mountain, B. W., Benning, L. G., & Boerema, J. A. (2003). Experimental studies on New Zealand hot spring sinters: Rates of growth and textural development. *Canadian Journal of Earth Sciences*, *40*(11), 1643–1667. https://doi.org/10.1139/e03-068

Müller, W. E. G., Krasko, A., Pennec, G. Le, Steffen, R., Wiens, M., Ammar, M. S. A., Müller, I. M., & Schröder, H. C. (2003). Molecular mechanism of spicule formation in the demosponge Suberites domuncula: silicatein-collagen-myotrophin. *Silicon Biomineralization: Biology—Biochemistry—Molecular Biology—Biotechnology*, 195–221.

Munoz-Saez, C. (2022). Geyserite Data El Tatio. In *Mendeley Data*. https://doi.org/DOI: 10.17632/bg8ycnngd2.1

Munoz-Saez, C., Gong, J., Perez-Fodich, A., & van Zuilen, M. A. (2023). Environmental and Hydrogeochemical Controls of Spicular Geyserite in Opaline Hot Spring Deposits. *Earth and Space Science*, *10*(3). https://doi.org/10.1029/2022EA002645

Munoz-Saez, C., Manga, M., & Hurwitz, S. (2018). Hydrothermal discharge from the El Tatio basin, Atacama, Chile. *Journal of Volcanology and Geothermal Research*, *361*, 25–35. https://doi.org/10.1016/j.jvolgeores.2018.07.007

Munoz-Saez, C., Manga, M., Hurwitz, S., Slagter, S., Churchill, D. M., Reich, M., Damby, D., & Morata, D. (2020). Radiocarbon Dating of Silica Sinter and Postglacial Hydrothermal Activity in the El Tatio Geyser Field. *Geophysical Research Letters*, *47*(11). https://doi.org/10.1029/2020GL087908

Munoz-Saez, C., Namiki, A., & Manga, M. (2015). Geyser eruption intervals and interactions: Examples from El Tatio, Atacama, Chile. *Journal of Geophysical Research: Solid Earth*, *120*(11), 7490–7507. https://doi.org/10.1002/2015JB012364

Munoz-Saez, C., Saltiel, S., Manga, M., Nguyen, C., & Gonnermann, H. (2016). Physical and hydraulic properties of modern sinter deposits: El Tatio, Atacama. *Journal of Volcanology and Geothermal Research*, *325*, 156–168. https://doi.org/10.1016/j.jvolgeores.2016.06.026

Nicolau, C., Reich, M., & Lynne, B. (2014). Physico-chemical and environmental controls on siliceous sinter formation at the high-altitude El Tatio geothermal field, Chile. *Journal of Volcanology and Geothermal Research*, *282*, 60–76. https://doi.org/10.1016/j.jvolgeores.2014.06.012

Nicolau del Roure Eylerts, C. B. (2013). *Physico-chemical and environmental controls on siliceous sinter formation at the high-altitude el Tatio geothermal field, northern Chile*.

Orange, F., Lalonde, S. V., & Konhauser, K. O. (2013). Experimental simulation of evaporation-driven silica sinter formation and microbial silicification in hot spring systems. *Astrobiology*, *13*(2), 163–176. https://doi.org/10.1089/ast.2012.0887

Parker, R. J., & Nicholson, K. (1990). Arsenic in geothermal sinters: determination and implications for mineral exploration. *12th NZ Geothermal Workshop, Auckland University, Auckland*, 35–39.

Peng, X., & Jones, B. (2012). Rapid precipitation of silica (opal-A) disguises evidence of biogenicity in high-temperature geothermal deposits: Case study from Dagunguo hot spring, China. *Sedimentary Geology*, *257–260*, 45–62. https://doi.org/10.1016/j.sedgeo.2012.01.013

Pérez Nuñez, C. (2019). *Estudio del ambiente de formación de sínteres silíceos en los géiseres de Alpehue, volcán Sollipulli, Sur de Chile.* https://repositorio.uchile.cl/handle/2250/173810

Perez-Fodich, A., & Derry, L. A. (2020). A model for germanium-silicon equilibrium fractionation in kaolinite. *Geochimica et Cosmochimica Acta*, *288*, 199–213. https://doi.org/10.1016/j.gca.2020.07.046

Phoenix, V. R., Bennett, P. C., Engel, A. S., Tyler, S. W., & Ferris, F. G. (2006). Chilean high-altitude hot-spring sinters: A model system for UV screening mechanisms by early Precambrian cyanobacteria. *Geobiology*, *4*(1), 15–28. https://doi.org/10.1111/j.1472-4669.2006.00063.x

Piper, A. M. (1944). A graphic procedure in the geochemical interpretation of water-analyses. *Eos, Transactions American Geophysical Union*, *25*(6), 914–928. https://doi.org/10.1029/TR025i006p00914

Pokrovski, G. S., Roux, J., Hazemann, J. L., & Testemale, D. (2005). An X-ray absorption spectroscopy study of argutite solubility and aqueous Ge(IV) speciation in hydrothermal fluids to 500 °C and 400 bar. *Chemical Geology*, *217*(1–2), 127–145. https://doi.org/10.1016/j.chemgeo.2005.01.006

Pokrovski, G. S., & Schott, J. (1998a). *Experimental study of the complexation of silicon and germanium with aqueous organic species: Implications for germanium and silicon transport and Ge/Si ratio in natural waters*.

Pokrovski, G. S., & Schott, J. (1998b). *Thermodynamic properties of aqueous Ge(IV) hydroxide complexes from 25 to 350°C: Implications for the behavior of germanium and the Ge/Si ratio in hydrothermal fluids*.

Pope, J. G., Brown, K. L., & McConchie, D. M. (2005). Gold concentrations in springs at Waiotapu, New Zealand: implications for precious metal deposition in geothermal systems. *Economic Geology*, *100*(4), 677–687.

Raven, J. A. (1983). The transport and function of silicon in plants. *Biological Reviews*, *58*(2), 179–207.

Rimstidt, J. D., & Barnes, H. L. (1980). The kinetics of silica-water reactions. *Geochimica et Cosmochimica Acta*, *44*(11), 1683–1699.

Rimstidt, J. D., & Cole, D. R. (1983). Geothermal mineralization; I, The mechanism of formation of the Beowawe, Nevada, siliceous sinter deposit. *American Journal of Science*, *283*(8), 861–875.

Rodgers, K. A., Cook, K. L., Browne, P. R. L., & Campbell, K. A. (2002). The mineralogy, texture and significance of silica derived from alteration by steam condensate in three New Zealand geothermal fields. *Clay Minerals*, *37*(2), 299–322. https://doi.org/10.1180/0009855023720035

Rothbaum, H. P., Anderton, B. H., Harrison, R. F., Rohde, A. G., & Slatter, A. (1979). Effect of silica polymerisation and pH on geothermal scaling. *Geothermics*, *8*(1), 1–20.

Ruff, S. W., Campbell, K. A., Van Kranendonk, M. J., Rice, M. S., & Farmer, J. D. (2020). The case for ancient hot springs in gusev crater, mars. *Astrobiology*, *20*(4), 475–499. https://doi.org/10.1089/ast.2019.2044

Ruff, S. W., & Farmer, J. D. (2016). Silica deposits on Mars with features resembling hot spring biosignatures at El Tatio in Chile. *Nature Communications*, *7*. https://doi.org/10.1038/ncomms13554

Salisbury, M. J., Jicha, B. R., de Silva, S. L., Singer, B. S., Jiménez, N. C., & Ort, M. H. (2011). 40Ar/39Ar chronostratigraphy of Altiplano-Puna volcanic complex ignimbrites reveals the development of a major magmatic province. *Bulletin of the Geological Society of America*, *123*(5), 821–840. https://doi.org/10.1130/B30280.1

Sanchez-Garcia, L., Fernandez-Martinez, M. A., García-Villadangos, M., Blanco, Y., Cady, S. L., Hinman, N., Bowden, M. E., Pointing, S. B., Lee, K. C., Warren-Rhodes, K., Lacap-Bugler, D., Cabrol, N. A., Parro, V., & Carrizo, D. (2019). Microbial biomarker transition in high-altitude sinter mounds from El Tatio(Chile) through different stages of hydrothermal activity. *Frontiers in Microbiology*, *10*(JAN). https://doi.org/10.3389/fmicb.2018.03350

Sanchez-Yanez, C., Reich, M., Leisen, M., Morata, D., & Barra, F. (2017). Geochemistry of metals and metalloids in siliceous sinter deposits: Implications for elemental partitioning into silica phases. *Applied Geochemistry*, *80*, 112–133. https://doi.org/10.1016/j.apgeochem.2017.03.008

Saunders, J. A. (1990). Colloidal transport of gold and silica in epithermal precious-metal systems: Evidence from the Sleeper deposit, Nevada. *Geology*, *18*(8), 757–760.

Scott, S., Galeczka, I. M., Gunnarsson, I., Arnórsson, S., & Stefánsson, A. (2024). Silica polymerization and nanocolloid nucleation and growth kinetics in aqueous solutions. *Geochimica et Cosmochimica Acta*, *371*, 78–94. https://doi.org/10.1016/j.gca.2024.02.017

Setiawan, F. A., Rahayuningsih, E., Petrus, H. T. B. M., Nurpratama, M. I., & Perdana, I. (2019). Kinetics of silica precipitation in geothermal brine with seeds addition: minimizing silica scaling in a cold re-injection system. *Geothermal Energy*, *7*(1). https://doi.org/10.1186/s40517-019-0138-3

Shannon, W. T., Owers, W. R., & Rothbaumt, H. P. (1982). *Pilot scale solids/liquid separation in hot geothermal discharge waters using dissolved air flotation.* (Vol. 1, Issue 1).

Shen, B., Lee, C. T. A., & Xiao, S. (2011). Germanium/silica ratios in diagenetic chert nodules from the Ediacaran Doushantuo Formation, South China. *Chemical Geology*, *280*(3–4), 323–335. https://doi.org/10.1016/j.chemgeo.2010.11.019

Sillitoe, R. H. (2015). Epithermal paleosurfaces. *Mineralium Deposita*, *50*(7), 767–793. https://doi.org/10.1007/s00126-015-0614-z

Slagter, S. (2019). *Silica Sinter formation at the El Tatio Geyser field, chilean Altiplano: Insights from radiocarbon dating*. https://repositorio.uchile.cl/handle/2250/170517

Slagter, S., Reich, M., Munoz-Saez, C., Southon, J., Morata, D., Barra, F., Gong, J., & Skok, J. R. (2019). Environmental controls on silica sinter formation revealed by radiocarbon dating. *Geology*, *47*(4), 330–334. https://doi.org/10.1130/G45859.1

Smith, D. K. (1998). *Opal, cristobalite, and tridymite: Noncrystallinity versus crystallinity, nomenclature of the silica minerals and bibliography*.

Spinthaki, A., Kamaratou, M., Matheis, J., Disci, D., Hater, W., & Demadis, K. D. (2021). The precipitation of "aluminum silicate" under geothermal stresses: Identifying its idiosyncrasies. *Geothermics*, *92*. https://doi.org/10.1016/j.geothermics.2021.102060

Squyres, S. W., Arvidson, R. E., Ruff, S., Gellert, R., Morris, R. V, Ming, D. W., Crumpler, L., Farmer, J. D., Marais, D. J. Des, & Yen, A. (2008). Detection of silica-rich deposits on Mars. *Science*, *320*(5879), 1063–1067.

Sun, V. Z., & Milliken, R. E. (2015). Ancient and recent clay formation on Mars as revealed from a global survey of hydrous minerals in crater central peaks. *Journal of Geophysical Research: Planets*, *120*(12), 2293–2332. https://doi.org/10.1002/2015JE004918

Sun, V. Z., & Milliken, R. E. (2018). Distinct Geologic Settings of Opal-A and More Crystalline Hydrated Silica on Mars. *Geophysical Research Letters*, *45*(19), 10,221-10,228. https://doi.org/10.1029/2018GL078494

Tassi, F., Martinez, C., Vaselli, O., Capaccioni, B., & Viramonte, J. (2005). Light hydrocarbons as redox and temperature indicators in the geothermal field of El Tatio (northern Chile). *Applied Geochemistry*, *20*(11), 2049–2062. https://doi.org/10.1016/j.apgeochem.2005.07.013

Tatzel, M., Von Blanckenburg, F., Oelze, M., Bouchez, J., & Hippler, D. (2017). Late Neoproterozoic seawater oxygenation by siliceous sponges. *Nature Communications*, *8*(1). https://doi.org/10.1038/s41467-017-00586-5

Tobler, D. J., Shaw, S., & Benning, L. G. (2009). Quantification of initial steps of nucleation and growth of silica nanoparticles: An in-situ SAXS and DLS study. *Geochimica et Cosmochimica Acta*, *73*(18), 5377–5393. https://doi.org/10.1016/j.gca.2009.06.002

Tobler, D. J., Stefánsson, A., & Benning, L. G. (2008). In-situ grown silica sinters in Icelandic geothermal areas. *Geobiology*, *6*(5), 481–502. https://doi.org/10.1111/j.1472-4669.2008.00179.x

Trujillo, P. (1970). Manifestaciones termales de Puchuldiza y Tuja. *Informe Inédito Para Comité Geotérmico, CORFO*.

van den Heuvel, D. B., Gunnlaugsson, E., & Benning, L. G. (2020). Surface roughness affects early stages of silica scale formation more strongly than chemical and structural properties of the substrate. *Geothermics*, *87*. https://doi.org/10.1016/j.geothermics.2020.101835

Walter, M. R. (1976). Geyserites of Yellowstone National Park: an example of abiogenic "stromatolites." In *Developments in sedimentology* (Vol. 20, pp. 87–112). Elsevier.

Weed, W. H. (1889). *The vegetation of hot springs*.

Weres, O., Yee, A., & Tsao, L. (1981). Kinetics of silica polymerization. *Journal of Colloid and Interface Science*, *84*(2), 379–402.

White, A. F., & Brantley, S. L. (2003). The effect of time on the weathering of silicate minerals: Why do weathering rates differ in the laboratory and field? *Chemical Geology*, *202*(3–4), 479–506. https://doi.org/10.1016/j.chemgeo.2003.03.001

White, A. F., Schulz, M. S., Vivit, D. V., Blum, A. E., Stonestrom, D. A., & Anderson, S. P. (2008). Chemical weathering of a marine terrace chronosequence, Santa Cruz, California I: Interpreting rates and controls based on soil concentration-depth profiles. *Geochimica et Cosmochimica Acta*, *72*(1), 36–68. https://doi.org/10.1016/j.gca.2007.08.029

White, D. E., Rrannock, W. W., & Murata, K. J. (1956). *Silica in hot-spring water** (Vol. 10). Pcrgamon Preaa Ltd.

Wilmeth, D. T., Nabhan, S., Myers, K. D., Slagter, S., Lalonde, S. V., Sansjofre, P., Homann, M., Konhauser, K. O., Munoz-Saez, C., & van Zuilen, M. A. (2020). Depositional evolution of an extinct sinter mound from source to outflow, El Tatio, Chile. *Sedimentary Geology*, *406*. https://doi.org/10.1016/j.sedgeo.2020.105726

Yokoyama, T., Sato, Y., Maeda, Y., Tarutani, T., & Itoi, R. (1993). Siliceous deposits formed from geothermal water I. The major constituents and the existing states of iron and aluminium. *Geochemical Journal*, *27*(6), 375–384.

ANNEXES

ANNEX A

Alkaline extraction method for opal (from Mortlock & Fröelich, 1996)

Prior to germanium analysis, the samples must be treated to improve the detection of the trace element. The steps performed for the alkaline extraction method for opal (adapted from Mortlock & Fröelich, 1996) are detailed below.

- ~25 mg of crushed (not powdered) sample is required (target SiO_2 concentration <100 ppm).
- Weigh pre-labeled centrifuge tubes.
- Transfer the samples to the tubes, reaching the required target, keeping a record of the weight.
- Add 5 mL of 30% H_2O_2 and weigh again.
- Leave to stand for 30 minutes, then weigh.
- Add 5 mL of 1N HNO_3, and weigh.
- Cap and sonify the tube for 30 min to let carbonates and organic matter react. Then dry, uncover to release gas, close the lid again and weigh.
- Add 20 mL of DI H_2O 18.2 Ω, and weigh.
- Centrifuge at 4000 rpm for 6 minutes (acc 6 and decel 5).
- Decant and remove the supernatant. Weigh the remaining solution.

Some steps are repeated:

- Add 5 mL of 30% H_2O_2 and weigh again.
- Leave to stand for 30 minutes, then weigh.
- Add 5 mL of 1N HNO_3, and weigh.
- Cap and sonify the tube for 30 min to let carbonates and organic matter react. Then dry, uncover to release gas, close the lid again and weigh.
- Add 20 mL of DI H_2O 18.2 Ω, and weigh.
- Centrifuge at 4000 rpm for 6 minutes (acc 6 and decel 5).
- Weigh 250 mL bottles, with the respective label on the cap.
- After centrifugation, the supernatant is removed and weighed (~1 mL volume is left)
- Transfer the precipitate to 250 mL bottles and weigh

- The tube is rinsed to a volume of 5 mL (with DI water, 2-3 times until the volume is reached)
- Transfer the rinsate to the 250 mL and weigh.
- Add 250 mL of 2M Na_2CO_3 solution to the bottle, and weigh.
- Leave in the thermoregulated bath at 85°C during the day and 80°C at night for 10 days, leaving half-open to prevent bursting. Shake the bottles twice a day during this period
- After 10 days, remove the samples from the bath, dry, allow to cool, and weigh.
- Weigh 50 mL tubes for transferring samples, 2 tubes per sample should be considered, each tube is weighed, labeled, and capped.
- Transfer 20 mL per sample (10 mL per tube, i.e. two tubes with 10 mL of sample), weigh each tube.
- Neutralize the samples with 2.5 mL of 65% HNO_3. Allow to stand and weigh.

ANNEX B

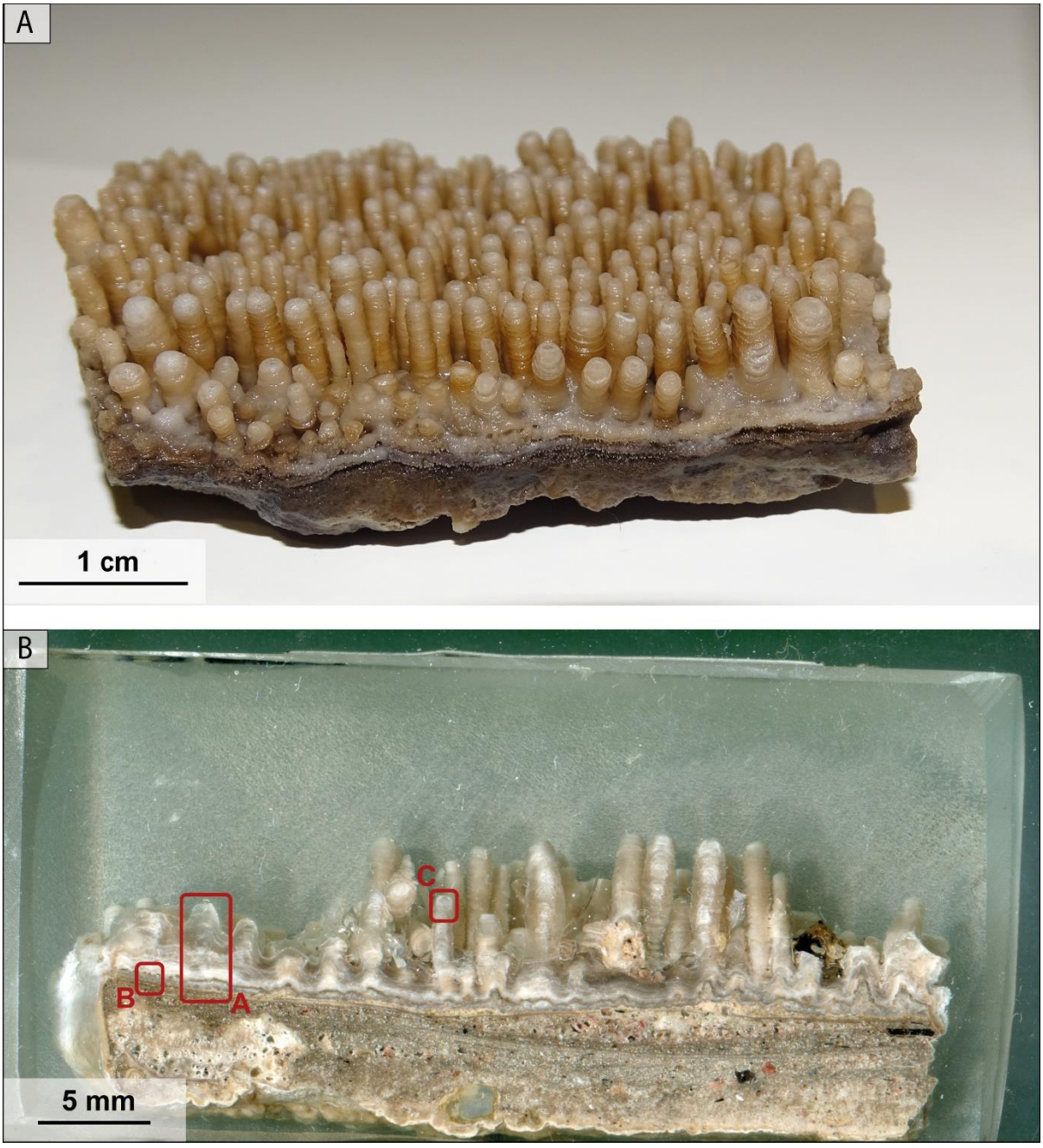

Figure 38: Two views of the in-situ sinter deposit sample from point VR01 at Vega Rinconada denoted ET01-VR01(A) Hand sample, geyserites of different sizes formed in the Vega Rinconada vent are observed. The spicules are finely laminated. (B) Polished cross-section of the sample in (A), shows the bedrock at the bottom, and the overlying sinter deposit, initially with laminations and subsequent formation of the geyserites. The red boxes A, B, and C are presented in the figure below.

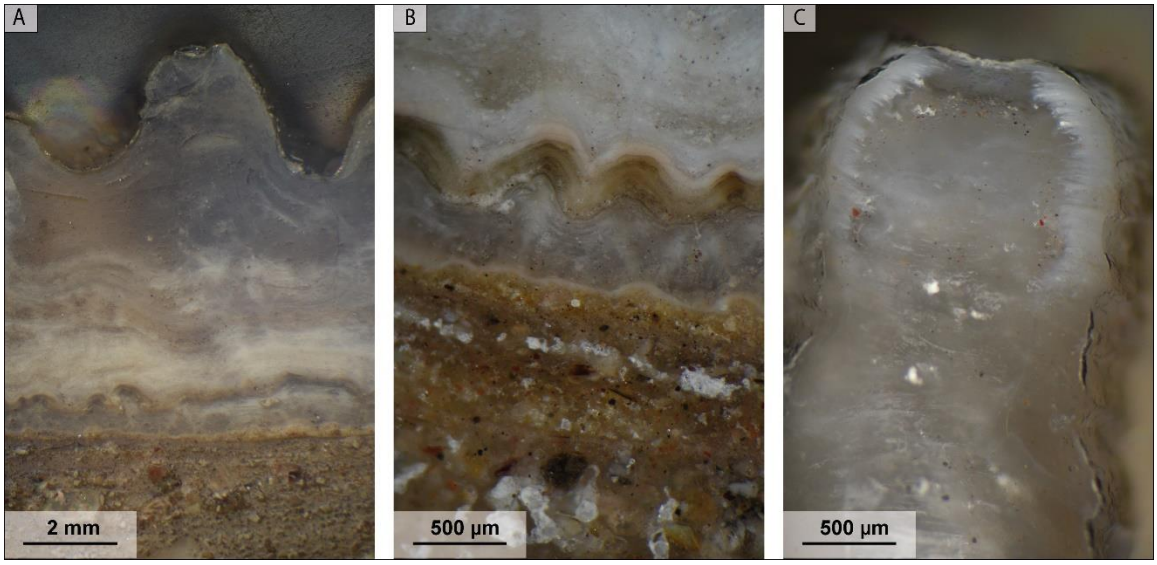

Figure 39: Photographs of sample ET02-VR01 from optical microscopy. A, B and C are the respective insets in Figure 38 (above). (A) Image of a spicule, in the lower zone visualizes the bedrock, with thin laminations deposited on it. (B) Closer view of the sinter laminations, which would indicate different depositional events, at that scale, they are small geyserites that were covered by opal precipitation. (C) Close-up of a spicule, at the edges it is possible to recognize small laminations, in addition to the presence of detritus trapped during silica precipitation.

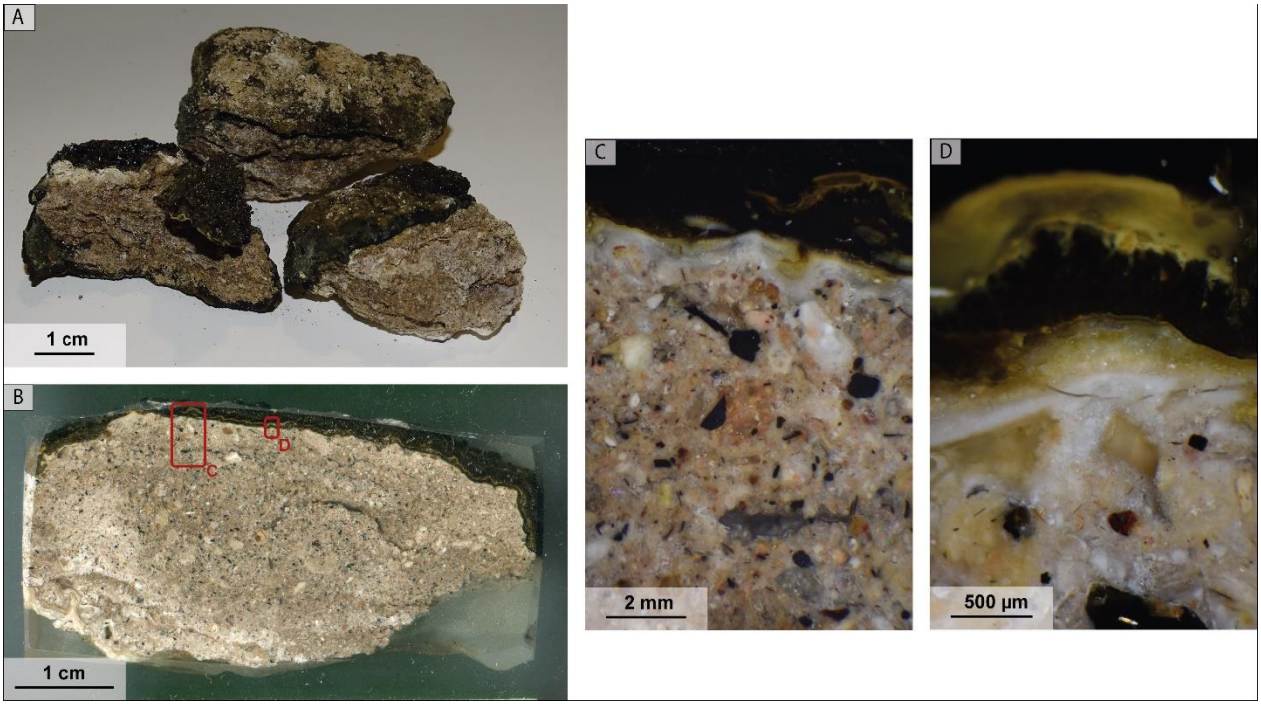

Figure 40: Different views of sample ET03-Co01 of in-situ sinter deposit, belonging to point Co01 at Ckoitchi. (A) Sinter hand samples. (B) Polished cross section of the larger sample in (A), mostly corresponds to silica-cemented bedrock. (C) Close-up of the bedrock-sinter deposit boundary, at the top the sinter deposit can be distinguished, with thin whitish laminations, being covered by a yellowish-blackish layer of biological material (from the bacterial mat). (D) Close-up of the sinter deposit, showing that the whitish layers fill the bedrock material, recementing the rock.

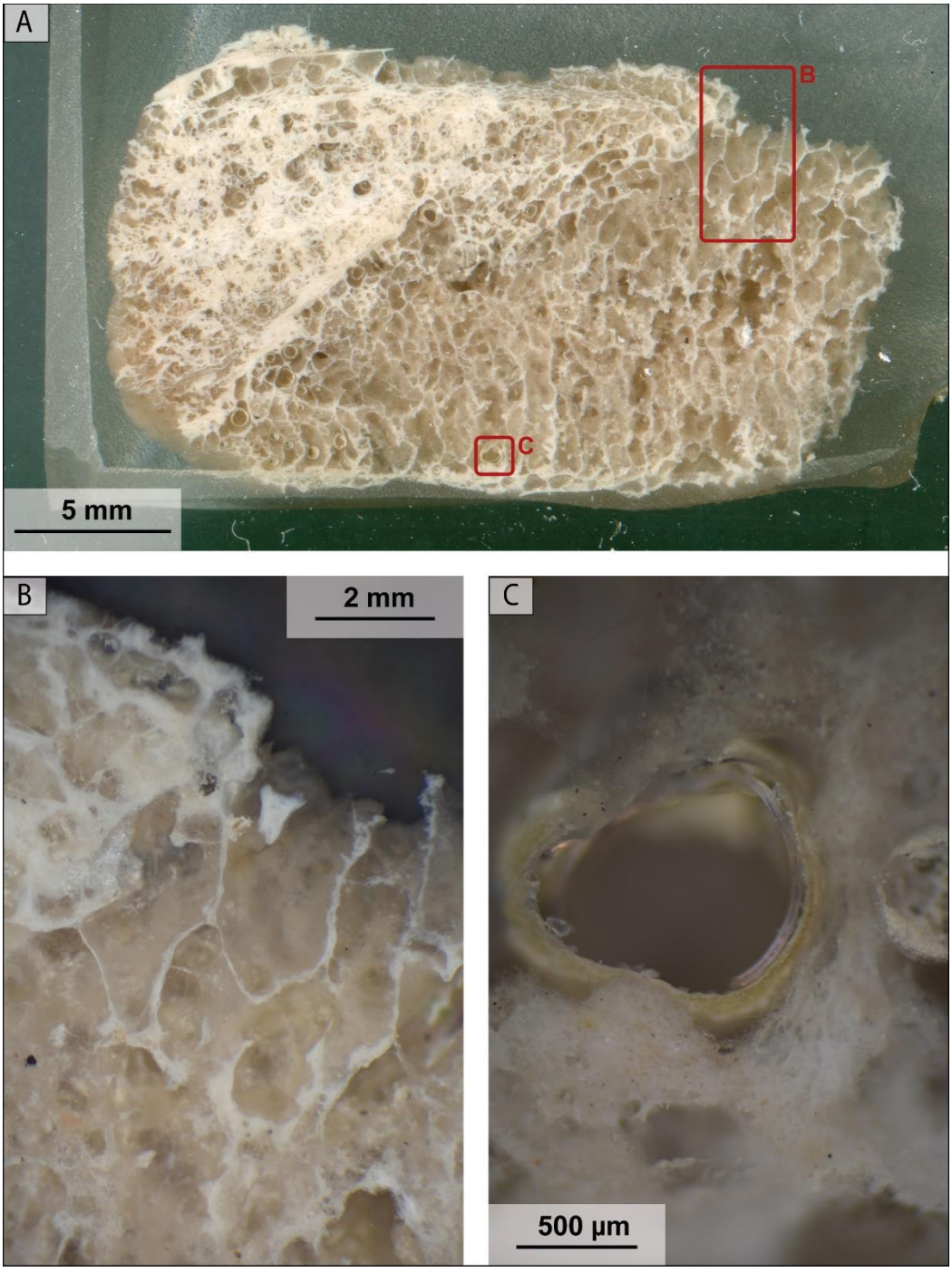

Figure 41: (A) Polished cross section of sample ETLIN02 from the Piscina Linzor, its fabric follows the pattern of a network of irregular silica threads, which generate a primary porosity that could be filled later. (B) Close-up of the silica network formed in this sinter. (C) Close-up of one of the sinter pores, which is inhabited by microbial filament, similar to those described by Gong et al. (2020).

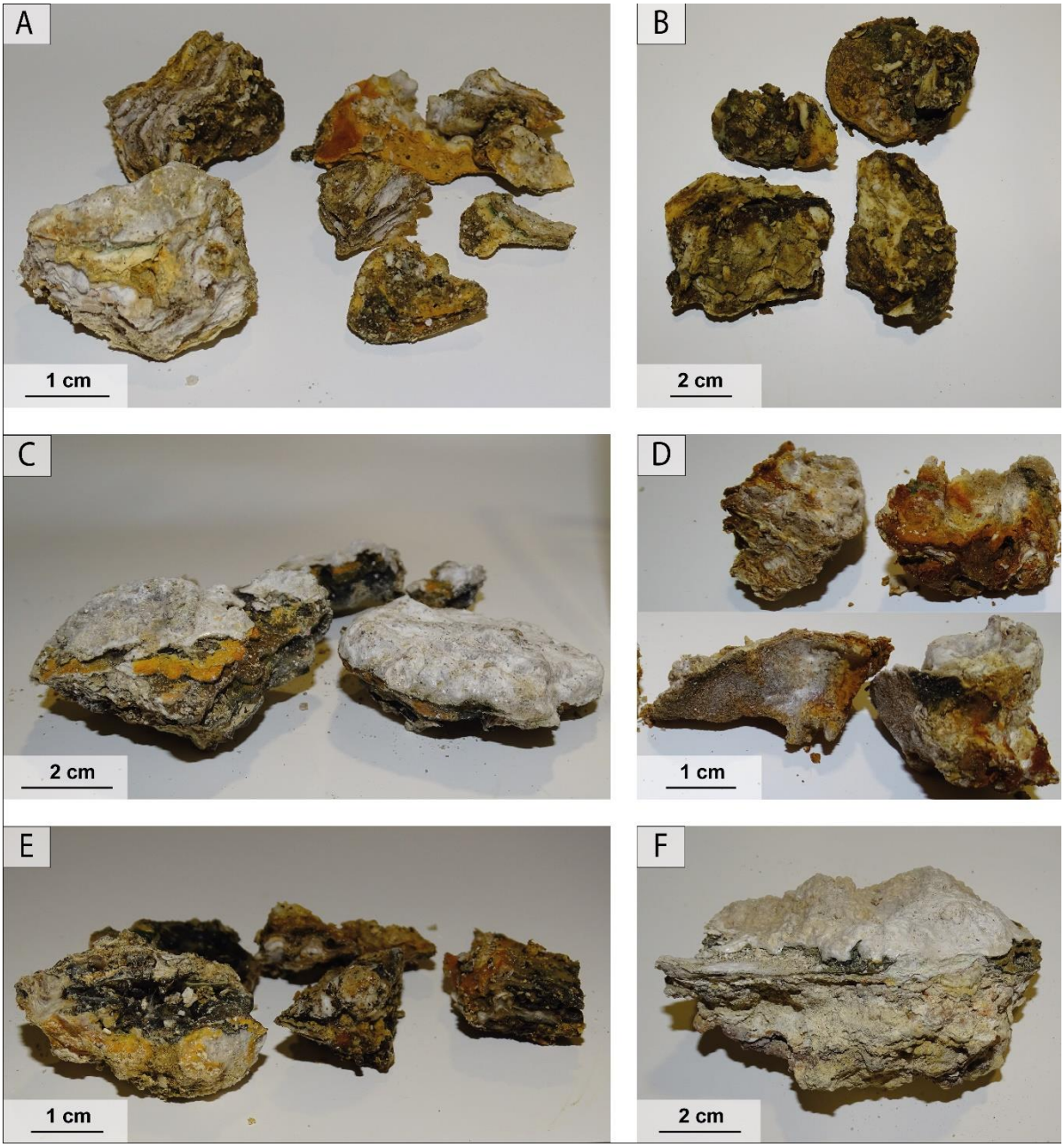

Figure 42: In-situ sinter deposit samples from the Ckoitchi area. (A) Samples called ET03-Co02.5, associated with the Co02 point. (B) Samples ET03-Co03 from point Co03. (C) Samples ET03-Co04 corresponding to the Co04 sector. (D) Samples ET03-Co05 from the Co05 sector. (E) Samples ET03-Co06 associated with the Co04 sector. (F) Sample ET03-Co07 located 12 m from the vent. All samples present laminations in whitish tones (deposited sinter), in addition, some of these laminations are yellowish, orange or blackish, associated with bacterial mats in the sector.

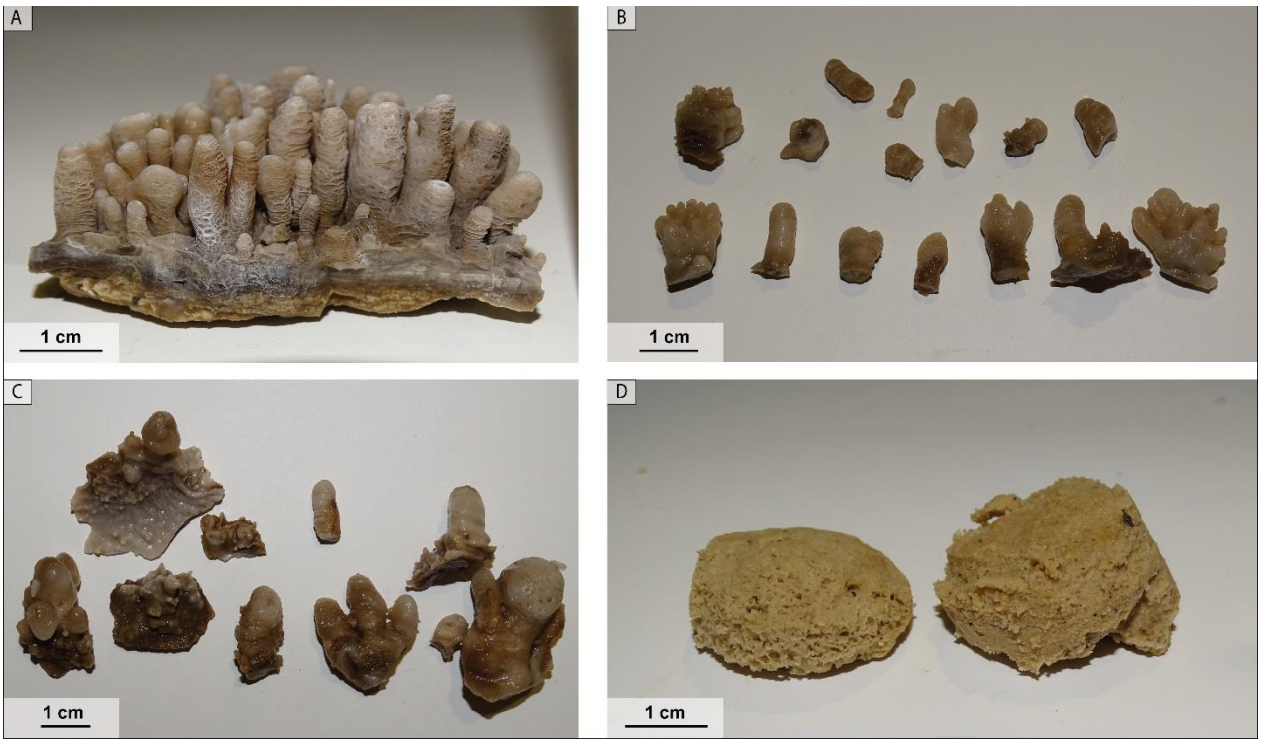

Figure 43: In-situ sinter deposit samples from the Vega Rinconada area along with samples from the Piscina Linzor. (A) Sample ET02-VR02 corresponding to point VR01, spicules of different widths and heights. (B) Samples ET02-VR03 from point VR02, with spicules of different sizes. (C) Samples ET02-VR04 from sector VR03, with the presence of spicules and some oncoids. (D) Sample ETLIN02 from the Piscina Linzor. The cylindrical shape is because they were extracted with a tube. The silica network and primary porosity formed during precipitation are observed.

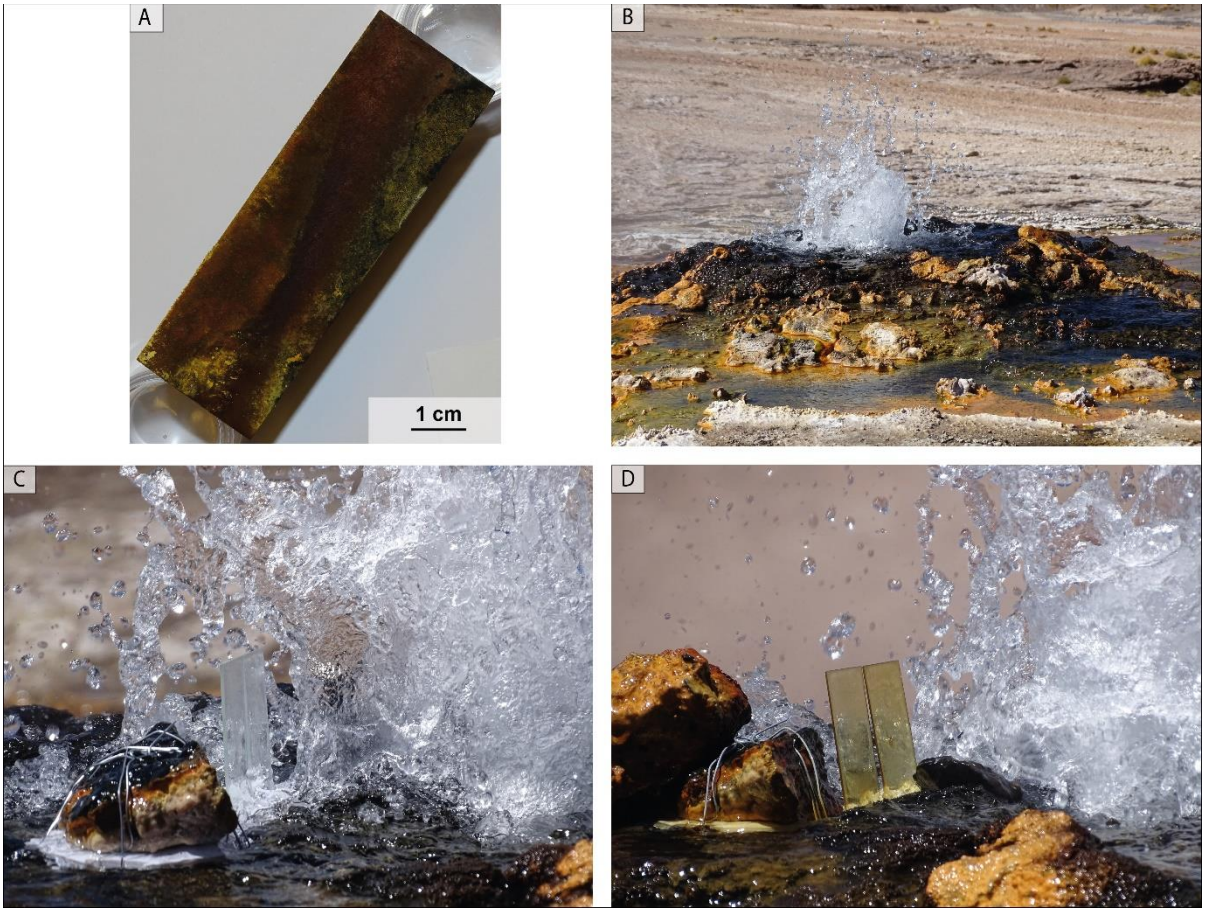

Figure 44: Samples from the precipitation experiment in the vent of Ckoitchi sector. (A) Complete view of one side of the CoVent-04 sample, which was found submerged in water at the time of extraction. (B) View of the vent of Ckoitchi to get a perspective in the following images. (C) Image of 24-09-2021, the day of implementation of the experiment, the slide on the left corresponds to the one in A. (D) Image two days after installation, on 26-09-2021, where the slide acquires a yellowish color due to the splashing of the perpetual spouter vent.

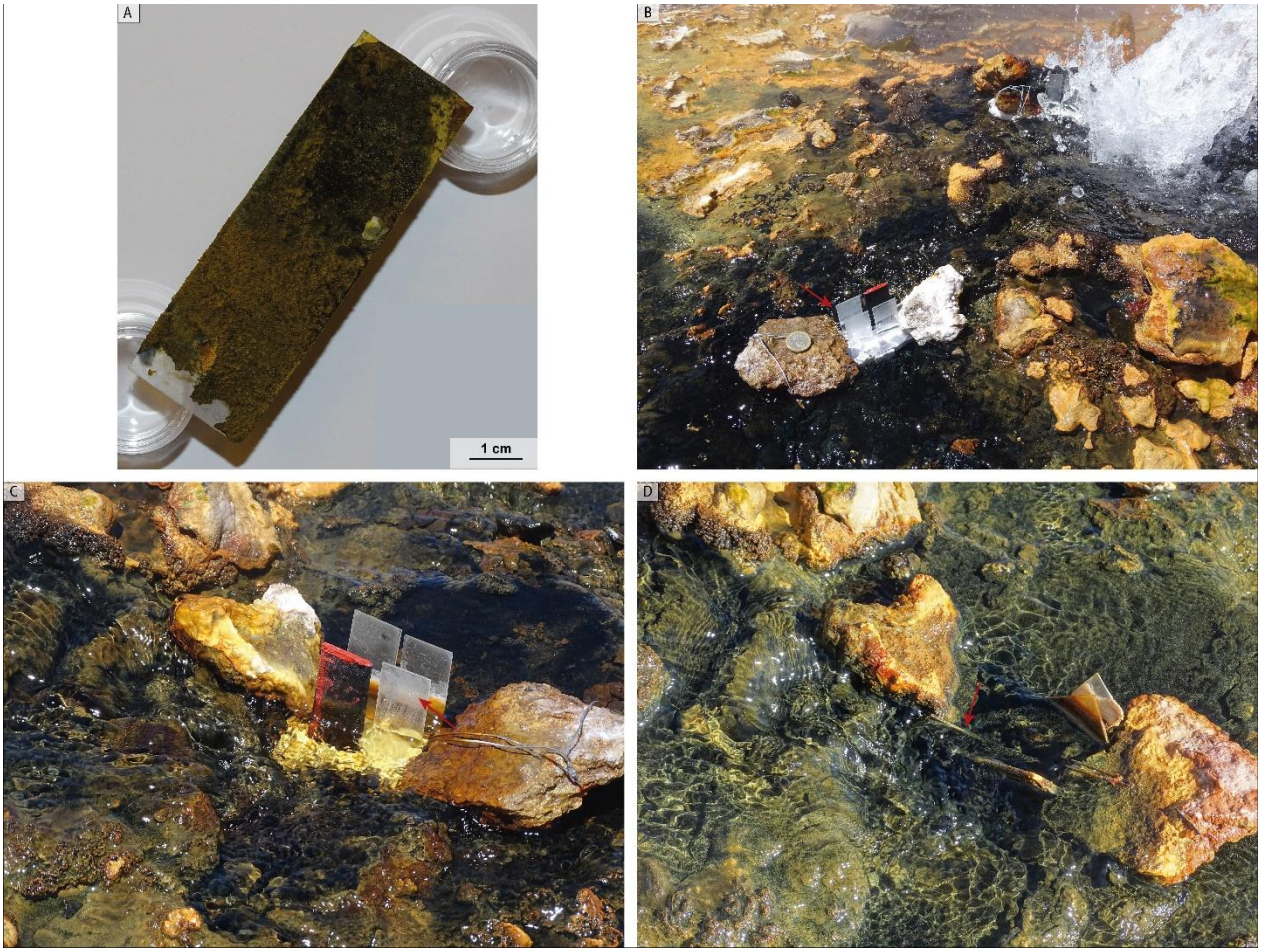

Figure 45: Images of sample Co01-39 from the precipitation experiment, associated with point Co01, red arrows indicate the position of the sample. (A) Complete view of one of the sides of the precipitate, the upper right corner is what can be seen in D. (B) Position of the samples with respect to the Vent, image from 24-09-2021 in its installation. (C) Image after a few days, on 01-10-2021, it can be seen that the slides present yellowish and whitish layers. (D) Image on the day of extraction, 22-04-2024, the slides do not retain their original position and are almost completely covered with blackish material, especially the submerged areas.

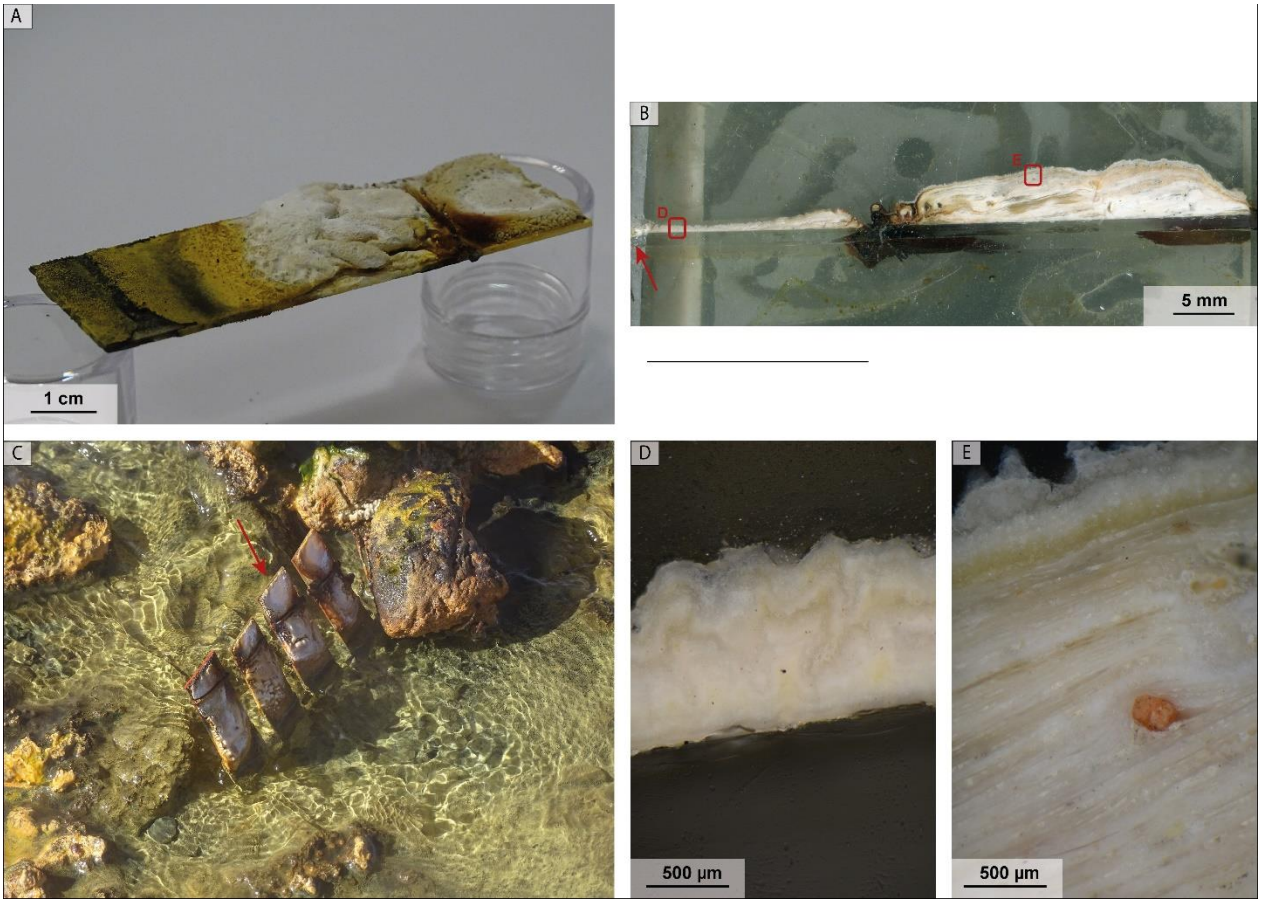

Figure 46: Sample Co01-68 from point Co01 at Ckoitchi, this slide was installed on 22-04-2022. (A) Perspective view of the slide, the left part of black-greenish shades was submerged. (B) Polished cross section of the precipitate, the red arrow indicates the non-submerged part of the sample (right part in A). (C) View of the samples at point Co01 on the day of extraction (22-04-2023), the red arrow indicates position of the sheet, indicating the same area as in B. (D) Close-up by optical microscopy of the image in B, showing the precipitate in massive form, with some colorations indicating different stages of precipitation. (E) Image by optical microscopy of the box shown in B. Fine laminations are observed in the deposit, together with some detritus trapped during precipitation.

Figure 47: Samples of the Co02 precipitation experiment in Ckoitchi. (A) Co02-06 slide used for chemical analysis, it can be observed that it has greenish and yellowish layers, with little indication of sinter precipitation. (B) Co02-40 precipitate used for SEM analysis, the formation of sinter is observed as small irregular spicules. (C) Image of the experimental setup on the day of installation (24-09-2021), where the red arrows indicate the positions of A and B as shown. (D) Image of the

sample extraction day (22-04-2022), where the red arrows also show the positions of A and B. In this case, A was almost completely submerged and covered by bacterial mat. (E) Polished cross section of B, two monticules that assimilate the shape of geyserites are observed, in addition the images F and G that were through optical microscopy are also indicated. (F) Close-up of the larger spicule in E, it is composed mainly of laminations that grow diagonally in brownish-whitish colors, it also presents some detritus. (G) Close-up of the small spicule, also showing the laminations of F, along with porosities between laminations and also the presence of detritus.

Figure 48: Samples associated with the Ckoitchi pun Co03 precipitation experiment. (A) Precipitate Co03-41 used for representative chemical analysis, greenish and yellowish layers are observed together with the precipitated opal. (B) Sample Co03-12 used for SEM analysis, with the same characteristics as the sample in A. (C) Image of 24-09-2021 when the samples were left installed. The red arrows indicate the positions of A and B. (D) Image on the day of sample removal (22-04-2022). (E) Polished cross section of the sample in B, images F and G observed through optical microscopy are indicated in red. (F) close-up of image E, massive laminations of silica (in white) are observed together with yellowish colors in some areas, in addition to the presence of detritus. (G) close-up of image E, this sector also shows laminations, but these are more irregular, with sectors that appear to be composed of microspheres. There are also yellowish zones with the presence of detritus.

Figure 49: Samples from the precipitation experiment corresponding to the Co04 point of Ckoitchi. (A) Precipitate Co04-43 used for chemical analysis, three main layers are observed, one whitish (precipitated opal) and the others of greenish and orange color, associated to the bacterial mat. (B) Co04-15 precipitate used for SEM analysis, with the same characteristics as the sample in A. (C) Image of the day of installation (24-09-2021), the rock arrows indicate the positions of A and B

respectively. (D) Perspective image of the day of sample extraction (22-04-2022), the Ckoitchi vent can be seen in the background. (E) Polished cross section image of B. The layer of precipitated opal covered by a greenish layer is observed. The location of images F and G obtained by optical microscopy is also indicated. (F) Close-up of image E, the precipitated opal is observed above the surface of the glass slide. (G) Close-up of image E, the contact between the precipitated opal (whitish laminations with detritus) and the bacterial mat (greenish network with precipitated opal in between) can be observed.

Figure 50: Samples from the Co05 point precipitation experiment at Ckoitchi. (A) Sample Co05-42 used for chemical analysis, a reddish-brown layer of very fine grains is observed. (B) Sample Co05-19 used for SEM analysis, a whitish layer of opal precipitate is observed (left side), in addition to the same reddish-brown layer of fine grains of (A). (C) Image of the day of sample positioning (24-09-2021) on the side of the pool. The red arrows indicate the positions of A and B. (D) Image of sample extraction day (22-04-2022), showing the final position, with A fully submerged and B subhorizontal. (E) Polished cross section of the sample in B, showing the resulting

precipitate, resembling a spicule shape at the bottom. The insets indicate the positions of images F and G obtained by optical microscopy. (F) close-up of image E, showing the whitish laminations, with the presence of detritus especially in the lower part of the deposit, in addition to a reddish-brown coating, possibly associated with bacterial mat. (G) close-up of the upper part of F, with greater detail of the laminations.

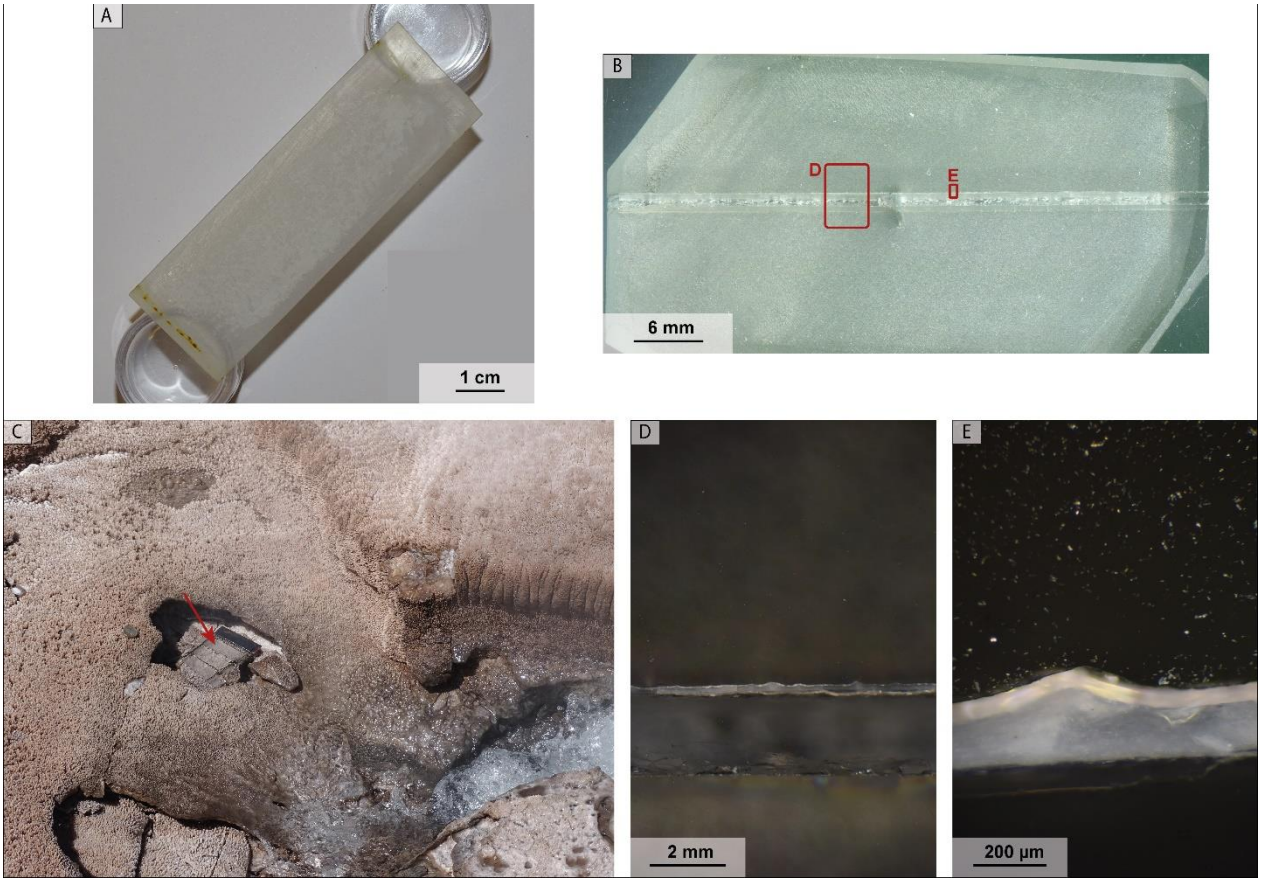

Figure 51: (A) Sample VR01-21 associated with the Vega Rinconada vent (point VR01), a whitish and irregular zone corresponding to the precipitate is observed. (B) Polished cross section of the sample in A, the precipitate is barely distinguishable at that scale. (C) image of the day of sample extraction (22-04-2022), the red arrow indicates the position of the laminate, to the left of the arrow is a 100 Chilean peso coin as a scale. (D) Close-up of image D, where it is possible to distinguish the precipitate (thin whitish layer) from the glass slide (below). (E) Close-up of the image in B, the thin layer of silica precipitated on the slide is observed, and covered by a thin shiny layer, which may be associated with cyanobacteria.

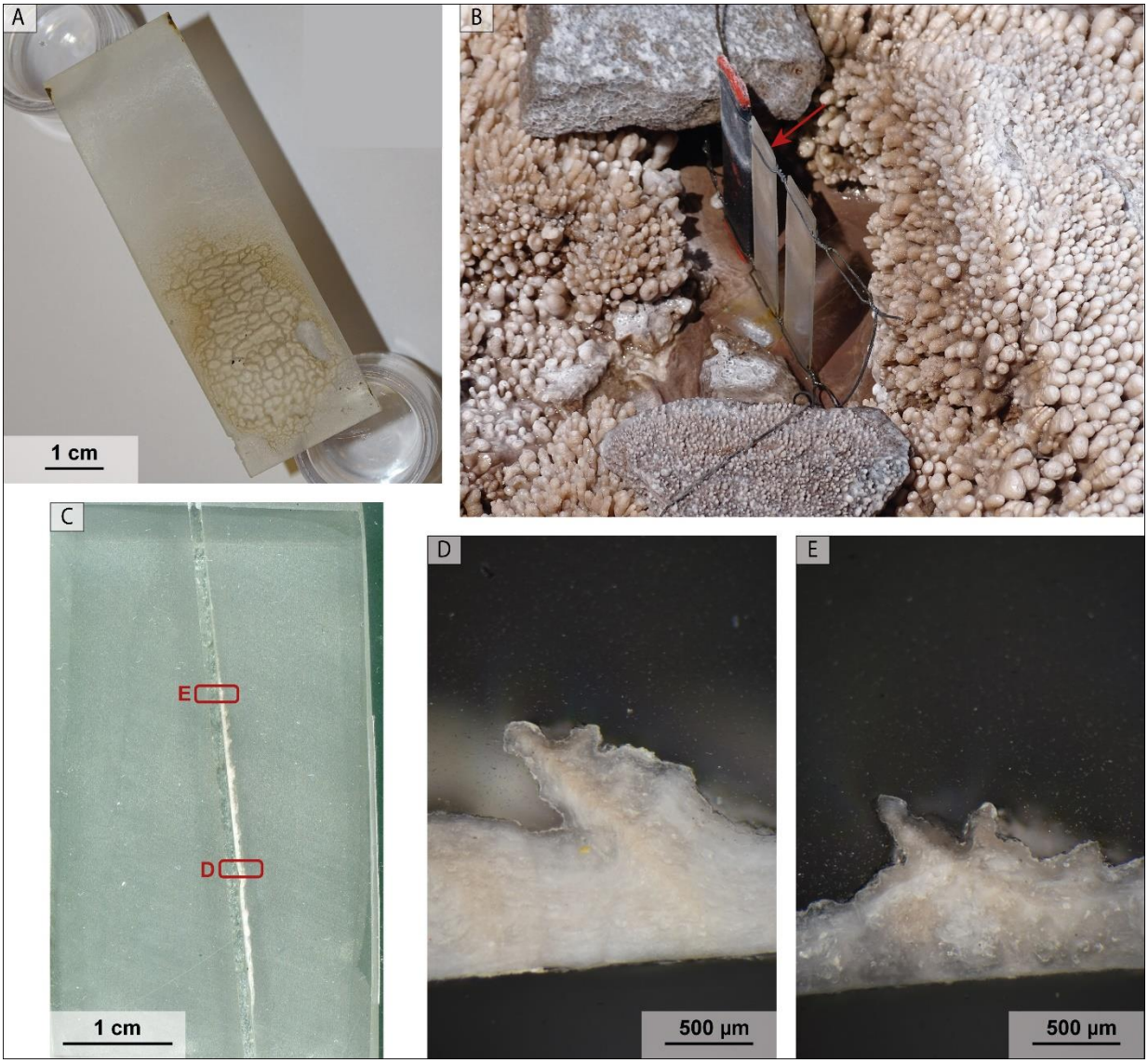

Figure 52: (A) Precipitate VR02-49 from point VR02 in Vega Rinconada, a light brown-whitish layer of irregular polygonal shapes is observed. (B) Image of the day the sample was extracted (22-04-2023) the laminate remained in the place where it was left, the red arrow indicates its position, the vent is to the left with respect to the image. (C) Polished cross section of the sample. A white precipitate layer is observed. In addition, the red boxes indicate the positions of images D and E obtained by optical microscopy. (D) Close-up of the image in C, a small diagonal spicule is observed, with almost imperceptible fine laminations of white color, besides the presence of few and very small detritus. (E) Close-up of the image in C, in this case two small spicules are observed, of white color and almost vitreous in some parts, due to the fact that the sector of the image has less precipitate than in D.

Figure 53: (A) Sample VR03-27 from point VR03 of Vega Rinconada, used for the representative chemical analysis. (B) Image of the day of sample installation (25-09-2021), the red arrow on the left indicates the position of the slide, also a Chilean 100 pesos coin is presented as scale. The vent is located downwards with respect to the image. (C) Image a few days later (01-10-2021) where it is observed that some silica precipitated in the samples, the red arrow indicates the position of the sample in A and the vent is located towards the upper left zone with respect to the image. (D) Image on the day of sample extraction (22-04-2022) showing that all the slides have precipitate. The red arrow indicates the position of the sample in A, there is also a Chilean 100 pesos coin as a scale, and the vent is located upwards with respect to the image.

Figure 54: (A) Sample VR03-52 from point VR03 at Vega Rinconada, showing the whitish precipitate with light brown tones. (B) Polished cross section of A, indicating the position of samples D and E obtained by optical microscopy. The red arrow indicates the same position as in image C. (C) Image of the day of sample extraction (22-04-2023), all slides show precipitated material. The vent is located upwards with respect to the image. (D) Close-up of the image in B, an almost homogeneous layer of precipitated opal is observed, with a slight presence of very small detritus. (E) Close-up of the image in B, it is observed that the precipitate is almost massive without laminations, besides the yellowish detritus that were cemented.

Figure 55: Samples from the precipitation experiment at Vega Rinconada point VR04. (A) Precipitate VR04-38 used for the representative chemical analysis, shows white and light brown shades. (B) Sample VR04-34 used for the SEM analysis, shows whitish and light brown shades, in addition to a larger amount of deposited material. (C) Image of the day of sample installation (25-09-2021),

with the arrows indicating the position of the slides. A Chilean 100 pesos coin is presented as a scale. The vent is located to the lower right of the image. (D) Image of the day of sample extraction (22-04-2022) where not much precipitated material is observed. The red arrows indicate the positions of the samples. In addition, the same previous scale coin is present, and the vent is down to the right with respect to the image. (E) Polished cross section of the sample in B, together with the boxes indicating the positions of F and G, obtained by optical microscopy. (F) Close-up of image E, showing a thin layer of whitish precipitate with a lot of detritus present. (G) Close-up of image in F, showing a detritus that was cemented by silica precipitation.

ANNEX C

Table 17: Qualitative information obtained from energy-dispersive X-ray spectrometry (EDS) in scanning electron microscopy (SEM) considering three samples of sinter in-situ (from vents of Ckoitchi and Vega Rinconada, and sinter of Piscina Linzor) and samples from the precipitation experiment (nine samples, one per position without considering the Ckoitchi vent).

Sample ID	Analysis type	Name ID	Data	SiO_2	Al_2O_3	FeO	TiO_2	As_2O_3	CaO	Na_2O	K_2O	C	SO_3	MgO	Cs_2O	MnO	Sb_2O_3
				wt. %	wt.%	wt.%	wt.%	wt.%	wt.%	wt.%	wt.%	wt.%	wt.%	wt.%	wt.%	wt.%	wt.%
Co01-68	point	355	Spectrum1	66.71	1.46	25.94	2.97	-	1.36	0.81	0.26	-	-	0.48	-	-	-
			Spectrum3	97.94	-	-	-	-	1.04	0.73	0.29	-	-	-	-	-	-
			Spectrum4	95.29	-	-	-	-	1.75	1.52	0.34	-	-	-	-	-	-
			Spectrum5	96.15	0.00	0.49	-	-	1.79	0.89	0.4	-	-	-	-	-	-
Co02-40	point	025zoom	Spectrum3	83.72	5.84	-	-	1.16	3.74	2.58	1.14	-	-	-	-	-	-
Co05-19	point	250	Spectrum1	92.68	4.34	-	-	-	-	1.64	1.33	-	-	-	-	-	-
ET02-VR01	map	260	map	86.59	6.84	0.74	-	-	0.57	1.84	2.61	-	-	-	0.6	-	-
	profile	260	profile	84.73	7.61	0.81	-	-	0.74	2.05	3.16	-	-	-	0.67	-	-
	point	667	Spectrum1	85.41	0.73	-	-	-	-	0.53	0.31	13.02	-	-	-	-	-
	point	667zoom	Spectrum1	24.85	2.37	56.21	15.13	-	-	-	-	-	-	1.44	-	-	-
			Spectrum3	69.95	15.84	0.59	-	-	-	-	13.63	-	-	-	-	-	-
			Spectrum4	5.16	-	20.64	-	-	-	-	-	17.43	56.77	-	-	-	-
			Spectrum5	14.48	-	17.43	-	-	-	-	-	21.95	46.14	-	-	-	-
	profile	963	profile	83.15	5.8	3.21	1.78	-	0.39	1.26	2.41	-	-	1.76	-	-	-
ET03-Co01	profile	571	profile	75.10	1.96	16.44	-	-	1.59	1.12	0.57	-	-	2.31	-	0.41	-
	profile	483	profile	79.35	1.57	14.2	-	-	1.25	0.91	0.52	-	-	1.4	-	0.37	-
ETLIN02	point	452	Spectrum4	79.97	11.61	-	-	-	-	3.24	4.67	-	-	-	-	-	-
			Spectrum6	98.27	1.25	-	-	-	-	-	0.48	-	-	-	-	-	-
			Spectrum8	89.71	8.09	-	-	-	-	-	2.2	-	-	-	-	-	-
VR01-21	point	285	Spectrum2	83.49	0.64	-	-	-	-	1.12	0.35	14.23	-	-	-	-	-
			Spectrum3	97.65	0.82	-	-	-	-	1.13	0.39	-	-	-	-	-	-
VR02-49	point	344	Spectrum1	95.38	-	-	-	-	-	1.49	0.69	-	-	0.66	-	-	1.3
			Spectrum2	95.84	-	-	-	-	0.36	1.14	0.51	-	-	-	-	-	1.64
			Spectrum3	78.86	-	-	-	-	-	0.76	0.5	18.43	-	-	-	-	0.91
			Spectrum4	96.31	-	-	-	-	0.36	0.88	0.41	-	-	-	-	-	1.7
			Spectrum5	96.76	-	-	-	-	-	1.11	0.55	-	-	-	-	-	1.12
VR03-52	point	375	Spectrum1	96.11	-	-	-	-	0.27	0.82	0.43	-	-	-	-	-	1.98
			Spectrum2	98.01	-	-	-	-	-	0.41	0.32	-	-	-	-	-	1.25
			Spectrum3	60.19	10.64	7.93	1.85	-	5.79	2.56	0.78	-	-	10	-	-	-
			Spectrum4	96.84	-	-	-	-	-	0.84	0.4	-	-	-	-	-	1.32
			Spectrum5	65.07	11.81	6.85	1.51	-	0.88	1.62	6.32	-	1.48	4.22	-	-	-
			Spectrum6	36.67	21.08	6.87	-	-	17.23	-	-	18.15	-	-	-	-	-
			Spectrum7	96.06	-	-	-	-	-	1.08	0.65	-	-	-	-	-	1.77
VR04-34	point	385	Spectrum1	89.30	-	-	-	-	1.84	3.26	1.1	-	1.98	-	-	-	-
			Spectrum2	94.00	-	-	-	-	-	1.78	1.09	-	-	-	-	-	1.04
			Spectrum3	93.42	-	-	-	-	0.45	1.71	1.09	-	-	-	-	-	1.66
			Spectrum4	81.76	-	-	-	-	-	1.7	0.74	13.27	-	-	-	-	1.05
			min	5.16	0.64	0.49	1.51	1.16	0.27	0.41	0.26	13.02	1.48	0.48	0.60	0.37	0.91
			max	98.27	21.08	56.21	15.13	1.16	17.23	3.26	13.63	21.95	56.77	10.00	0.67	0.41	1.98
			mean	80.03	5.56	12.74	4.65	1.16	2.30	1.42	1.53	16.64	26.59	2.78	0.64	0.39	1.40
			SD	23.69	5.29	15.02	5.89	-	3.97	0.73	2.56	3.28	29.04	3.14	0.05	0.03	0.34

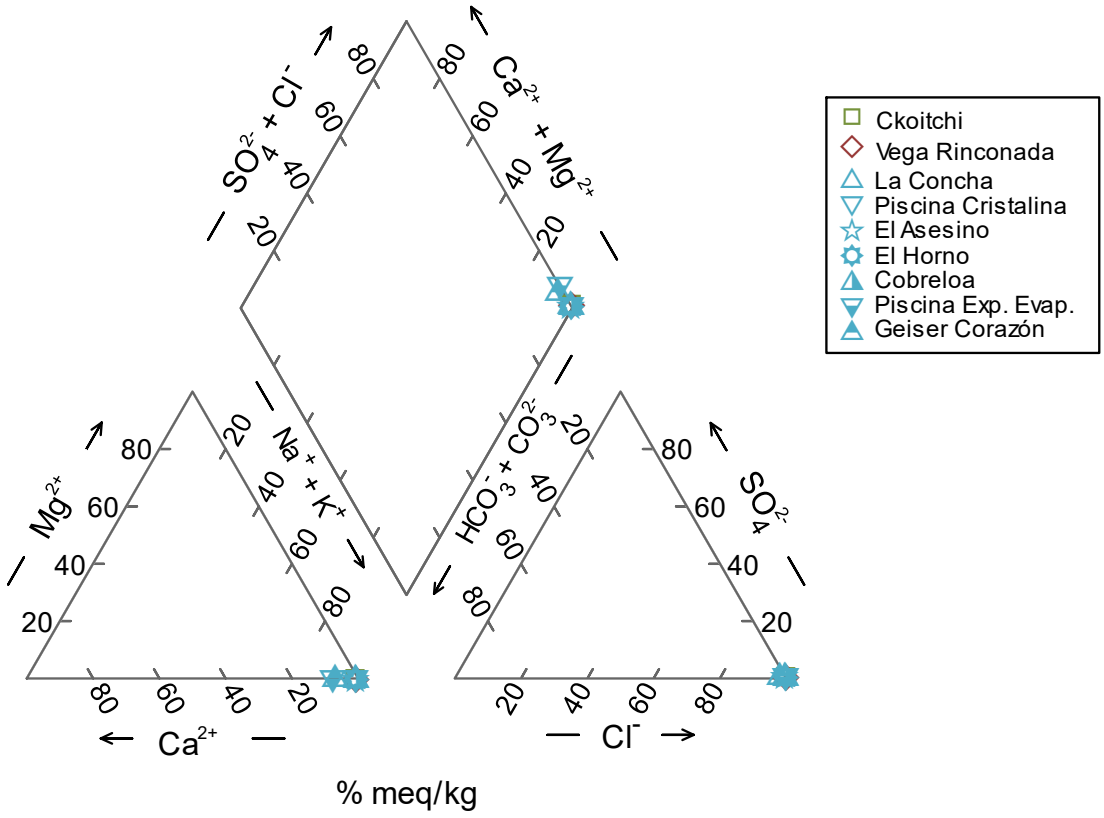

Figure 56: Classification of Ckoitchi hydrothermal fluids according to Piper's classification (Piper, 1944). In this case, they correspond to Na-Cl type waters.